

Imaging the earth with ambient noise and earthquakes

Thesis by
Yiran Ma

In Partial Fulfillment of the Requirements
for the Degree of
Doctor in Philosophy

The logo for the California Institute of Technology (Caltech), featuring the word "Caltech" in a bold, orange, sans-serif font.

California Institute of Technology
Pasadena, California

2016
(Defended December 10, 2015)

To my parents.

Acknowledgments

The PeruSE experiment was supported by the Gordon and Betty Moore Foundation and NSF (EAR-1045683).

I would like to first thank my adviser, Prof. Rob Clayton. Rob's sharpness in science is always admirable. Without the support, freedom, and respect he gave me, this thesis could not have been possible. I also thank the other members of my thesis committee, including Prof. Don Helmberger, Prof. Joann Stock, Prof. Jennifer Jackson, and Prof. Victor Tsai, for the time they dedicated to my thesis and its progress.

In addition to that, Prof. Joann Stock's guidance on the Salton project has been valuable. I also thank Prof. Mike Gurnis for his guidance on my second oral project about basin modeling.

My thanks also go to Donna Mireles, Kim Baker-Gatchalian, Rosemary Miller, Viola Carter, Julia Zuckerman, Mike Black, and the other administrative and IT staff for all the help they have provided.

The students in the Seismo Lab have made it a delightful place to be a part of. In particular, I thank my officemates Semechah Lui, Kangchen Bai, VoonHui Lai, Jorge Castillo Castellanos, Francisco Ortega, Xiangyan Tian, and those in Rob's group meeting: Younghee Kim, Kristin Phillips, Ting Chen, Sara Dougherty, Asaf Inbal, Daniel Bowden, and Jose Luis Garcia-Reyes. Discussion with Patricia Persaud has been encouraging. I also thank some other friends in and out of the lab, with whom I have had lots of fun: Lingsen Meng, Jingshu Shen, Zhongwen Zhan, Dongzhou Zhang, Yihe Huang, Junle Jiang, Yingdi Luo, Junjie Yu, Xiaolin Mao and Huan Tang, Daoyuan Sun, Han Yue, Yanghui Zhao, Jing Luan, and Xuan Zhang.

I'm always grateful for the resources and colleagues I had as an undergraduate. I owe special thanks to the members in the geophysics group of Nanjing University who were willing to spend time and resources on me, in particular, Pan Wang, who taught me receiver functions. I also thank those old friends of mine, in particular, Chen Gu, for her encouragement and positive influence since college, and Yue Shi, for her continuous caring and support since high school.

The most important encounter I had at Caltech must be my fiancé Dunzhu Li. I thank him for his love, and all the positive influence he has had on my life. My uncles' families have taken care of me since the first day I arrived in the U.S., and I owe them a lot of thanks. Last but not least, I would like to thank my parents, Nailun Ma and Suying Jin, and my younger brother Ziyao Ma, for their endless love. My parents are extremely devoted to their work and family, which has had a long-lasting influence over me.

Abstract

In this thesis, I develop the velocity and structure models for the Los Angeles Basin and Southern Peru. The ultimate goal is to better understand the geological processes involved in the basin and subduction zone dynamics. The results are obtained from seismic interferometry using ambient noise and receiver functions using earthquake-generated waves. Some unusual signals specific to the local structures are also studied. The main findings are summarized as follows:

(1) Los Angeles Basin

The shear wave velocities range from 0.5 to 3.0 km/s in the sediments, with lateral gradients at the Newport-Inglewood, Compton-Los Alamitos, and Whittier Faults. The basin is a maximum of 8 km deep along the profile, and the Moho rises to a depth of 17 km under the basin. The basin has a stretch factor of 2.6 in the center decreasing to 1.3 at the edges, and is in approximate isostatic equilibrium. This “high-density” (~ 1 km spacing) “short-duration” (~ 1.5 month) experiment may serve as a prototype experiment that will allow basins to be covered by this type of low-cost survey.

(2) Peruvian subduction zone

Two prominent mid-crust structures are revealed in the 70 km thick crust under the Central Andes: a low-velocity zone interpreted as partially molten rocks beneath the Western Cordillera – Altiplano Plateau, and the underthrusting Brazilian Shield beneath the Eastern Cordillera. The low-velocity zone is oblique to the present trench, and possibly indicates the location of the volcanic arcs formed during the steepening of the Oligocene flat slab beneath the Altiplano Plateau.

The Nazca slab changes from normal dipping ($\sim 25^\circ$) subduction in the southeast

to flat subduction in the northwest of the study area. In the flat subduction regime, the slab subducts to ~ 100 km depth and then remains flat for ~ 300 km distance before it resumes a normal dipping geometry. The flat part closely follows the topography of the continental Moho above, indicating a strong suction force between the slab and the overriding plate. A high-velocity mantle wedge exists above the western half of the flat slab, which indicates the lack of melting and thus explains the cessation of the volcanism above. The velocity turns to normal values before the slab steepens again, indicating possible resumption of dehydration and eclogitization.

(3) Some unusual signals

Strong higher-mode Rayleigh waves due to the basin structure are observed in the periods less than 5 s. The particle motions provide a good test for distinguishing between the fundamental and higher mode. The precursor and coda waves relative to the interstation Rayleigh waves are observed, and modeled with a strong scatterer located in the active volcanic area in Southern Peru. In contrast with the usual receiver function analysis, multiples are extensively involved in this thesis. In the LA Basin, a good image is only from PpPs multiples, while in Peru, PpPp multiples contribute significantly to the final results.

Contents

Acknowledgments	iv
Abstract	vi
1 Introduction	1
1.1 Los Angeles Basin	1
1.2 Peruvian subduction zone	2
I LASSIE: Los Angeles Syncline Seismic Interferometry Experiment	5
2 Higher-mode ambient-noise Rayleigh waves in sedimentary basins	6
2.1 Abstract	6
2.2 Introduction	6
2.3 Multi-component cross-correlations	10
2.3.1 Love wave	11
2.3.2 Rayleigh wave	13
2.4 Numerical investigations on Rayleigh wave in a basin model	19
2.4.1 1-D model	19
2.4.2 2-D model	24
2.5 Discussions and Conclusions	26
2.6 Supplementary material	29
3 Structure of the Los Angeles Basin from ambient noise and receiver	

functions	34
3.1 Abstract	34
3.2 Introduction	34
3.3 Receiver functions	37
3.4 Ambient noise tomography	41
3.4.1 Phase velocity maps	42
3.4.2 Shear velocity structure	43
3.5 Discussion	47
3.5.1 The basement and Moho depths	47
3.5.2 Comparison with the uniform stretching model	48
3.5.3 The shear velocities	50
3.6 Conclusions	51
3.7 Supplementary material	52
II PeruSE: Peru Subduction Experiment	61
4 Locating a scatterer in the active volcanic area of Southern Peru from ambient noise cross-correlations	62
5 The crust and uppermost mantle structure of Southern Peru from ambient noise and earthquake surface wave analysis	73
6 Flat slab deformation caused by interplate suction force	86
7 Conclusions	105

List of Figures

2.1	The LASSIE array. The red and yellow dots are LASSIE stations, and the black circles are SCSN stations. The green line denotes the location of the 2-D profile (A-A'), and the distances from "A" are marked with blue crosses in 10 km intervals. The faults are shown with pink lines (from Jennings and Bryant (2010)).	9
2.2	CVM-H model along A-A' profile. The white lines delineate the basement and the Moho depths. The Puente Hills is at ~30 km distance, and separates the Los Angeles Basin (LAB) to the south and the San Gabriel Valley (SGV) to the north.	10
2.3	Love waves shown in the tangential-component cross-correlations between N116 and all the yellow stations in Fig. 2.1. The cross-correlations filtered to 1 and 5-s period are shown as examples. The asymmetry of the cross-correlations is due to the asymmetry of the noise source amplitude, which is strong to the south.	12
2.4	Tomographic inversion result along A-A' profile (Fig. 2.1) with measured Love wave dispersion curves. The y-axis is the period. The Los Angeles Basin (LAB) and San Gabriel Valley (SGV) are shown as low velocities. The Newport-Inglewood Fault (NIF) and Whittier Fault (WF) are shown.	12

2.5	Rayleigh waves shown in the vertical and radial component cross-correlations (Z-Z, Z-R, R-Z, and R-R) between N116 and all the yellow stations in Fig. 2.1. (a) Filtered to 1-s period. Both fundamental and higher modes are strong. (b) Filtered to 3-s period. The higher mode is generally stronger in the four profiles. (c) Filtered to 5-s period. Only the fundamental mode is observed.	17
2.6	Particle motion measurements using the cross-correlations (Z-Z, Z-R, R-Z and R-R) between N116 and A135. Tab.2.1 shows the cross-correlation pair used for each measurement. For each period, we have a maximum of four measurements corresponding to the two force directions (Z-Z/Z-R pair, or R-Z/R-R pair) and two modes. We only measure the particle motion when the phase is clear. We observe that the higher mode disappears above ~ 4 -s period. The higher mode has a prograde particle motion, while the fundamental mode has a retrograde particle motion. A rapid increase in the ellipticity (H/V) of the fundamental mode around 4-s period is observed at N116.	19
2.7	The eigenfunction of 3-s period Rayleigh wave calculated for the basin model in Tab. 2.2. The eigenfunctions are normalized for each mode.	22
2.8	The dispersion curve and ellipticity for fundamental and 1st higher mode Rayleigh wave in 1-10 s period, calculated for a basin model in Tab. 2.2. Note the different direction of particle motion between fundamental and higher mode. The higher mode is evanescent above about 4.5-s period, along with a rapid increase in the ellipticity of the fundamental mode.	23
2.9	The FK synthetics on the waveform in a 1-D structure (Tab. 2.2). The source is at 0.5 km depth with a central period of 3 s. The waveforms are filtered to 3-s period. The top two panels show the Z and R recordings with a Z source. The bottom two panels show the results for R source.	24

2.10	(Top panel) 2-D model for the FD modeling. The source is at 0 km distance. (Bottom panel) The H/V ratio measured from the waveforms (dashed line) and that predicted from the local 1-D structure (solid line). Result at 2 and 3-s period shows that the H/V ratio is a site property in a large scale, but sharp variations in the structure do add complexities to it.	26
2.11	An example to distinguish the two modes using Z-Z and Z-R cross-correlations between N116 and A135. (a) At 3-s period. Both higher and fundamental modes are observed. The separation time corresponds to the maximum curvature point in the phase plot. (b) At 6-s period, only the fundamental mode is observed.	29
2.12	The Rayleigh wave dispersion and ellipticity calculated for a basin model with a basement at: (a) 6-km depth; (b) 8-km depth. The other model parameters are same as that in Tab. 2.2.	31
2.13	The waveforms (before and after filtering to 1-10 s) in the FD modeling (section 2.4.2, Fig. 2.10). The strong body wave signals arriving ahead of the surface wave are muted. The red solid lines show the group arrival time of 3 and 4-s period surface waves. We see that we may only measure the surface waves up to 3 s.	33
3.1	The LASSIE array. The red and yellow dots are LASSIE stations, and the black circles are SCSN stations. The green line denotes the location of the 2-D profile (A-A'), and the distances from "A" are marked with blue crosses in 10 km intervals. The faults are shown in pink lines, and some of them are annotated: NIF - Newport-Inglewood Fault, C-LAF - Compton-Los Alamitos Fault, WF - Whittier Fault. The Ps conversion points at 20 km depth (blue and green squares) are plotted for the two events used in the receiver functions (Fig. 3.2).	37

3.2	Receiver functions of two events recorded by all the yellow-dot stations in Fig. 3.1. The PpPs phase related to the P-to-S conversion at the basement is recognized after the time-depth conversion shown in Fig. 3.9.	40
3.3	CCP migration with PpPs phase. The white lines delineate the inferred basement depth and Moho depth.	41
3.4	Tomographic inversion result along A-A' profile. The y-axis is the period. The results above 5-s period are extracted from Figs. 3.11 and 3.12, in which we use both LASSIE and SCSN stations. For Love wave below 5 s, we only use LASSIE stations. The inversion is similar to the one shown in Fig. 3.11, but in a small rectangular region that encloses LASSIE stations only.	43
3.5	V_{SH} inversion results using 1-12 s Love wave dispersion data. From top to bottom: linear inversion, nonlinear inversion, and CVM-H model.	45
3.6	V_S inversion results using 1-12 s Love wave and 5-10 s Rayleigh wave dispersion data. From top to bottom: linear inversion, nonlinear inversion, and CVM-H model. The approximate location of the "C-LAF" (Compton-Los Alamitos Fault) from Wright (1991) (Fig. 3.16) is delineated with red dashed line.	46
3.7	The predicted total subsidence from 1-D uniform stretching model. The solid lines are predictions with parameters in McKenzie (1978) , and the dashed lines are that with a 5% decrease in the crustal density. The data (asterisks) are fit by the dashed lines, due to the increase in the initial subsidence, instead of the thermal subsidence, which is against the strata data.	49
3.8	CVM-H model along profile A-A'.	52
3.9	The depth-axis RFs with time-depth conversion for PpPs phase. The ~ 5 km offset in the structures in the two profiles is due to the different piercing points of the two events (Fig. 3.1), which is corrected in the CCP profile (Fig. 3.3). The black and yellow lines delineate the basement and the Moho respectively.	53

3.10	The time-axis RFs for DLA station. The events are arranged according to the back-azimuths, and are divided by four quadrants. The colored bar along the x-axis divides the quadrants.	54
3.11	Love wave phase velocity map and resolution test for 5 to 12-s period.	55
3.12	Rayleigh wave phase velocity map and resolution test for 5 to 10-s period.	56
3.13	The resolution matrix for the 1-D inversion at $x \approx 0$ km. (a) shows that the Love wave inversion has a good resolution until 3 km depth. (b) shows that with the Rayleigh wave data alone, one cannot constrain the structure. (c) shows that with both types of data, the resolution can reach about 8 km depth.	58
3.14	Data and predictions from the model (Fig.3.6, second panel) inverted from the dispersion curves.	59
3.15	The change in the prediction of total subsidence with 10% perturbation in each parameter.	60
3.16	A geological profile adapted from Wright (1991) . The red line shows the approximate range of A-A'.	60

List of Tables

2.1	Cross-correlation pairs used for measuring particle motion.	18
2.2	1-D basin model.	21
3.1	Events with clear recordings. The top two events happened while most stations were in operation, and are used in the receiver function analysis.	39

Chapter 1

Introduction

This thesis is composed of two parts: the “Los Angeles Syncline Seismic Interferometry Experiment” (LASSIE) in the Los Angeles Basin, and the “Peru Subduction Experiment” (PeruSE) in the Peruvian subduction zone. These two projects are at different scales, but with the same goal of imaging the interior structure of the earth. The main tools involved are seismic interferometry using ambient noise, and receiver functions from earthquake-generated waves. The results serve as a framework for discussion of the geological processes related to the basin and subduction zone dynamics. The motivation and outline of each part are briefly introduced in the following.

1.1 Los Angeles Basin

Determining the basin structure is important for evaluating the potential seismic hazard because basins trap and amplify strong motion energy (Olsen, 2000; Komatitsch et al., 2004). The Los Angeles Basin is a typical example of this. And because of its size and depth, the basin is capable of enhancing waves in the 2-5 sec range, which is particularly dangerous for high-rise buildings. Numerical modeling of these phenomena requires an accurate model of the subsurface structure and velocities that define the basin. As is also a significant oil-production area, the LA Basin has been explored by numerous oil-company surveys and the results were presented in Wright (1991). These high resolution data have been an important component of the unified model in this region (Shaw et al., 2015). However, some critical improvements are needed.

First, since the industry data is based on P wave velocities, the S wave velocities that are important for ground motion simulations are determined by inference and need direct measurements. Second, the deeper structures like basin bottom and the Moho are not covered by the industry data. These have never been directly imaged.

In Chapters 2-3, we add some additional constraints on the structure of the LA Basin and its shear wave velocities, based on the new LASSIE experiment that was done in the fall of 2014. This “high-density” (~ 1 km spacing) “short-duration” (~ 1.5 month) experiment turns out to be effective for the ambient noise and receiver function studies, and may serve as a prototype experiment that will allow basins to be covered by this type of low-cost survey.

In Chapter 2, we performed detailed analyses on the multi-component cross-correlations across the LA Basin. In particular, we show the existence of strong higher-mode Rayleigh waves due to the basin structure. The particle motions provide a good test for distinguishing between the fundamental and higher mode.

In Chapter 3, we combined the ambient-noise surface waves with receiver functions to measure the shape and velocity structure of the LA Basin. We also determined the Moho variation beneath the basin that was previously unknown. The density of the array was essential for the receiver function analysis in the basin environment.

1.2 Peruvian subduction zone

Southern Peru is an interesting area to study subduction and the related volcanism processes along an active continental margin. The dip of the subducted Nazca slab changes from $\sim 30^\circ$ in the southeast to nearly horizontal at a depth of ~ 100 km in the northwest. The so-called “flat slab” then spans over 1500 km distance along strike to the northwest. The Peruvian flat subduction is not unique, as approximately 10 percent of present day subduction zones are considered to have flat slabs (Gutscher et al., 2000; Skinner and Clayton, 2013). Various segments of the present normal subduction regimes of South America have also experienced flat subduction episodes in the past (Mamani et al., 2010; O’Driscoll et al., 2012; Ramos and Folguera, 2009).

However, among several mechanisms that can potentially transform a normal dipping slab into the flat geometry (Gutscher, 2002; Manea et al., 2012; O’Driscoll et al., 2012), the dominant one is still not clear. Distinguishing between the structure of flat and normal subduction zones is important for understanding the mechanisms as well as consequences of the flat subduction.

Located in the northern Central Andes, Southern Peru is also characterized by an over 4 km high mountain belt. The tectonic shortening since around 30-40 Ma cannot fully explain the high and flat plateau of the Central Andes, as well as the 70 km thick crust (Oncken et al., 2006; Husson and Sempere, 2003). Other tectonic activities have also modified the orogenic process. A low-velocity zone has been widely observed in the mid-crust, and is interpreted as a large volume of partially molten rocks (Schilling et al., 2006; Yuan et al., 2000; Ward et al., 2013). The magmatic addition from the mantle, although not significant in thickening the crust (Mamani et al., 2010; Schilling et al., 2006), contributes heat, which induces the crustal melting and lowers the viscosity of the mid-lower crust, and therefore controls the mechanical behavior of the crust. The crustal flow from the Western and Eastern Cordillera may have thickened the Altiplano Plateau (Husson and Sempere, 2003). The underthrusting Brazilian Shield that has been imaged (Phillips et al., 2012; Phillips and Clayton, 2014; Lamb et al., 1996) may have also contributed to the crustal thickening. These recent geophysical observations have unveiled the deep structures, and are important for understanding the series of tectonic events that have built the Central Andes.

In Chapters 4-6, we explored the crust and uppermost mantle structure beneath Southern Peru, using data primarily from the PeruSE experiment, which is a box-like seismic array deployed progressively from June 2008 to February 2013 (PeruSE, 2013). The results revealed interesting structures related to the subduction, orogeny, and volcanism processes.

In Chapter 4, we performed detailed analyses on some unusual signals in the ambient-noise cross-correlations: precursor and coda waves relative to the interstation Rayleigh wave. We modeled them with a strong scatterer that is located in the active volcanic area.

In Chapter 5, we used ambient noise and earthquake surface waves to constrain the shear velocity structure of the crust and uppermost mantle. We show the extent of the mid-crust Andean low-velocity zone in the study region, the two lithospheric blocks across the Cusco-Vilcanota Fault System, and the velocity differences between the flat and normal subduction regimes.

In Chapter 6, we focused on the flat subduction regime, and imaged the structures of the oceanic Moho, the continental Moho, and the mid-crust structures (molten rocks and Brazilian Shield) using receiver function and surface wave methods. In particular, we show that the shape of the flat slab correlates with the topography of the continental Moho above, which indicates that the interplate suction force is likely the dominant force in the development of flat subduction.

Part I

LASSIE: Los Angeles Syncline Seismic Interferometry Experiment

Chapter 2

Higher-mode ambient-noise Rayleigh waves in sedimentary basins

2.1 Abstract

We show that higher modes are an important component of high-frequency Rayleigh waves in the cross-correlations over sedimentary basins. The particle motions provide a good test for distinguishing the fundamental mode from the higher mode, with the fundamental mode having retrograde motion and the higher mode having prograde motion in the 1-10 s period of interest. It is important to correctly identify the mode order when inverting the dispersion curves, because misidentifying the higher mode as fundamental will lead to an anomalous high V_{SV} velocity. The basement depth controls the cut-off period, above which the higher mode is evanescent that coincides with a rapid increase in the ellipticity or H/V ratio of the fundamental mode. The relative amplitude of the higher and fundamental mode in the cross-correlation is not only determined by the Green's function, but also the noise source distribution, especially in the partitioning between source force components.

2.2 Introduction

Determining the basin structure is important for evaluating the potential seismic hazard because basins trap and amplify strong motion energy (Olsen, 2000; Komatitsch et al., 2004). The Los Angeles Basin is a typical example of this, where there have

been many studies on its structure (Lee et al., 2014; Fuis et al., 2001; Shaw et al., 2015; Tape et al., 2009; Süs and Shaw, 2003; Hauksson and Haase, 1997), using data from both passive and active seismic experiments, as well as well-logs and reflection data from the oil industry. The culmination of these efforts has been the creation of a series of steadily improving Community Velocity Models (Plesch et al., 2011; Kohler et al., 2003), which are used in the simulation of ground motions from scenario earthquakes.

Methods based on ambient noise cross-correlation (Yao et al., 2006; Lin et al., 2008; Shapiro et al., 2005; Lin et al., 2014) have been an important development in building basin models. With a dense recording array, both high-frequency surface waves (Lin et al., 2013; Shirzad and Shomali, 2014; Fang et al., 2015) and body wave signals (Nakata et al., 2015) can be extracted, and used to determine the structure. The ellipticity of the Rayleigh wave is also being used to infer the depth of the basin (Savage et al., 2013). The generation of empirical Green’s functions by correlation can be used to generate scenario earthquakes, which when compared to numerical simulations, can be used to test the basin models (Denolle et al., 2014, 2013).

One problem that arises when using ambient noise surface waves to determine structure of basins is the presence of higher modes. The standard analysis generally assumes that the fundamental mode is dominant in the vertical component cross-correlations. While this is generally true for regional scale surveys, the higher-mode Rayleigh wave can also be strong (Rivet et al., 2015; Savage et al., 2013). A misidentification of the mode will lead to a higher V_{SV} and incorrect anisotropy estimates (V_{SV} vs. V_{SH}), as well as incorrect amplitude information.

In this paper, we analyze surface waves generated by ambient noise correlations using data from a dense broadband array that was deployed across the Los Angeles Basin. The density of the array allows us to clearly see the modes and to measure their properties. The actual model of the basin that is determined will be the subject of another paper where the surface wave dispersion curves are combined with receiver functions to measure the shape and velocity structure of the Los Angeles Basin.

A Dense Broadband Array Across the Los Angeles Basin

To study the structure of the LA Basin, we have deployed a dense array of three-component broadband seismometers across it (Figs. 2.1 and 2.2). Of particular interest in this paper are 44 (of 73) stations that are deployed in a linear array with ~ 1 km interstation distance. They were operational from September to November 2014, with an average recording time of about 40 days. This “high-density short-duration” experiment, named the “Los Angeles Syncline Seismic Interferometry Experiment” (LASSIE), turns out to be effective for the ambient noise studies that will be shown. This type of array may serve as a prototype experiment that will allow basins to be covered by this type of low-cost short-duration survey.

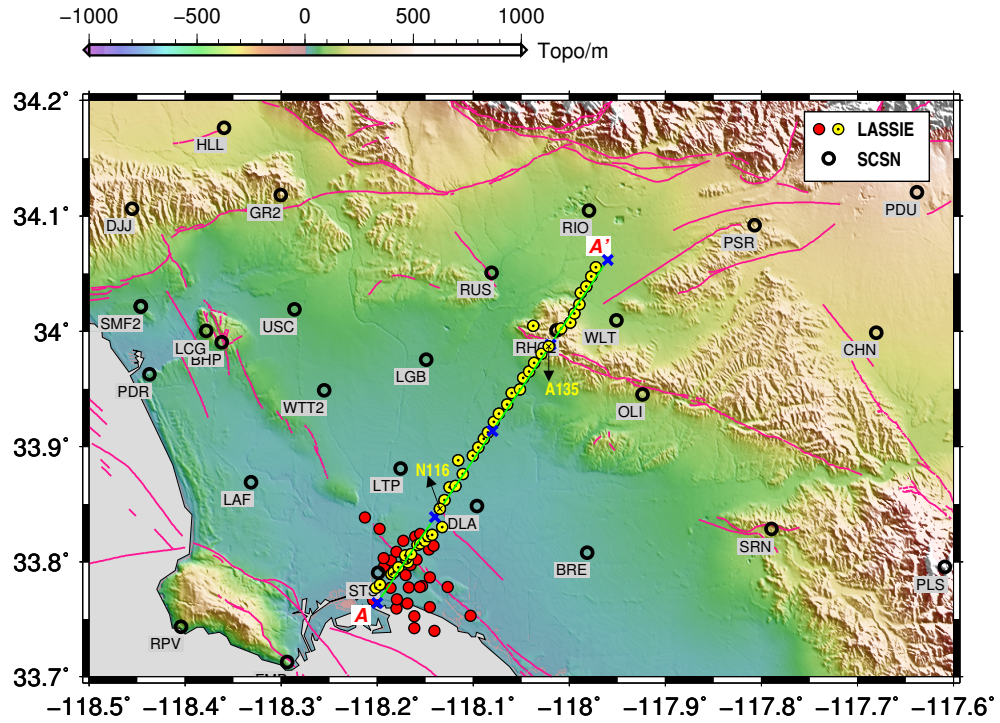


Figure 2.1: The LASSIE array. The red and yellow dots are LASSIE stations, and the black circles are SCSN stations. The green line denotes the location of the 2-D profile (A-A'), and the distances from “A” are marked with blue crosses in 10 km intervals. The faults are shown with pink lines (from Jennings and Bryant (2010)).

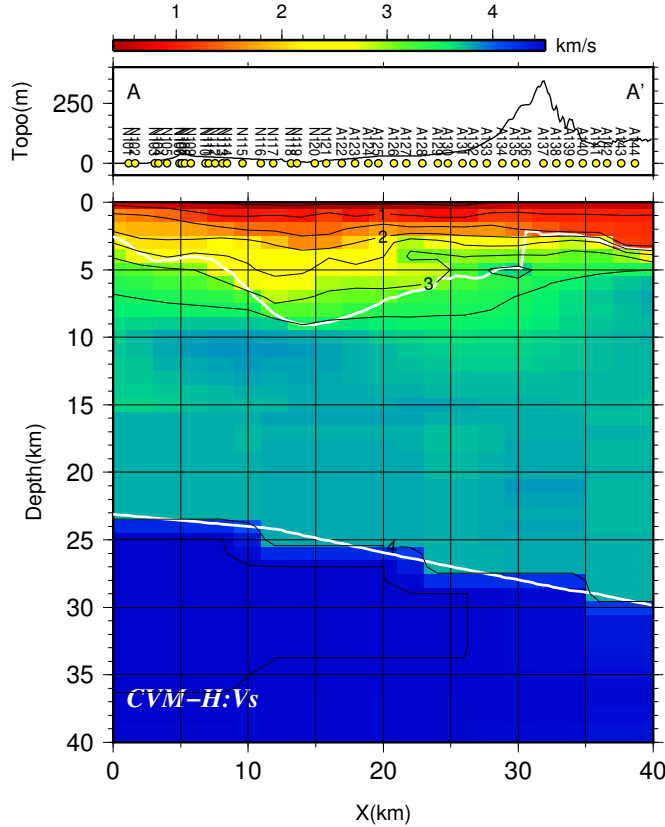


Figure 2.2: CVM-H model along A-A' profile. The white lines delineate the basement and the Moho depths. The Puente Hills is at ~ 30 km distance, and separates the Los Angeles Basin (LAB) to the south and the San Gabriel Valley (SGV) to the north.

2.3 Multi-component cross-correlations

Following methods of [Bensen et al. \(2007\)](#) and [Lin et al. \(2014\)](#), we perform cross-correlations between all three components of each pair of stations. The data (cut to 1-day segments) for each station are pre-processed before the cross-correlations. As in [Lin et al. \(2014\)](#), the same trace is used for all the three components in the time domain normalization or spectral whitening steps in the pre-processing, so that the H/V (R/Z) ratio is preserved for each Rayleigh wave arrival. The Rayleigh wave H/V ratio is a site property ([Tanimoto and Rivera, 2008](#); [Yano et al., 2009](#); [Lin et al., 2014](#)),

and therefore is same for all the Rayleigh wave arrivals over time regardless of their propagation paths. This guarantees that the Rayleigh wave in the cross-correlation (for example, measured from Z-R and Z-Z cross-correlations) also preserves the H/V ratio (see [sec. 2.6](#)).

2.3.1 Love wave

In [Fig. 2.3](#), we show the cross-correlation results (filtered to 1- and 5-s period) between the tangential (T) component of station N116 and all the yellow-dot stations in [Fig. 2.1](#). We observe clear Love wave signals along the profile, except in the 1-s period profile for those stations located at a distance beyond 30 km. Note that the Puente Hills is located at the 30 km point in the A-A' profile, and separates the Los Angeles Basin from the San Gabriel Valley to the north. The noisy signals are likely due to the scattering effect of the topography, which can produce strong precursor and coda waves ([Ma et al., 2013](#)).

The dispersion measurement for the Love wave is comparatively simple. We measure the phase velocity dispersion curves from 1 to 10-s period, using the FTAN method ([Lin et al., 2008](#); [Bensen et al., 2007](#)). The 2π ambiguity is more difficult to resolve for shorter periods compared to regional-scale studies, which use periods longer than 5 s (e.g., [Yao et al. \(2006\)](#)). We solve this by tracking the dispersion curve from long period to short period, and use the group velocity ($U = \partial w / \partial k$) to guide the instantaneous slope of the dispersion curve. The tomographic inversion result using the method of [Barmin et al. \(2001\)](#) is shown in [Fig. 2.4](#). The Los Angeles Basin and the San Gabriel Valley are evident in the tomographic images.

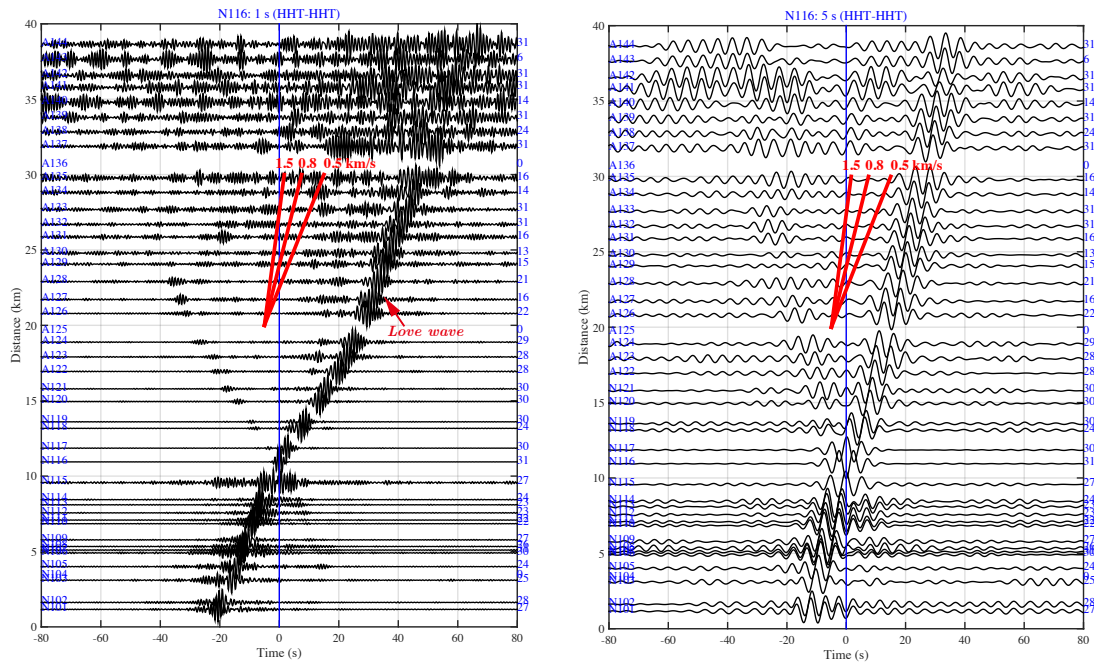


Figure 2.3: Love waves shown in the tangential-component cross-correlations between N116 and all the yellow stations in Fig. 2.1. The cross-correlations filtered to 1 and 5-s period are shown as examples. The asymmetry of the cross-correlations is due to the asymmetry of the noise source amplitude, which is strong to the south.

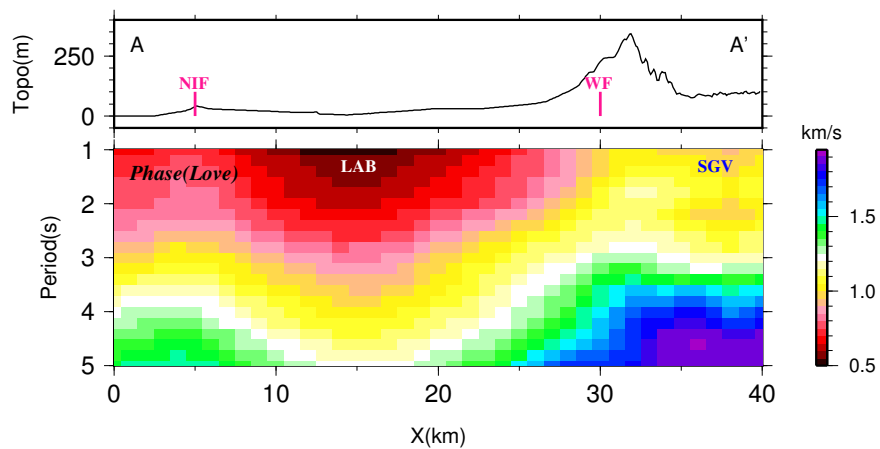


Figure 2.4: Tomographic inversion result along A-A' profile (Fig. 2.1) with measured Love wave dispersion curves. The y-axis is the period. The Los Angeles Basin (LAB) and San Gabriel Valley (SGV) are shown as low velocities. The Newport-Inglewood Fault (NIF) and Whittier Fault (WF) are shown.

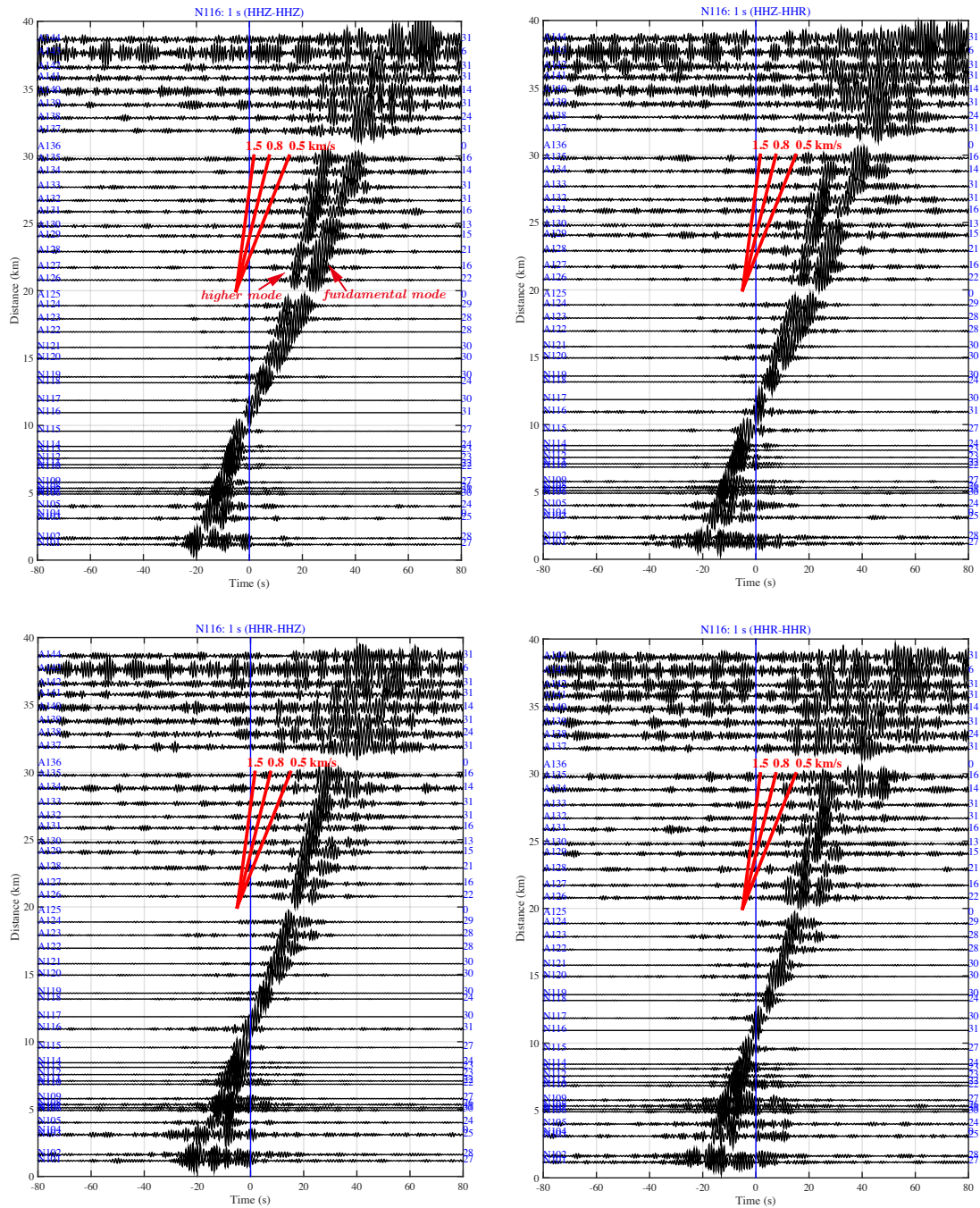
2.3.2 Rayleigh wave

In Figs. 2.5a to 2.5c, we show the Z-Z, Z-R, R-R, and R-Z cross-correlations between station N116 and all the linear-array stations (yellow dots in Fig. 2.1), filtered to 1, 3, and 5-s periods. In the 1-s period profiles (Fig. 2.5a), we see that the fundamental and higher-mode Rayleigh waves are equally strong with a Z-directed force at N116 (i.e., Z-Z and Z-R cross-correlations). The higher mode is even stronger than the fundamental mode with a R-directed force at N116 (i.e., R-Z and R-R cross-correlations). In the 3-s period profiles (Fig. 2.5b), the fundamental mode is only visible with a Z-directed force at N116 (i.e., Z-Z and Z-R cross-correlations) for stations in the Los Angeles Basin (distances less than 30 km). For stations in the San Gabriel Valley (distance larger than 30 km), the fundamental mode is only visible in Z-R cross-correlations (Z-directed force, R response). While the higher mode dominates at 3-s period (Fig. 2.5b), it is evanescent in the 5-s period profiles (Fig. 2.5c), where only the fundamental mode is observed.

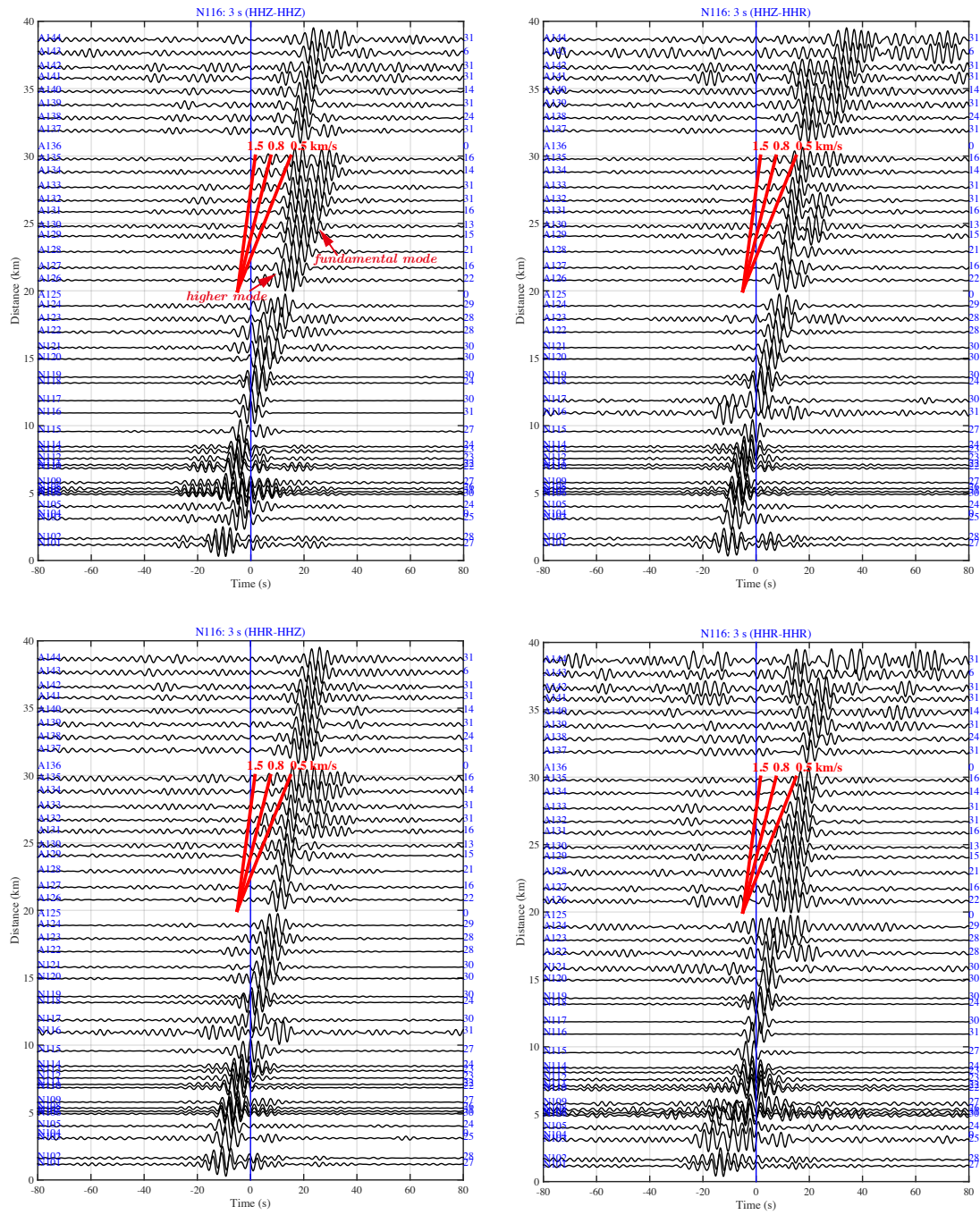
Using the multi-component cross-correlations between two stations, we can show the particle motion of the two modes at the two station sites. We stack the positive and negative lags of the cross-correlations to approximate the Green's function. We take the cross-correlations between N116 and A135 as an example. N116 is located in the basin while A135 is in the Puente Hills (Figs. 2.1 and 2.2). Tab. 2.1 shows the pairs of cross-correlations used for each particle motion measurement. For example, using Z-Z and Z-R cross-correlations, which correspond to a Z-directed force at N116, we can measure the particle motion at A135. Using the Z-Z and R-Z cross-correlations, which correspond to a Z-directed force at A135, we can measure the particle motion at N116. Note that the sign of the R-Z cross-correlation needs to be inverted since the R direction (from A135 to N116) is opposite to that in the cross-correlation (from N116 to A135).

Figs. 2.6a and 2.6b show the particle motions measured for different modes at different periods. The measurements from Z and R source directions give similar results. We only do the measurement when clear signals in the cross-correlation pair

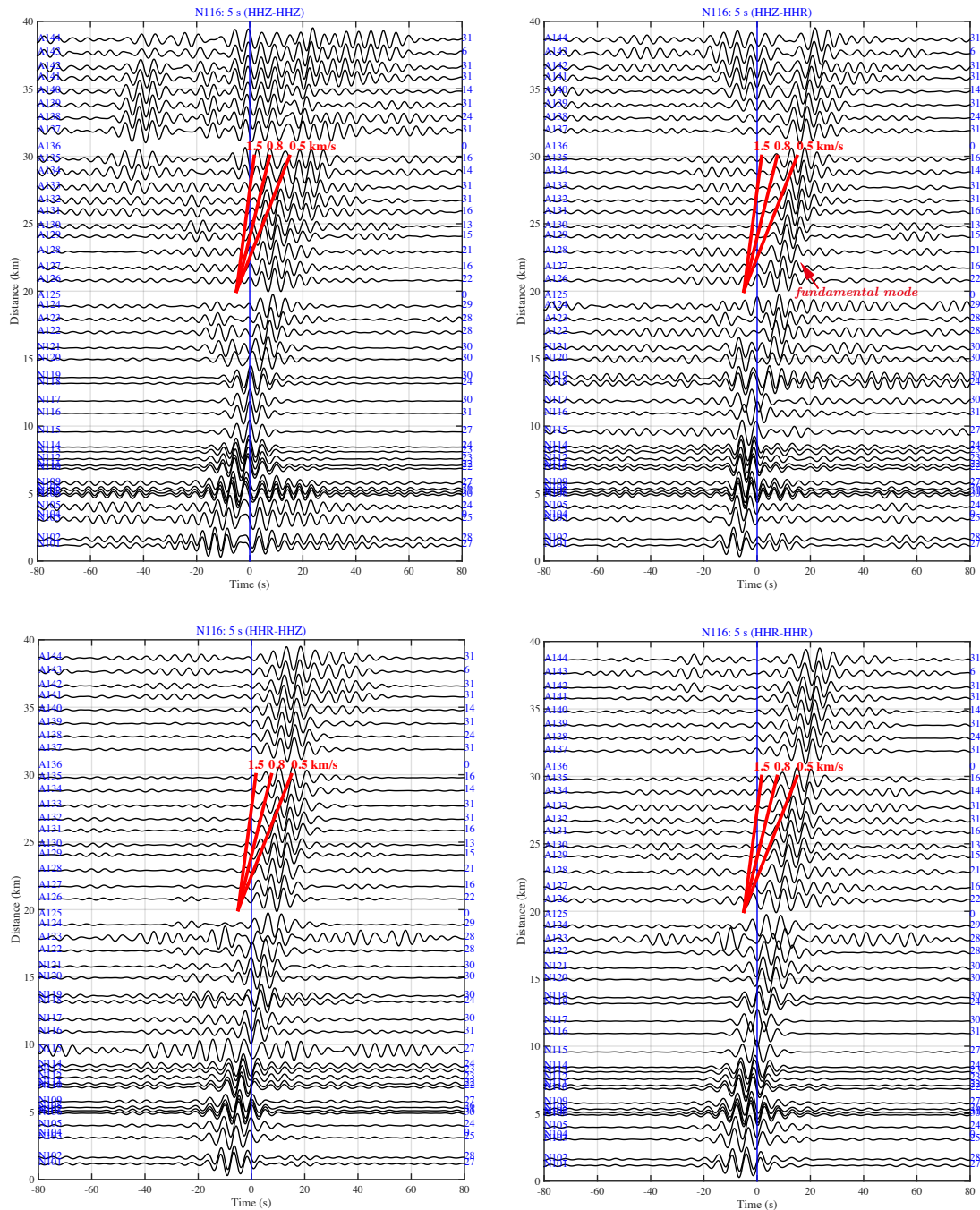
are evident. We observe that (1) the higher mode shows prograde particle motion, while the fundamental mode is retrograde, and (2) the higher mode disappears around 4 s, and above this “cut-off period” the fundamental mode in the basin (N116) shows high ellipticity or H/V ratio. There is a gap in our measurements at the cut-off period, because we cannot observe clear signals arriving at same time (same mode) in the cross-correlation pairs.



(a)



(b)



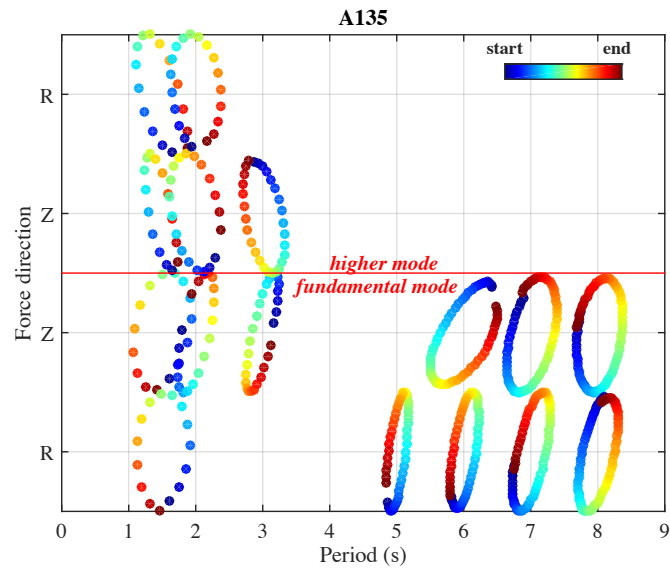
(c)

Figure 2.5: Rayleigh waves shown in the vertical and radial component cross-correlations (Z-Z, Z-R, R-Z, and R-R) between N116 and all the yellow stations in Fig. 2.1. (a) Filtered to 1-s period. Both fundamental and higher modes are strong. (b) Filtered to 3-s period. The higher mode is generally stronger in the four profiles. (c) Filtered to 5-s period. Only the fundamental mode is observed.

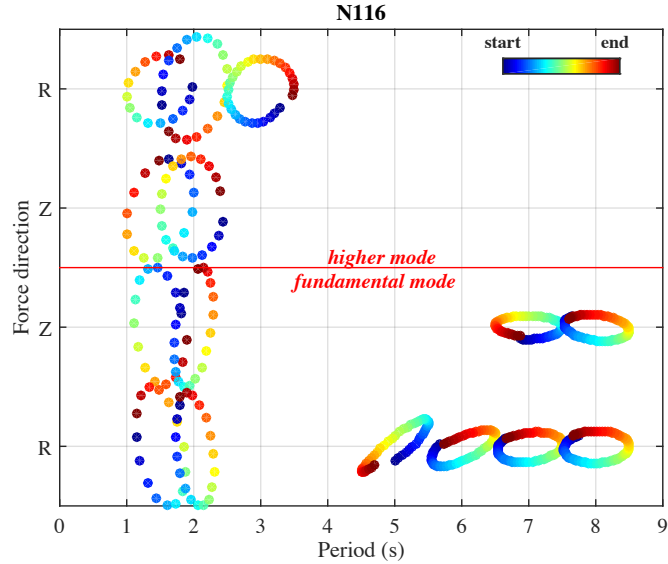
Site \ Corr	Z-Z	Z-R	R-Z	R-R
A135				
N116		*	*	
	Z force			
	R force			

* Means the trace is multiplied by -1 to adjust the R direction

Table 2.1: Cross-correlation pairs used for measuring particle motion.



(a)



(b)

Figure 2.6: Particle motion measurements using the cross-correlations (Z-Z, Z-R, R-Z and R-R) between N116 and A135. [Tab. 2.1](#) shows the cross-correlation pair used for each measurement. For each period, we have a maximum of four measurements corresponding to the two force directions (Z-Z/Z-R pair, or R-Z/R-R pair) and two modes. We only measure the particle motion when the phase is clear. We observe that the higher mode disappears above ~ 4 -s period. The higher mode has a prograde particle motion, while the fundamental mode has a retrograde particle motion. A rapid increase in the ellipticity (H/V) of the fundamental mode around 4-s period is observed at N116.

2.4 Numerical investigations on Rayleigh wave in a basin model

2.4.1 1-D model

The Rayleigh wave Green's function in a 1-D layered structure is ([Aki and Richards, 2002](#)):

$$\begin{aligned}
G &= \begin{bmatrix} G_{RR} & G_{RZ} \\ G_{ZR} & G_{ZZ} \end{bmatrix} \\
&= \sum_n \frac{1}{8cUI_1} \begin{bmatrix} r_1(z)r_1(h) & -ir_1(z)r_2(h) \\ ir_2(z)r_1(h) & r_2(z)r_2(h) \end{bmatrix} \times \left(\frac{2}{\pi k_n \Delta} \right)^{1/2} \exp \left[i(k_n \Delta + \frac{\pi}{4}) \right]
\end{aligned} \tag{2.1}$$

where n denotes the n th mode, h is the depth of the point source, z is the depth of the receiver, Δ is the distance between source and receiver; r_1 and r_2 are the horizontal and vertical displacement eigenfunctions, k_n is the wavenumber of the n th mode, c and U are the phase and group velocity (of the n th mode) respectively, and $I_1 = \frac{1}{2} \int_0^\infty \rho (r_1^2 + r_2^2) dz$ is the energy integral.

We see that for each mode, the particle motion ellipse is determined by $r_1(z=0)$ and $r_2(z=0)$ at the station, and the dependence of the wave amplitude on the source depth or direction is also controlled by the eigenfunctions $r_1(h)$ or $r_2(h)$. Using the program from [Herrmann and Ammon \(2002\)](#), we can calculate the eigenfunctions and ellipticity for different 1-D basin models. An example for a simple basin model with parameters described in [Tab. 2.2](#) is shown in [Figs. 2.7](#) and [2.8](#). The basement depth of 4 km is comparable to the average of the study region. It is shallower than that beneath N116 in CVM-H model (~ 7 km, [Fig. 2.2](#)), but better fits the 4-s cut-off period of the higher mode.

From the eigenfunctions at 3-s period ([Fig. 2.7](#)), we see that the particle motion at the surface differs in sign for the two modes. In addition, we see that the R-directed force can generate a stronger higher mode than Z-directed force, especially at deeper depths. The ellipticity over 1-10 s periods is shown in [Fig. 2.8](#). In [Fig. 2.12](#), we show similar plots for models with 6 and 8-km basement depths, and we see that distinct from the retrograde particle motion of the fundamental mode, the higher mode shows a prograde particle motion. The retrograde particle motion of higher mode only appears in the short period end (around 1-s period) in the 8-km depth

basement model (Fig. 2.12b). Therefore, the difference in the direction of particle motion, as is also evident in the data, can be useful to distinguish between the two modes in the 1-10 s period of interest. We also notice that at ~ 4 -s period, the higher mode disappears, which means no k_1 is found for the eigenproblem, as shown by the truncation of the dispersion curve, and the ellipticity of the fundamental mode suddenly increases, as we also observe in the data.

To show the relative strengths of the two modes, we use the FK method (Zhu and Rivera, 2002) to compute synthetics for the model in Tab. 2.2. One could also use the modal solution given above, with the eigenfunctions and the normalization terms (I_1 , c , $U\dots$) calculated for each mode, but the computation is easier with the FK method. Fig. 2.9 shows the result (filtered to 3-s period) for a point source (R or Z direction) with central period of 3 s at 0.5 km depth. We see that the higher mode is dominant with an R-directed force (R-Z and R-R profiles), while the fundamental mode is dominant with a Z-directed force (Z-Z and Z-R profiles). We see that for noise sources with different force components or source depths (from Fig. 2.7), the relative amplitude of the fundamental and higher-mode Rayleigh wave are different. Since the cross-correlation is a summation of the contributions over the noise sources, the relative amplitude of the two modes is not only controlled by the structure between the two stations or the channels used in the cross-correlations (i.e., the Green’s function), but also by the noise source distribution. We therefore cannot use the relative amplitude of the two modes in the cross-correlation to infer the Green’s function.

	H(km)	V_S (km/s)	V_P (km/s)	Rho(g/cm ³)
Sediments	4	1.0-3.0 (gradient)	2.5-5.0	2.0-2.5
Half space		3.8	6.5	2.8

Table 2.2: 1-D basin model.

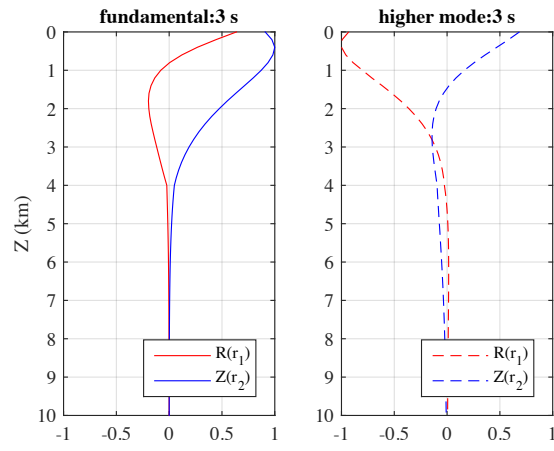


Figure 2.7: The eigenfunction of 3-s period Rayleigh wave calculated for the basin model in [Tab. 2.2](#). The eigenfunctions are normalized for each mode.

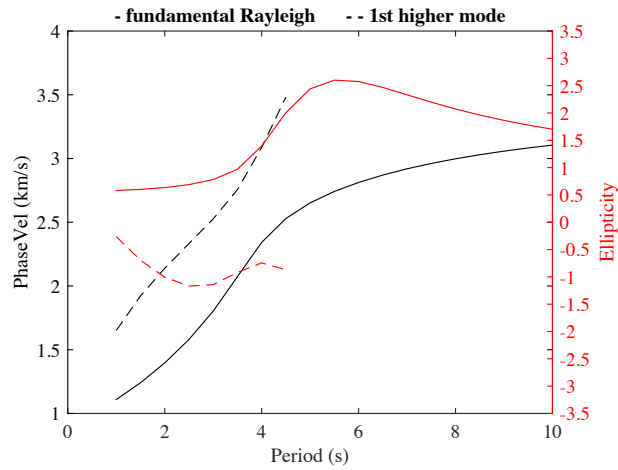


Figure 2.8: The dispersion curve and ellipticity for fundamental and 1st higher mode Rayleigh wave in 1-10 s period, calculated for a basin model in [Tab. 2.2](#). Note the different direction of particle motion between fundamental and higher mode. The higher mode is evanescent above about 4.5-s period, along with a rapid increase in the ellipticity of the fundamental mode.

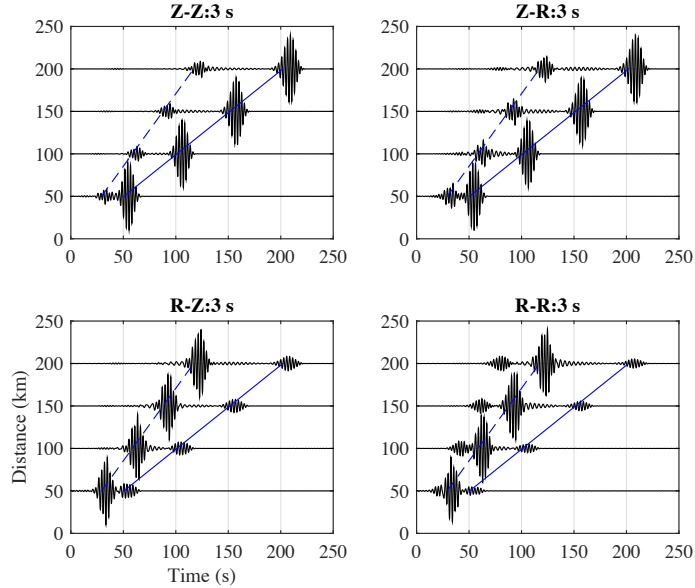


Figure 2.9: The FK synthetics on the waveform in a 1-D structure (Tab. 2.2). The source is at 0.5 km depth with a central period of 3 s. The waveforms are filtered to 3-s period. The top two panels show the Z and R recordings with a Z source. The bottom two panels show the results for R source.

2.4.2 2-D model

Since the H/V ratio is a site property, we have explored the particle motion of the Rayleigh wave in a 1-D structure so far. Here, we extend this to model the surface wave propagation in a 2-D structure and measure the H/V ratios along the profile. The example illustrates that the H/V ratio is indeed a site property in a large scale, but the lateral variations in structure do add complexities to it.

We use a finite-difference program (Li et al., 2014) to simulate the wave propagation in a 2-D basin structure. The background model is the same as the 1-D basin model used in section 2.4.1 (Tab. 2.2). We add an inverted-triangle shape basin at 100-110 km distance (Fig. 2.10), so that the basement depth increases from 4 km in the background model to 9 km at 105 km distance. An explosion source is placed at 0 km distance and 0.5 km depth, with a Gaussian shape source time function centered

at ~ 4 Hz. The grid space is 0.05 km, and time step is 0.002 s.

In the synthetic seismogram (Fig. 2.13, before and after filtering to 1-10 s), we noticed strong body wave signals arriving ahead of the surface wave. The predicted group arrival time for 3 and 4-s period surface wave is plotted, which suggests that muting the body waves will affect periods longer than 3 s. Therefore, after muting the body waves, we only measure the H/V ratio (the ratio of the peak of the envelope) for period no longer than 3 s. We also cannot get a reliable measurement at high frequency (~ 1 s) because of the approximation that the FD method uses for the free surface, which requires a very small grid size and thus enormous computing power to achieve accuracy (as we see the error does decrease with grid size). In Fig. 2.10, we show the measurements for 2 and 3-s period along the profile, as well as the predictions on the local 1-D structure as in section 2.4.1.

For 3-s period, we see that inside of the basin, the 2-D result shows the same trend as the 1-D prediction, but the number differs a lot. The fit is even worse at 110-120 km distance. It might not be surprising that the surface wave behaves differently from 1-D prediction considering the finite frequency effects and body wave contamination with the sharp variations in this model. In the distance range less than 100 km or larger than 125 km, the 2-D result is consistent with the 1-D prediction. The result suggests that the peculiar basin structure (100-110 km) does not affect the H/V ratio of the Rayleigh wave after passing the structure and propagates for another 15 km. 2-s period shows the similar case as 3-s period. Thus, the H/V ratio is indeed a site property in a large scale, although the sharp variation in the structure can affect this assumption.

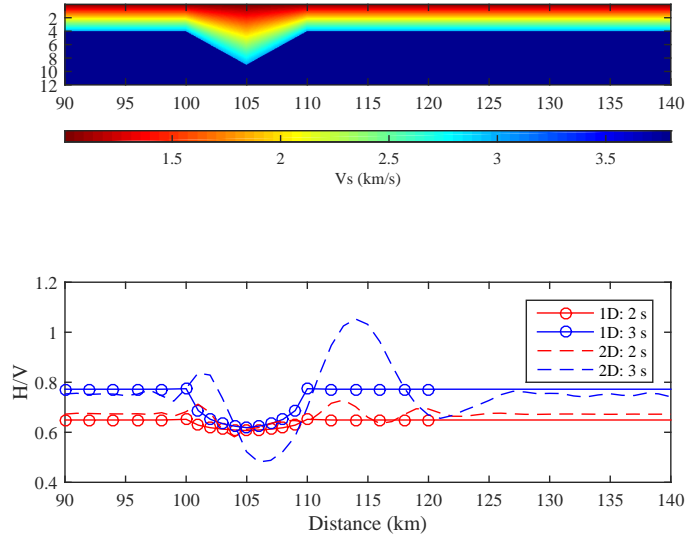


Figure 2.10: (Top panel) 2-D model for the FD modeling. The source is at 0 km distance. (Bottom panel) The H/V ratio measured from the waveforms (dashed line) and that predicted from the local 1-D structure (solid line). Result at 2 and 3-s period shows that the H/V ratio is a site property in a large scale, but sharp variations in the structure do add complexities to it.

2.5 Discussions and Conclusions

We see that with about 1-km interstation distance, we can extract strong surface wave signals as high as 1-s period. The shorter period surface wave is sensitive to shallower depths, and therefore it is very useful to image the basin structures. Love wave signals are comparatively simple for dispersion analysis (Figs. 2.3 and 2.4), but strong higher-mode Rayleigh waves in the basin (e.g. Fig. 2.5a) complicate the use of Rayleigh waves. Rivet et al. (2015) recently proposed to use the H/V ratio to distinguish between the modes. Their work involves inverting the dispersion curve for the V_S model assuming separate cases as to whether the Rayleigh wave is a fundamental or higher mode. The H/V ratios (over a range of periods) are then calculated for the two cases, and the one that best matches the data is chosen. In contrast, our proposed

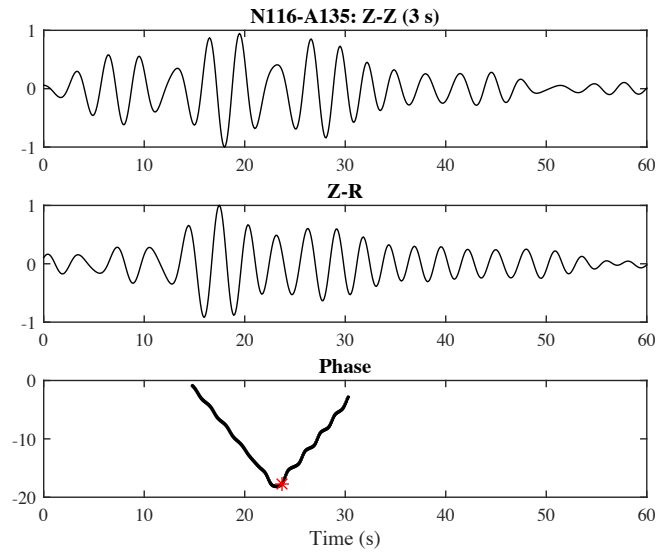
method distinguishes the two modes directly by measuring particle motion from the data.

It's not necessary to plot the particle motion ellipse in order to distinguish the modes. In Figs. 2.11a and 2.11b, we show the examples using the Z-Z and Z-R cross-correlations between N116 and A135. We plot the (unwrapped) instantaneous phase $\phi(t) = \arg(r(t) + iz(t))$, with a 5-point (0.5 s) moving-window smoothing. We then calculate the instantaneous curvature $\phi''(t)$. The time t^* , which corresponds to the maximum of $\phi''(t)$, is where the two modes separate. The slope of $\phi(t)$ should be negative for $t < t^*$ (higher mode) and is positive for $t > t^*$ (fundamental mode) (Fig. 2.11a). If we only observe one mode then we can deduce its type by the slope (Fig. 2.11b).

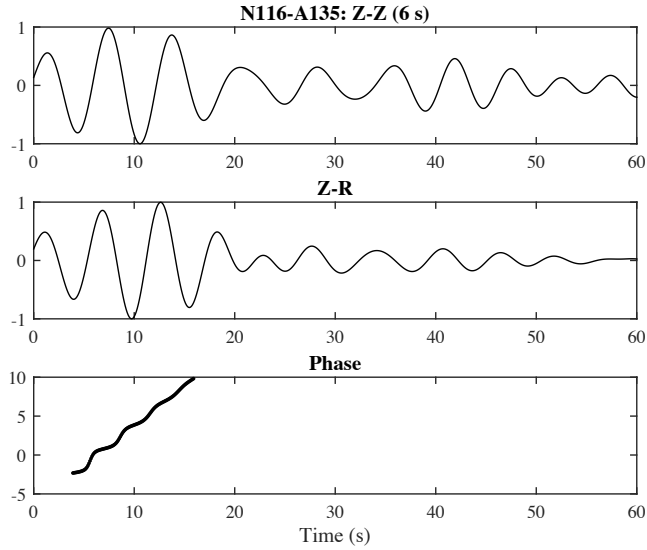
The cut-off period (T_0), above which the higher mode disappears, coincides with the rapid increase in the fundamental mode ellipticity (H/V) and is close to the period ($T_1 = 1/f_1$) with the peak H/V ratio. The frequency f_1 is related to the resonance frequency f^* of the basin (Boaga et al., 2013; Field and Jacob, 1993; Fäh et al., 2001; Nakamura, 1989). Therefore, the basement depth can be estimated as $h = V_s/2f_1$. For the synthetic model in section 2.4.1, $T_1 \approx 5.5$ s ($T_0 \approx 4$ s), using the average velocity of the sediments as $V_s = 2.0$ km/s (Tab. 2.2), the basement depth is estimated to be 5.5 km. It is a bit deeper than the actual 4.0 km depth, possibly because the formula is for constructive interference between vertical rays, while the h can be smaller for non-vertical rays. The data in section 2.3.2 also shows $T_1 \approx 5$ s ($T_0 \approx 4$ s), the estimated basement depth as 5 km is quite close to the average basement depth in CVM-H model (Fig. 2.2). Alternatively, we can estimate the period in which the higher mode exists from the known basement depth measured from other methods, like receiver functions.

The strong higher mode (compared with the fundamental) we observed is not only due to the low-velocity sedimentary layer, but also the contribution from the R-directed noise source, since the Z-directed source does not generate a higher mode that is equally strong with the fundamental. The basin edge scattering could have acted as the R-directed noise source, and because of the \sqrt{r} decay of the surface wave, given

same intensity, its contribution can be much larger than distant Z-directed sources from the ocean. Therefore, the relative amplitude of the two modes in the cross-correlation cannot be used to infer the Green's function between the two stations.



(a)



(b)

Figure 2.11: An example to distinguish the two modes using Z-Z and Z-R cross-correlations between N116 and A135. (a) At 3-s period. Both higher and fundamental modes are observed. The separation time corresponds to the maximum curvature point in the phase plot. (b) At 6-s period, only the fundamental mode is observed.

2.6 Supplementary material

Text S2.1: To enhance the extraction of surface wave signals, the data of each station are usually pre-processed before cross-correlation (Bensen et al., 2007; Lin et al., 2014). The time domain normalization and spectral whitening in frequency domain can modify the amplitude of the data. However, as we will show, the H/V ratio of the surface wave is preserved in these processes.

In time domain normalization, we divide all three components (Z/N/E) by the same trace, which is the smoothed envelope of the data filtered to the earthquake band (use the maximum of the three at each time point). Therefore, the arrival at a certain time t_i is scaled by the same factor (m_i) at all three components. R is the

linear combination of N and E, and therefore it is also scaled by the same factor.

The Rayleigh wave in the cross-correlation is from the contribution of all the Rayleigh wave arrivals from the noise source recorded by the two stations.

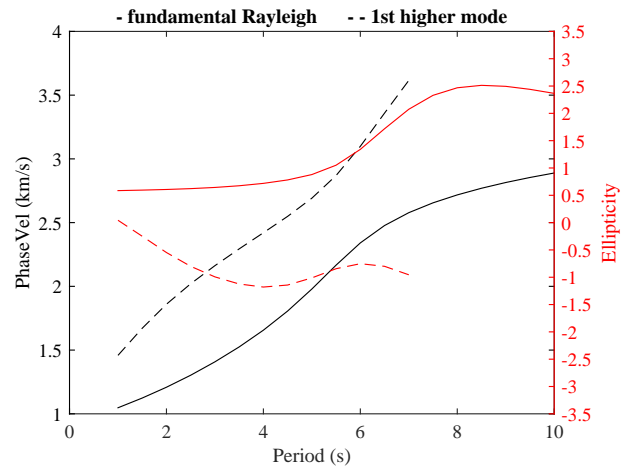
$$\frac{Z_1 R_2}{Z_1 Z_2} = \frac{\sum_{i=1}^N \frac{1}{m_{i1} m_{i2}} Z_{i1} R_{i2}}{\sum_{i=1}^N \frac{1}{m_{i1} m_{i2}} Z_{i1} Z_{i2}} \quad (2.2)$$

Since Rayleigh wave H/V (R/Z) ratio is a site property, which is controlled solely by the 1-D structure beneath the seismometer (Tanimoto and Rivera, 2008; Yano et al., 2009). Then,

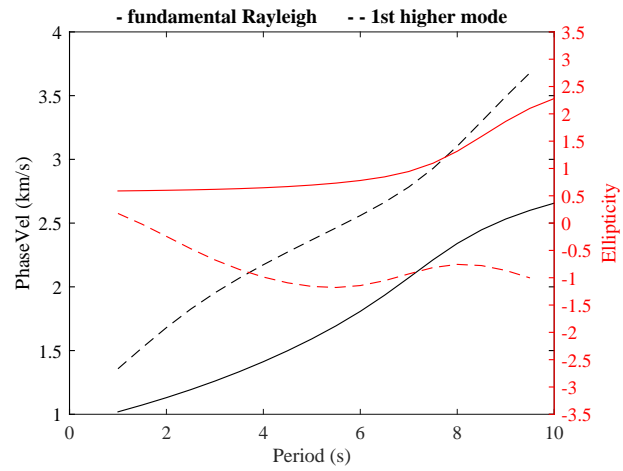
$$\frac{R_{i2}}{Z_{i2}} = k_2 \quad (2.3)$$

$$\frac{Z_1 R_2}{Z_1 Z_2} = \frac{k_2 \sum_{i=1}^N \frac{1}{m_{i1} m_{i2}} Z_{i1} Z_{i2}}{\sum_{i=1}^N \frac{1}{m_{i1} m_{i2}} Z_{i1} Z_{i2}} = k_2 \quad (2.4)$$

We see that the H/V ratio is preserved in the cross-correlation. For the spectral whitening in frequency domain, we also do the same operation to all the three components, and therefore the H/V ratio should also be preserved.

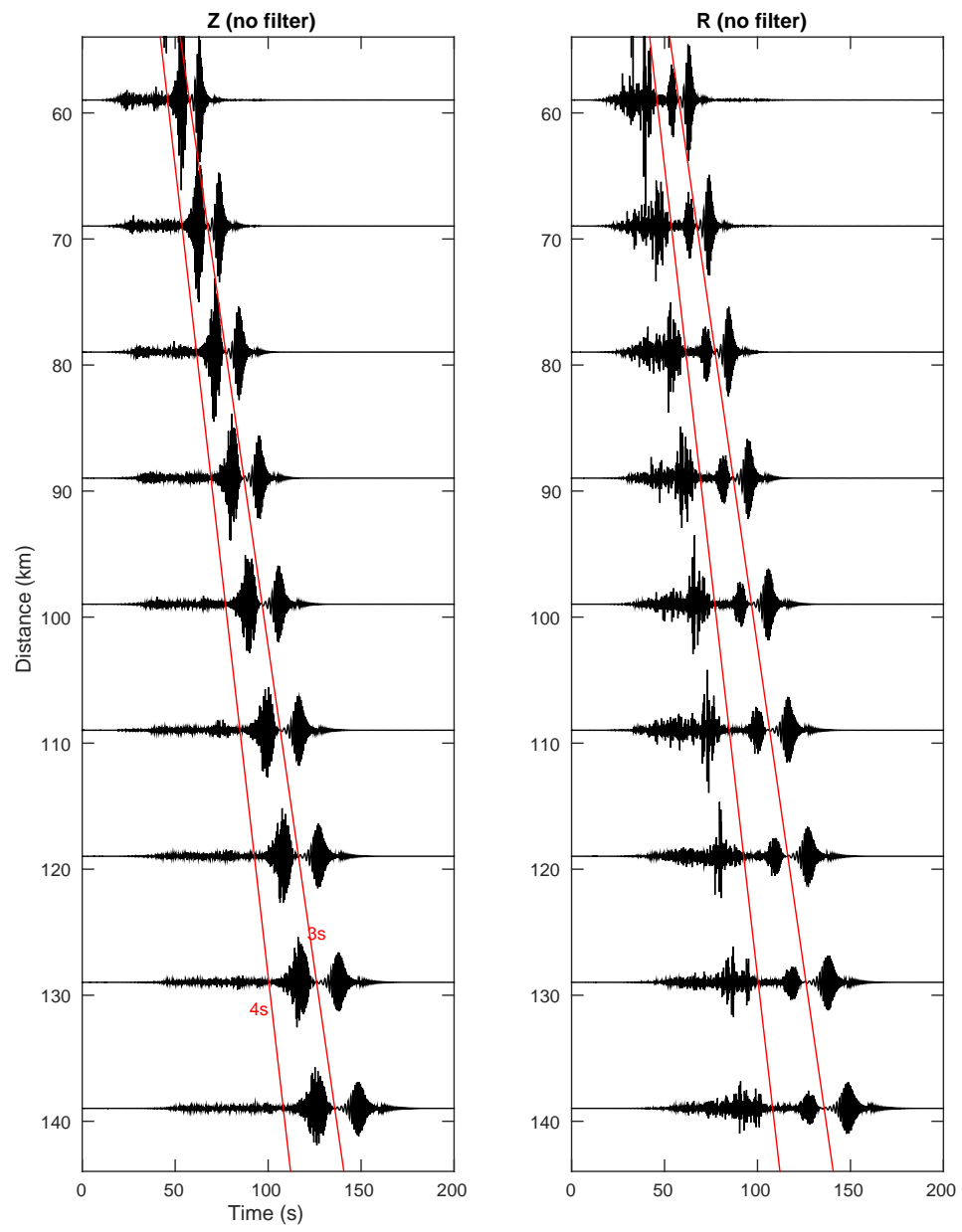


(a)

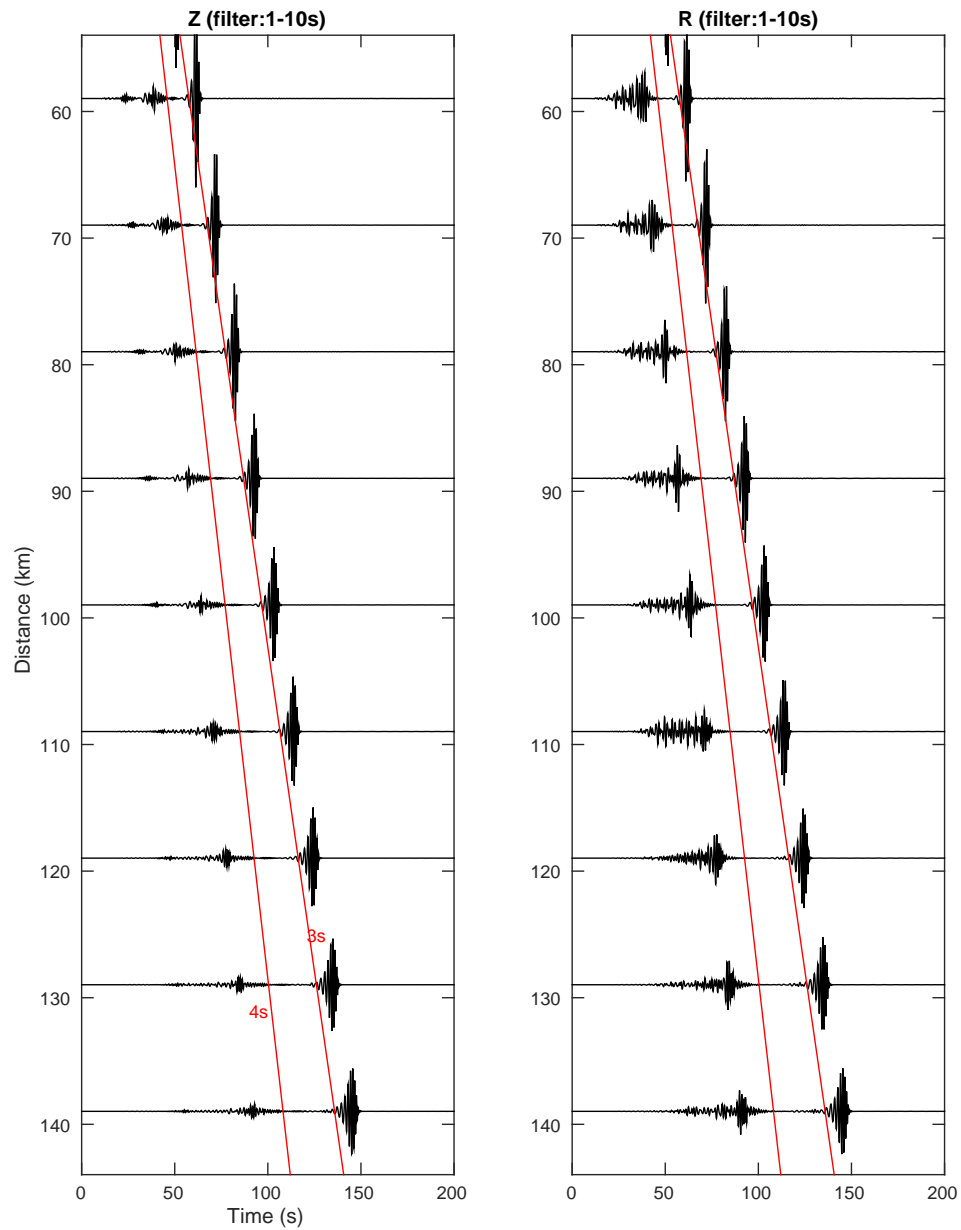


(b)

Figure 2.12: The Rayleigh wave dispersion and ellipticity calculated for a basin model with a basement at: (a) 6-km depth; (b) 8-km depth. The other model parameters are same as that in [Tab. 2.2](#).



(a)



(b)

Figure 2.13: The waveforms (before and after filtering to 1-10 s) in the FD modeling (section 2.4.2, Fig. 2.10). The strong body wave signals arriving ahead of the surface wave are muted. The red solid lines show the group arrival time of 3 and 4-s period surface waves. We see that we may only measure the surface waves up to 3 s.

Chapter 3

Structure of the Los Angeles Basin from ambient noise and receiver functions

3.1 Abstract

A velocity (V_S) and structure model is derived for the Los Angeles Basin, California based on ambient-noise surface wave and receiver function analysis, using data from a low-cost, short-duration, dense broadband survey (LASSIE) deployed across the basin. The shear wave velocities range from 0.5 to 3.0 km/s in the sediments, and show lateral gradients at the Newport-Inglewood, Compton-Los Alamitos, and Whittier Faults. The structure of the model shows that the basin is a maximum of 8 km deep along the profile, and that the Moho rises to a depth of 17 km under the basin. The basin has a stretch factor of 2.6 in the center grading to 1.3 at the edges and is in approximate isostatic equilibrium.

3.2 Introduction

The Los Angeles Basin is a Miocene-age pull-apart basin that was formed by the passing of the Pacific-Juan de Fuca-North America triple-junction by southern California (Nicholson et al., 1994; Ingersoll and Rumelhart, 1999). It has been extensively studied over the last few decades because it is a significant oil-production area, and

because it is a major concern for the seismic hazard evaluation for the area. The oil production is primarily confined to the bounding faults (Newport-Inglewood, Whittier, and Hollywood faults), and a summary of the structure determined by numerous oil-company surveys is presented in [Wright \(1991\)](#). The basin is part of the seismic hazard because the sediments trap and amplify strong motion energy, and because of its size and depth, the basin is capable of enhancing waves in the 2-5 sec range, which is particularly dangerous for high-rise buildings. Numerical modeling of these phenomena requires an accurate model of the subsurface structure and velocities that define the Los Angeles Basin.

An initial unified model for the southern California region was produced by [Magistrale et al. \(2000\)](#) with a mixture of various studies such as receiver functions ([Zhu and Kanamori, 2000](#)) and tomography ([Hauksson, 2000](#)). The basin structure was based on empirical rules applied to formation maps that were interpolated from borehole data. Another approach was used in [Süss and Shaw \(2003\)](#), where they used P-wave velocity measurements determined from stacking velocities from oil-company reflection surveys along with sonic logs from boreholes, in addition to a basin shape model based on gravity and borehole lithology observations ([McCulloh, 1960](#); [Yerkes et al., 1965](#)). These models have been combined and further enhanced through the use of full waveform inversions ([Tape et al., 2009](#); [Lee et al., 2014](#)), leading to an updated unified model ([Shaw et al., 2015](#)) including the CVM-H velocity model (currently 15.1.0 version) and the CFM fault model.

In this paper we add some additional constraints on the structure of the Los Angeles Basin and its shear wave velocities. This study is based on a new survey that was done in the fall of 2014. It consisted of a relatively dense array of broadband sensors that traversed the basin from Long Beach, through Whittier to the southern part of the San Gabriel Valley. [Fig. 3.1](#) shows the location of the experiment, which is named “Los Angeles Syncline Seismic Interferometry Experiment” (LASSIE). It includes 73 three-component broadband stations, 51 of which are deployed in a line with ~ 1 km interstation distance. They were operational from September to November 2014, with an average recording time of about 40 days. This survey is an example of what can be

done with a low-cost, short-duration, rapid-deployment style that may prove useful for conducting additional surveys to refine the basin detail.

In this study we use ambient-noise derived surface waves and receiver functions (RFs) to construct the new model. Both are traditionally thought of as not being very useful in an urban environment where the cultural noise can be overwhelming. The basin reverberations in addition add difficulties to phase recognitions in the RFs. However, as shown here, an excellent signal can be obtained and the key is to have a dense array to use lateral continuity to distinguish signals from the noise. [Fig. 3.8](#) shows the CVM-H model beneath the array. The shallow structure (less than 10 km depth) shows a lot of detail due to the P-wave velocity data from the oil industry. In contrast, it does not show any variations in the Moho except the deepening trend towards inland.

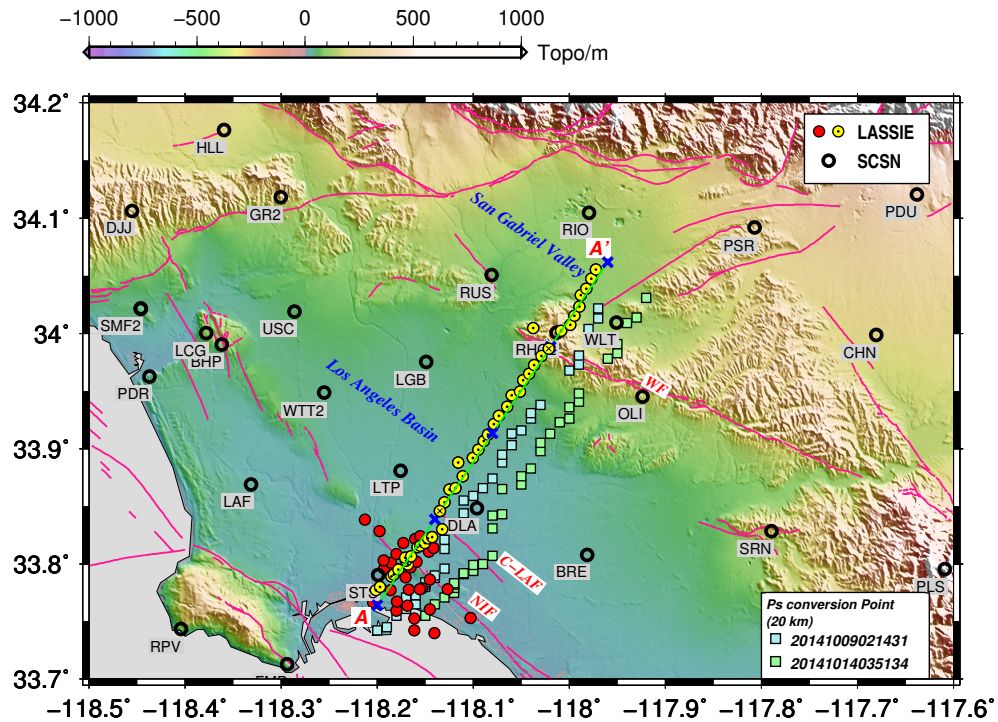


Figure 3.1: The LASSIE array. The red and yellow dots are LASSIE stations, and the black circles are SCSN stations. The green line denotes the location of the 2-D profile (A-A'), and the distances from “A” are marked with blue crosses in 10 km intervals. The faults are shown in pink lines, and some of them are annotated: NIF - Newport-Inglewood Fault, C-LAF - Compton-Los Alamitos Fault, WF - Whittier Fault. The Ps conversion points at 20 km depth (blue and green squares) are plotted for the two events used in the receiver functions (Fig. 3.2).

3.3 Receiver functions

Standard methods are used to retrieve and process the receiver functions (RFs). For each seismic event, the data are rotated to R-T-Z coordinates, and filtered to a 1-50 s pass-band. The iterative time-domain deconvolution (Ligorria and Ammon, 1999) is used to retrieve the P-to-S receiver functions (RFs). A low-pass Gaussian filter is applied with a parameter of 2.5, which means the corresponding cutoff frequency is ~ 1.2 Hz and the pulse width in the time domain is ~ 1.0 s. The events we used are

within 30-95° epicentral distance, and have a magnitude no less than 6. Two events (Tab. 3.1) with clear recordings occurred while most stations were in operation, and are used in the following processing. Their approximate Ps conversion points at 20 km depth are shown in Fig. 3.1.

The time domain RFs are shown in Fig. 3.2. The PpPs multiples corresponding to the basement depth are recognized after converting the time axis to depth using the time-depth relation for the PpPs phase (Fig. 3.9). The CCP migration result using the PpPs phase is shown in Fig. 3.3. For each station, we use the 1-D model extracted from CVM-H model at the station location as the reference model for time-depth conversion, which takes into account of the anomalously high V_p/V_s ratio for the sedimentary layer (see Fig. 3 in Brocher (2005)). An underestimation of the V_p/V_s ratio can result in a deeper depth of the structure (Zhu and Kanamori, 2000). If there was not a good reference model, we could first do the CCP migration with a model without sedimentary layer (for example, IASP91 model), and then use the RF results to update the reference model using an empirical V_p/V_s ratio for the sedimentary layer.

We observe a clear basement shape that is generally in accordance with the CVM-H model. In addition, we observe strong thinning of the crust beneath the basin, which is very different from the CVM-H model, but is more reasonable considering the large-magnitude crustal extension forming the basin (Crouch and Suppe, 1993; Ingersoll and Rumelhart, 1999).

For comparison, we also show the RFs calculated for the DLA station of the SCSN, which is located in the basin and is close to the A-A' profile (Fig. 3.1). With two years of data, we have ~ 100 events for the RFs, and the results are shown in Fig. 3.10. We see that despite the large number of events with a good azimuthal coverage, the useful phases (for example, the Moho Ps) are still very difficult to recognize.

Time*	Latitude(°)	Longitude(°)	Depth(km)	Magnitude	Back-azimuth(°)	Distance(°)
20141009021431	-32.1082	-110.811	16.54	7	173.231	66.0076
20141014035134	12.5262	-88.1225	40	7.3	120.746	34.5917
20140924111615	-23.8009	-66.6321	224	6.2	132.236	75.4109
20141101185722	-19.6903	-177.759	434	7.1	236.282	77.8924

*Time is in the format of YYYYMMDDHHMMSS

Table 3.1: Events with clear recordings. The top two events happened while most stations were in operation, and are used in the receiver function analysis.

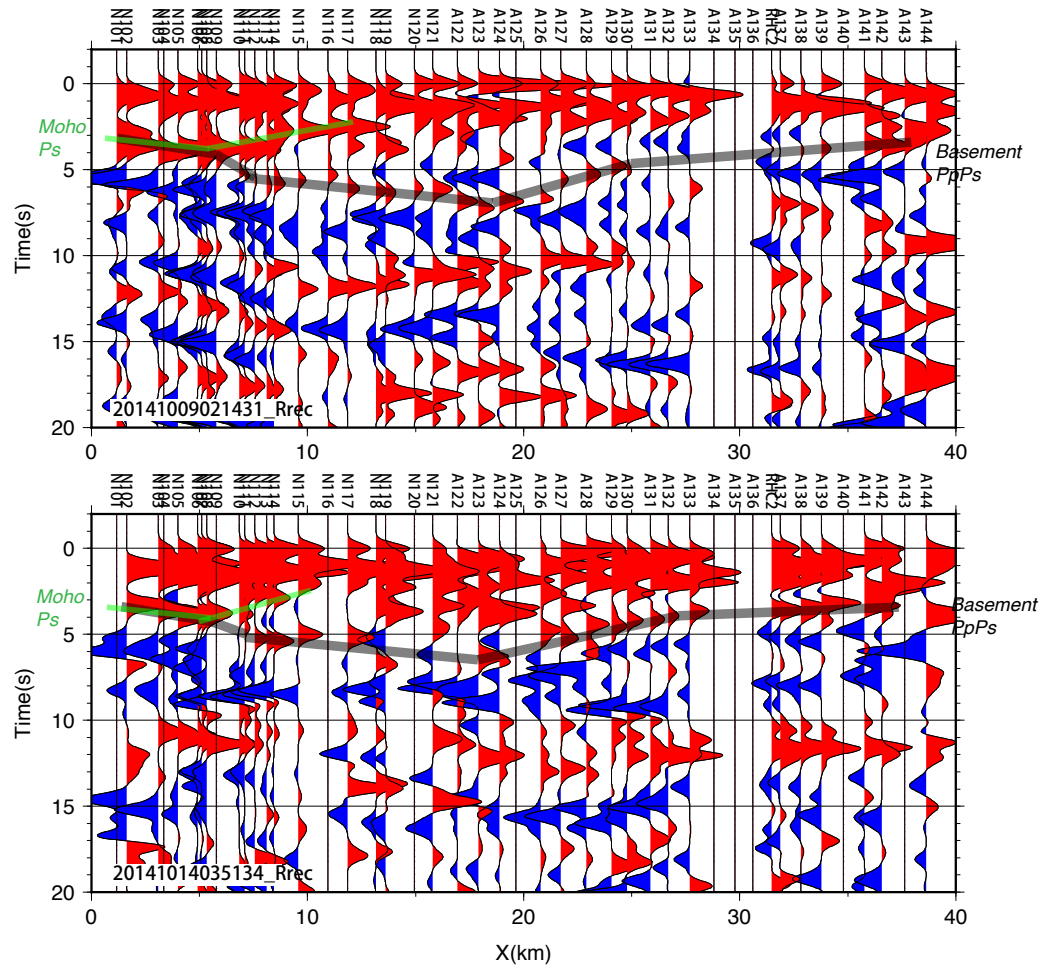


Figure 3.2: Receiver functions of two events recorded by all the yellow-dot stations in Fig. 3.1. The PpPs phase related to the P-to-S conversion at the basement is recognized after the time-depth conversion shown in Fig. 3.9.

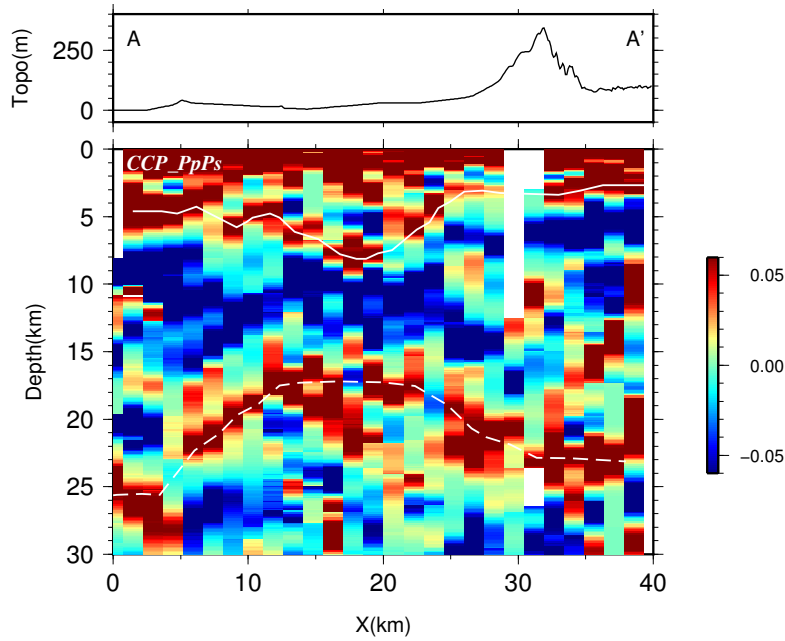


Figure 3.3: CCP migration with PpPs phase. The white lines delineate the inferred basement depth and Moho depth.

3.4 Ambient noise tomography

The multi-component cross-correlation results are shown in Ma et al. (2015). The Love wave is relatively simple for dispersion analysis (1-12 s here), while strong higher-mode Rayleigh wave exists in periods less than 5 s. Identifying the modes is important because using the wrong mode will lead to incorrect shear wave velocity estimates. Ma et al. (2015) proposed to use the particle motion direction to distinguish between the two modes. More work is needed to automate the phase extraction for this small-aperture array (thus less separated modes), and for the present, we limit the dispersion analysis to the fundamental Rayleigh wave with periods longer than 5 s.

The FTAN method (Lin et al., 2008; Bensen et al., 2007) is used to measure the dispersion curves, with T-T cross-correlations for Love wave, and Z-Z cross-correlations for Rayleigh wave. To resolve the 2π ambiguity, we track the dispersion curve from

long period to short period, and use the group velocity ($U = \partial w / \partial k$) to guide the instantaneous slope of the dispersion curve. The longest period used for each station pair is limited by one wavelength (Luo et al., 2015) to satisfy the far-field approximation. Therefore, to increase the ray coverage, the SCSN stations are used for periods longer than 5 s.

The dispersion curves are used to invert for the phase velocity maps at each period, with a method similar to Barmin et al. (2001). The tomographic inversion is formed as a linear inversion problem to minimize the cost function of: $(Gm - d)^T C^{-1} (Gm - d) + \lambda^2 \|Fm\|^2$, where the first term is the data misfit with $d = t - t_0$, $m = (c_0 - c)/c$, and the data covariance matrix C that is estimated from the misfit after a trial inversion (with a large damping parameter). The second term is the Gaussian smoothness with the correlation length set as twice the grid size. The damping parameter λ is chosen with reference to the L-curve (misfit vs. smoothness curve) (Aster et al., 2011). The resolution matrix $R = (G^T C^{-1} G + \lambda^2 F^T F)^{-1} G^T C^{-1} G$ is used to do the resolution test, with the input checkerboard model m and output model $\hat{m} = Rm$.

The dispersion curve at each location along A-A' profile is then extracted from the phase velocity maps, and inverted for the local 1-D structures which are then combined to form a 2-D profile. A linear inversion method ($c^2 = G\beta^2$) based on approximate eigenfunctions (Haney and Tsai, 2015) is used. The result is subsequently used as an initial model for a more accurate nonlinear inversion (Herrmann and Ammon, 2002).

3.4.1 Phase velocity maps

For Love waves, we measure the dispersion curves from 1-12 s for the cross-correlations between the LASSIE stations (“partial data”), and 5-12 s for the cross-correlations between all stations including both LASSIE and SCSN stations (“full data”). The dispersion curves are then used to form the phase velocity maps at each period (1-12 s) through tomographic inversion. For the 1-5 s “partial data”, the inversion is performed in a rectangular region enclosing the LASSIE stations, with a grid size of

2 km. For 5-10 s “full data”, the inversion is performed in a large region enclosing all the stations, with a grid size of 5 km. Examples of phase velocity maps and resolution tests are shown in Fig. 3.11. For the Rayleigh waves, the procedure is similar to the Love wave analysis, with examples shown in Fig. 3.12.

A 2-D profile (distance vs. period) along A-A’ is extracted from the Love (1-12 s) and Rayleigh (5-10 s) wave phase velocity maps, and is shown in Fig. 3.4.

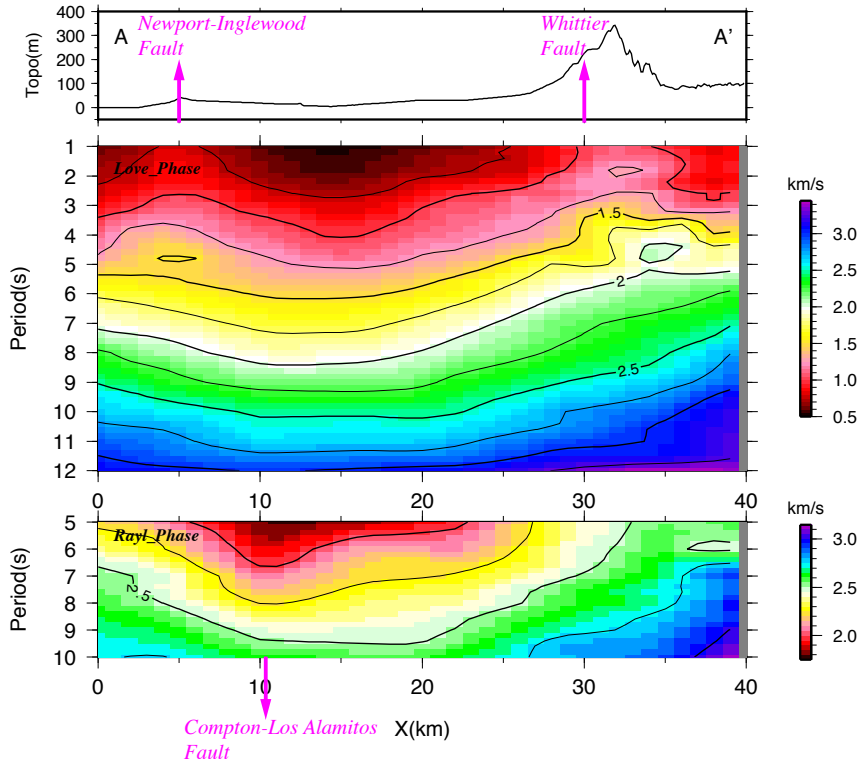


Figure 3.4: Tomographic inversion result along A-A’ profile. The y-axis is the period. The results above 5-s period are extracted from Figs. 3.11 and 3.12, in which we use both LASSIE and SCSN stations. For Love wave below 5 s, we only use LASSIE stations. The inversion is similar to the one shown in Fig. 3.11, but in a small rectangular region that encloses LASSIE stations only.

3.4.2 Shear velocity structure

For every 1 km in the profile in Fig. 3.4, we extract both the Love and Rayleigh dispersion curves, and invert for the local 1-D structure, which will be combined to form

a 2-D velocity profile along A-A'. Note that the Love wave gives V_{SH} structure, while the Rayleigh wave gives V_{SV} structure, which can be different because of anisotropy.

The inversion from phase velocities to shear velocities is a nonlinear problem (Aki and Richards, 2002). Haney and Tsai (2015) derived a linear form for the inversion ($c^2 = G\beta^2$), with approximate eigenfunctions calculated from a power-law structure. It has advantages in that no initial model is needed and the resolution and other properties (such as parameterization of the layers, choice of damping parameters) are easier to analyze. Other assumptions include constant density and a Poisson's ratio of 0.25, which should only cause small errors in the result because the phase velocities are most sensitive to V_S . Here, we use their formulas to invert the Love and Rayleigh wave dispersion curves, and the result is used as an initial model for the more accurate nonlinear inversion. The cost function to minimize is $\|c_{L/R}^2 - G_{L/R}\beta^2\|^2 + \lambda^2\|L\beta^2\|^2$, where the first term is the data misfit (Love or Rayleigh), and the second term is the regularization on the first derivative of the model (β^2).

For the Love wave (1~12 s) inversion, the model is parameterized into layers with increasing layer-thickness $h_n = k^{n-1}h_0$ ($n = 1\dots N$) down to a depth of 10 km, below which it is treated as half space. We choose $h_0 = 0.1$ km, and $k = 1.11$. The damping parameter λ^2 is chosen as 0.1. The resolution matrix (an example is shown in Fig. 3.13a) shows that the resolution is diminishing beneath 3 km depth. The result from the linear inversion is shown in Fig. 3.5. Based on this, we calculate the V_P and density with the empirical relationship from Brocher (2005) (equation (1) and (9)). They are used as an initial model in the nonlinear inversion code by Herrmann and Ammon (2002), and the result is also shown in Fig. 3.5, which is only slightly different from the linear inversion. We see clear evidence of the Newport-Inglewood fault (NIF) and Whittier fault (WF) in the results.

For the Rayleigh wave (5~10 s), an initial attempt to invert with it alone suggests that the data has a very limited constraint on the model (see the resolution matrix in Fig. 3.13b), mainly due to the lack of constraints on the top 5 km. Therefore, we jointly invert for both Rayleigh and Love wave data (see the resolution matrix in Fig. 3.13c) with the assumption that the anisotropy is not strong, which can be

checked with the misfit afterwards. The procedure is similar to previous inversions with Love wave, except that basement depth (from RFs) is taken into consideration for the deeper-depth sensitivities of the Rayleigh wave, and the layer thickness beneath the basement depth is much thicker (with $k = 2.5$). Less damping ($1/3$) is imposed across the interface corresponding to the basement depth. The linear and nonlinear inversion results are shown in Fig. 3.6. The fit of the data is shown in Fig. 3.14.

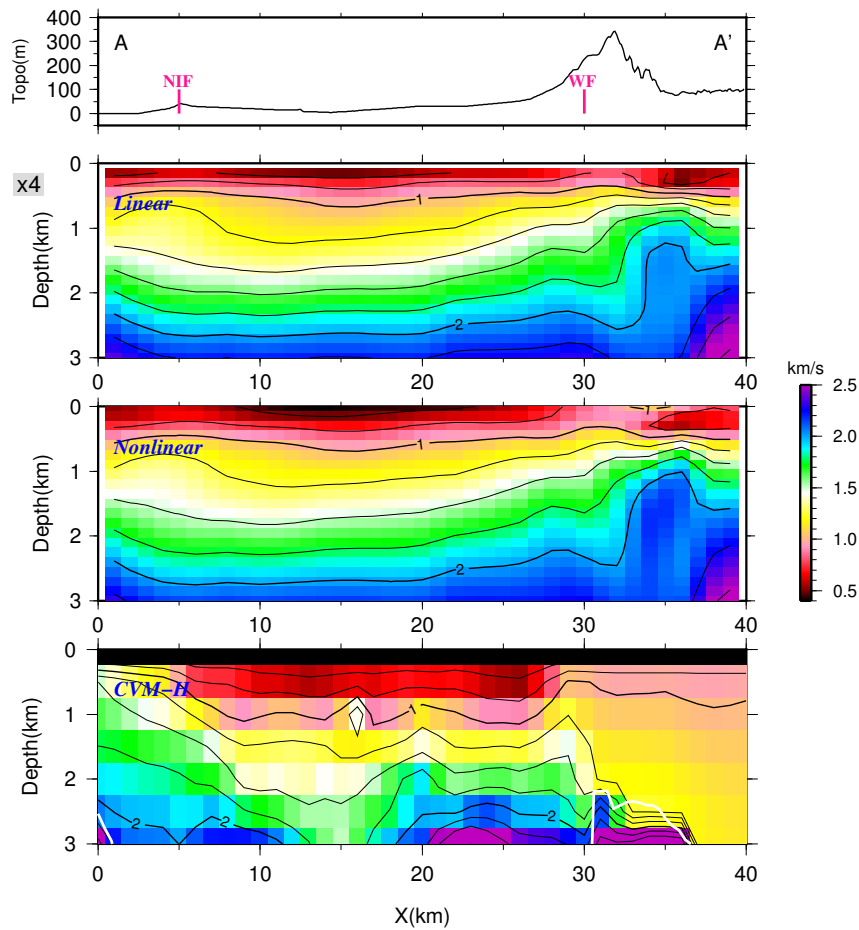


Figure 3.5: V_{SH} inversion results using 1-12 s Love wave dispersion data. From top to bottom: linear inversion, nonlinear inversion, and CVM-H model.

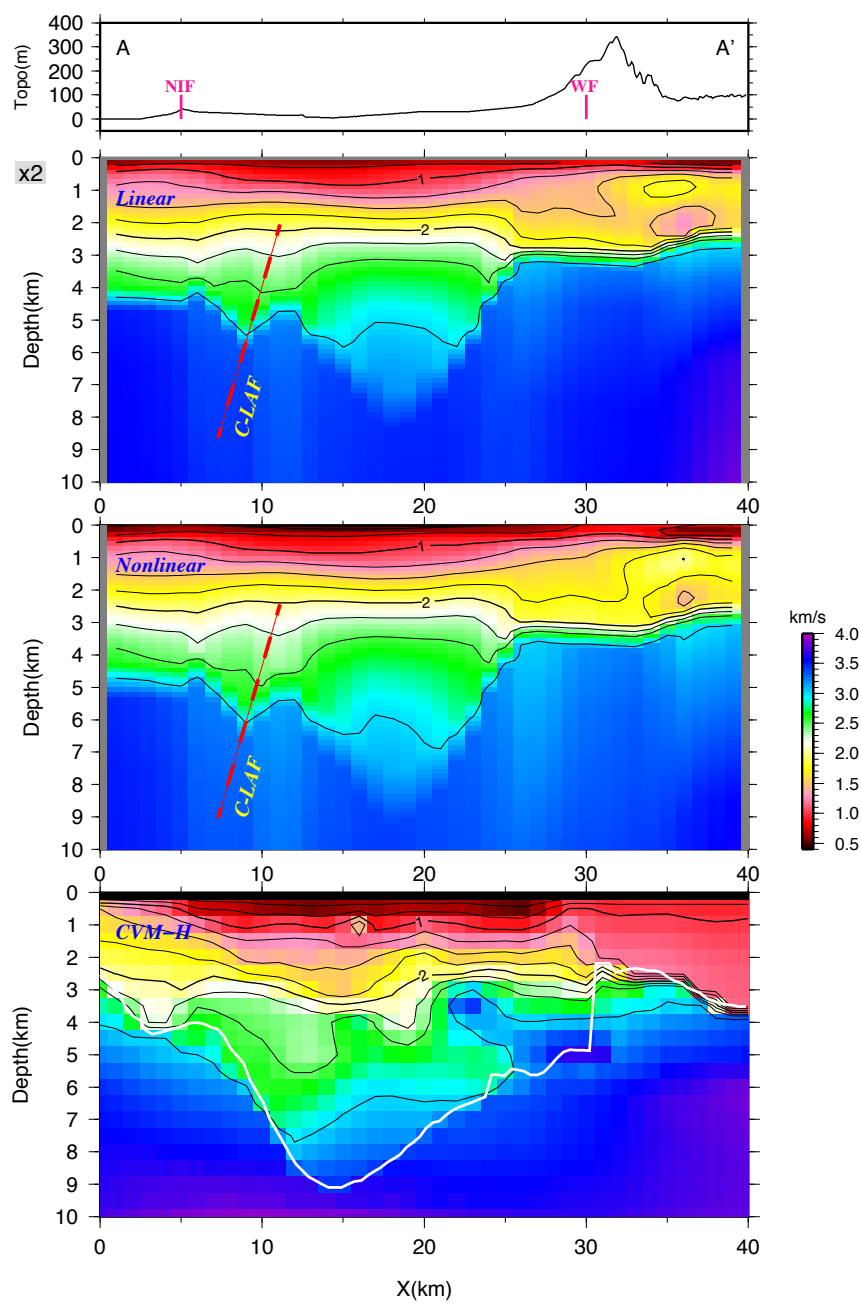


Figure 3.6: V_S inversion results using 1-12 s Love wave and 5-10 s Rayleigh wave dispersion data. From top to bottom: linear inversion, nonlinear inversion, and CVM-H model. The approximate location of the “C-LAF” (Compton-Los Alamitos Fault) from Wright (1991) (Fig. 3.16) is delineated with red dashed line.

3.5 Discussion

3.5.1 The basement and Moho depths

The basement and Moho depths have been clearly delineated with the PpPs phase of the receiver functions. The basement depth is not only essential to the understanding of the formation of the basin, but also to the evaluation of the seismic hazard, since it determines the resonance frequency of the basin. Previous estimates of the basin bottom were determined by gravity, constrained by a few borehole measurements (Yerkes et al., 1965; McCulloh, 1960), while industry reflection data does not penetrate to the bottom of the deepest part of the basin. Here, we have provided a direct image of the basement depth with the receiver functions.

The Moho depth beneath the Los Angeles basin has not been well resolved. The CVM-H model (Fig. 3.8) is a simple linear interpolation between the Moho depth at the offshore and the northern edge of the basin. There has been some indication of an upwarp of the Moho beneath the basin based on the traveltime residuals of the teleseismic events (Kohler and Davis, 1997); however, the accuracy is limited by limited knowledge of the crustal velocities. The receiver functions directly show the elevated Moho shape beneath the basin, and reveal a 10 km thick crust under the center of the basin (note that, the crust is referred to the crystalline part, excluding the sedimentary layer) .

From the following analysis, we see that the basin is in isostatic equilibrium. Denote the density of the sediment, crust, and mantle as ρ_s , ρ_c , and ρ_m ; the initial thickness of the crust before stretching as h_c ; the thickness of the sediments as h_s ; and the elevation of the Moho beneath the basin (filled by mantle) as h_m . From the principle of isostasy, we have $\rho_c h_c = \rho_s h_s + \rho_c (h_c - h_s - h_m) + \rho_m h_m$. This gives $\frac{h_s}{h_m} = \frac{\Delta h_s}{\Delta h_m} = \frac{\rho_m - \rho_c}{\rho_c - \rho_s}$, which is 5/3 for $\rho_s = 2500 \text{ kg m}^{-3}$, $\rho_c = 2800 \text{ kg m}^{-3}$, and $\rho_m = 3300 \text{ kg m}^{-3}$.

Without information about the initial thickness of the crust, what we observed in the RFs is h_s and, $\frac{\Delta h_s}{\Delta h_m}$ which is about 1. It is within the reasonable range of the prediction by isostasy (for example, $\rho_m = 3100 \text{ kg m}^{-3}$ satisfies isostasy). Using

$\frac{\Delta h_s}{\Delta h_m}=1$ and the observed h_s , we estimate that the initial crustal thickness is about 26 km, which is the average of the CVM-H model here (Fig. 3.8). The stretch factor β , which is the ratio between the original and the thinned crustal thickness, is thus 2.6 for the center of the basin, and decreases to about 1.3 at the edge. This factor determines the thermal subsidence of the basin in the uniform stretching model of McKenzie (1978).

3.5.2 Comparison with the uniform stretching model

McKenzie (1978) has proposed a classic model for the stretching and subsidence of a basin. In their model, the total subsidence consists of initial subsidence and thermal subsidence. The rapid stretching of the crust and sub-crust lithosphere causes the initial subsidence, which is accompanied by the upwelling of the asthenosphere. The subsequent cooling of the lithosphere and asthenosphere causes the thermal subsidence. There have been many successful applications of this model (“uniform stretching model”); however, for the LA Basin, it was modified to include a 2-D heat flow as presented in Sawyer et al. (1987). Turcotte and McAdoo (1979) have also successfully explained the southwestern block of the LA Basin with the half-space cooling model, and in addition, linked the thermal history with the oil production. Their model essentially considers the thermal subsidence only and needs corrections for applications elsewhere, for example, to the central block of the LA Basin as discussed in their paper.

In section 3.5.1, we estimate the stretch factor β (2.6 in the center, 1.3 in the edge) and initial crustal thickness (26 km). Using formulas and parameters in McKenzie (1978) with an assumption of a sediment-loaded basin, the subsidence is shown in solid lines in Fig. 3.7. The RF basement depths in the center and edge of the basin are taken as the observed subsidence. Supposing the thermal subsidence started at about 11 Ma (Turcotte and McAdoo, 1979; Sawyer et al., 1987), we see that the deficiency of the prediction is ~ 3 km in the center and 1 km in the edge. In Fig. 3.15, we take $\beta = 2.6$ as an example, and show the change in the predicted subsidence with a 10%

change in each parameter. We see that the most plausible change in the parameter in order to fit the data is the density of the crust (dashed line in Fig. 3.7, with $\rho_c = 2.67 \text{ g cm}^{-3}$). However, this only changes the initial subsidence, and the thermal subsidence remains the same, which is against the observation from the strata data as in Sawyer et al. (1987). They suggested a 2-D thermal conduction to explain the rapid thermal subsidence rate. The stretch factor, however, is a variable that needs to be estimated in their paper, and our results can be used to better constrain the model.

The models above can be oversimplified considering the recent transpression on the basin (e.g., Ingersoll and Rumelhart (1999)). And because of the compression, the present crustal thickness we observed can be thicker than that after the stretching. We would need to include more data (e.g., the stratigraphic records) to better infer the subsidence history of the LA Basin.

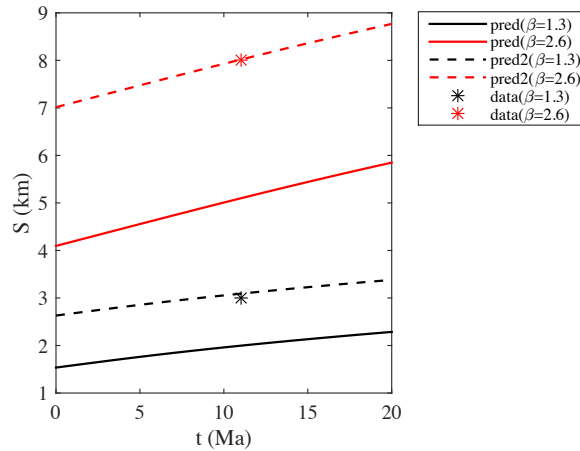


Figure 3.7: The predicted total subsidence from 1-D uniform stretching model. The solid lines are predictions with parameters in McKenzie (1978), and the dashed lines are that with a 5% decrease in the crustal density. The data (asterisks) are fit by the dashed lines, due to the increase in the initial subsidence, instead of the thermal subsidence, which is against the strata data.

3.5.3 The shear velocities

Because of the density of data from the oil industry, the CVM-H model of the basin shows a lot of detail in the P-wave velocity, and the S-wave velocity is largely inferred from it. In contrast, our results provide direct measurements on the shear velocities. The 1-12 s ambient-noise Love wave (Fig. 3.5) well constrains the V_{SH} in the top 3 km of the basin. The 5-10 s Rayleigh wave is less satisfactory in constraining the structure, and needs to be jointly inverted with the Love wave. It may be improved in the future with a better separation of the fundamental and higher modes in the 1-5 s period range.

In Fig. 3.5, we see that V_{SH} is less than 1 km/s for the top 0.5 km depth, and is less than 2 km/s for the top 2.5 km depth except for the region to the north of the Whittier fault, where the Puente Hills are located. North of the Puente Hills, the sedimentation increases as the line enters the San Gabriel Valley. The Whittier fault, as a thrust fault dipping to the north, is evidenced by the velocity contours. The velocity contours are also elevated at the location of the Newport-Inglewood fault, but a strong velocity contrast is not observed in this depth range (above 3 km depth). The observations are in accordance with the geological profile in Wright (1991), shown in Fig. 3.16.

In Fig. 3.6, we show the joint inversion from Love and Rayleigh waves, with the assumption that no strong anisotropy (V_{SV} vs. V_{SH}) exists. The shallow depth is controlled by Love wave data, and therefore is only slightly modified from Fig. 3.5. We see that the velocity gradient has rapidly decreased beneath the 2.5 km/s contour at ~ 4 km depth. It suggests that the compaction of the sediments has reached the maximum extent at this depth. We also note the small depression of the basement at 10 km distance coincides with the location of the buried Compton-Los Alamitos fault in Wright (1991) (“C-LAF” in Fig. 3.16).

3.6 Conclusions

We used data from a dense but short duration (~ 1.5 month) array that was deployed across the LA Basin to image the structure of the basin. With two seismic events, the basement and Moho depths are clearly delineated by the PpPs phase in the receiver functions. The shear velocities are revealed by the Love and Rayleigh waves that emerge in the multi-component cross-correlations.

An elevated Moho is imaged beneath the basin. From the edge to the center of the basin, the basement depth increases from about 3-4 km to about 8 km, and the crustal thickness decreases from 20 km to merely 10 km. It indicates a stretch factor increasing from 1.3 to 2.6, with an estimated initial crustal thickness of 26 km from isostasy. The prediction from a simple 1-D uniform stretching model is not sufficient to explain the total subsidence.

The shear velocity of the sediments increases from about 0.5 km/s to 2 km/s at a ~ 2.5 km depth. The gradient rapidly decreases at ~ 4 km depth, indicating that the sediments are fully compacted by this depth. The Newport-Inglewood fault, Compton-Los Alamitos fault, and Whittier thrust fault are both evident from the shear velocity profile.

3.7 Supplementary material

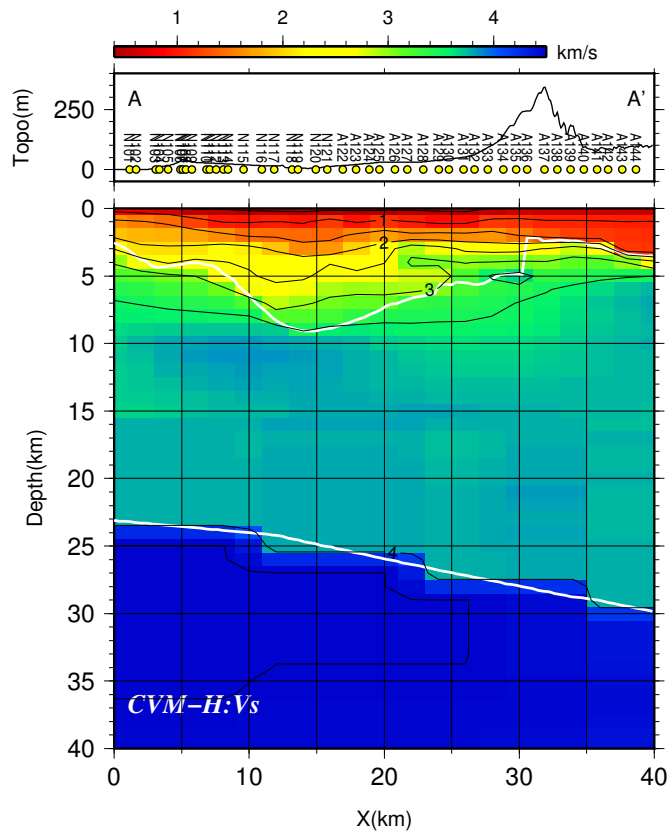


Figure 3.8: CVM-H model along profile A-A'.

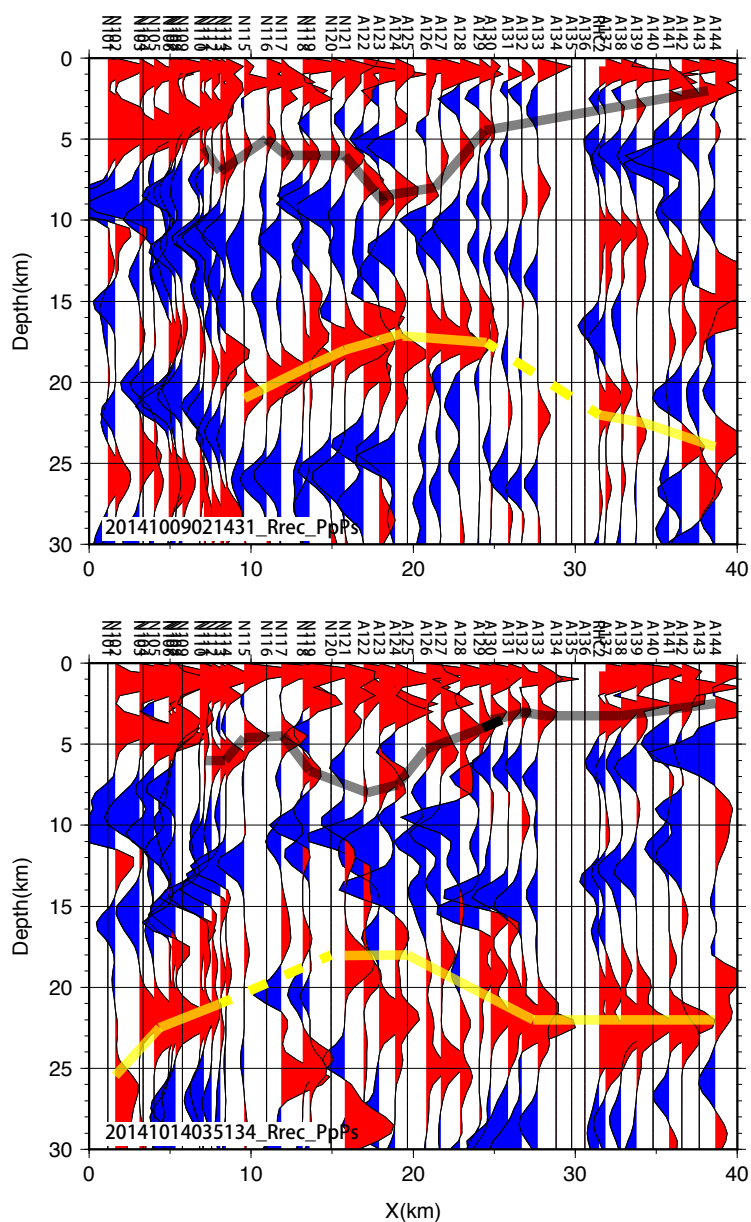


Figure 3.9: The depth-axis RFs with time-depth conversion for PpPs phase. The ~ 5 km offset in the structures in the two profiles is due to the different piercing points of the two events (Fig. 3.1), which is corrected in the CCP profile (Fig. 3.3). The black and yellow lines delineate the basement and the Moho respectively.

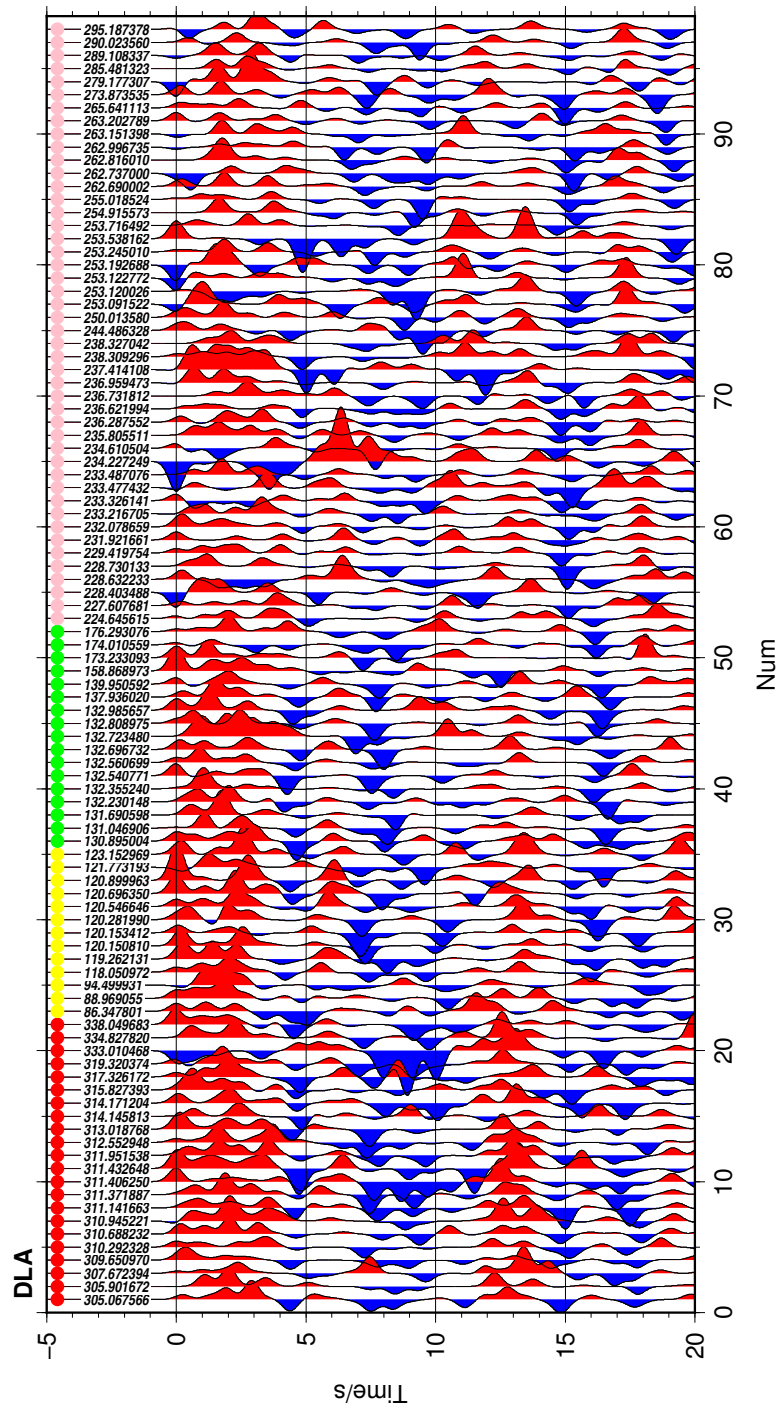


Figure 3.10: The time-axis RFs for DLA station. The events are arranged according to the back-azimuths, and are divided by four quadrants. The colored bar along the x-axis divides the quadrants.

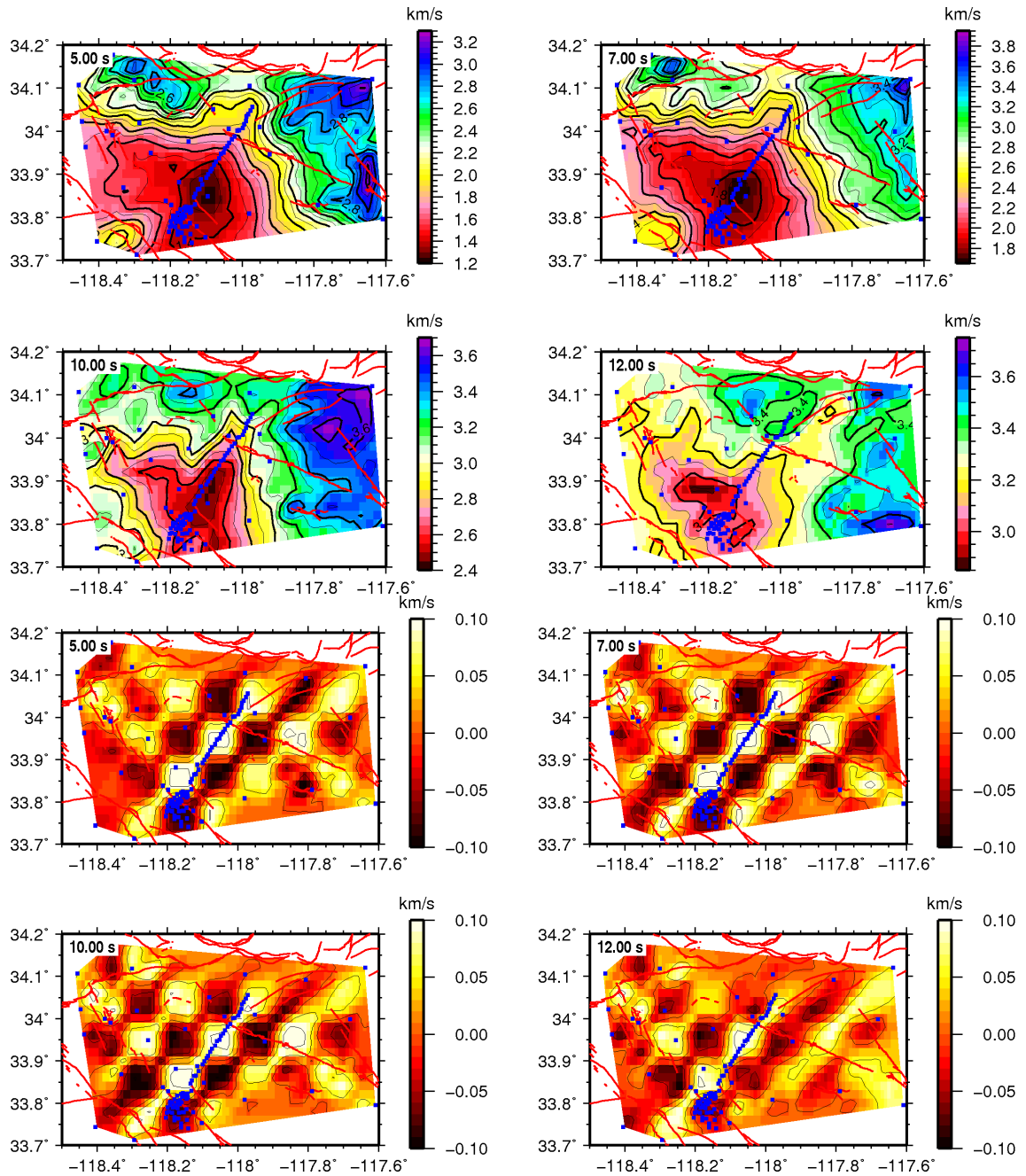


Figure 3.11: Love wave phase velocity map and resolution test for 5 to 12-s period.

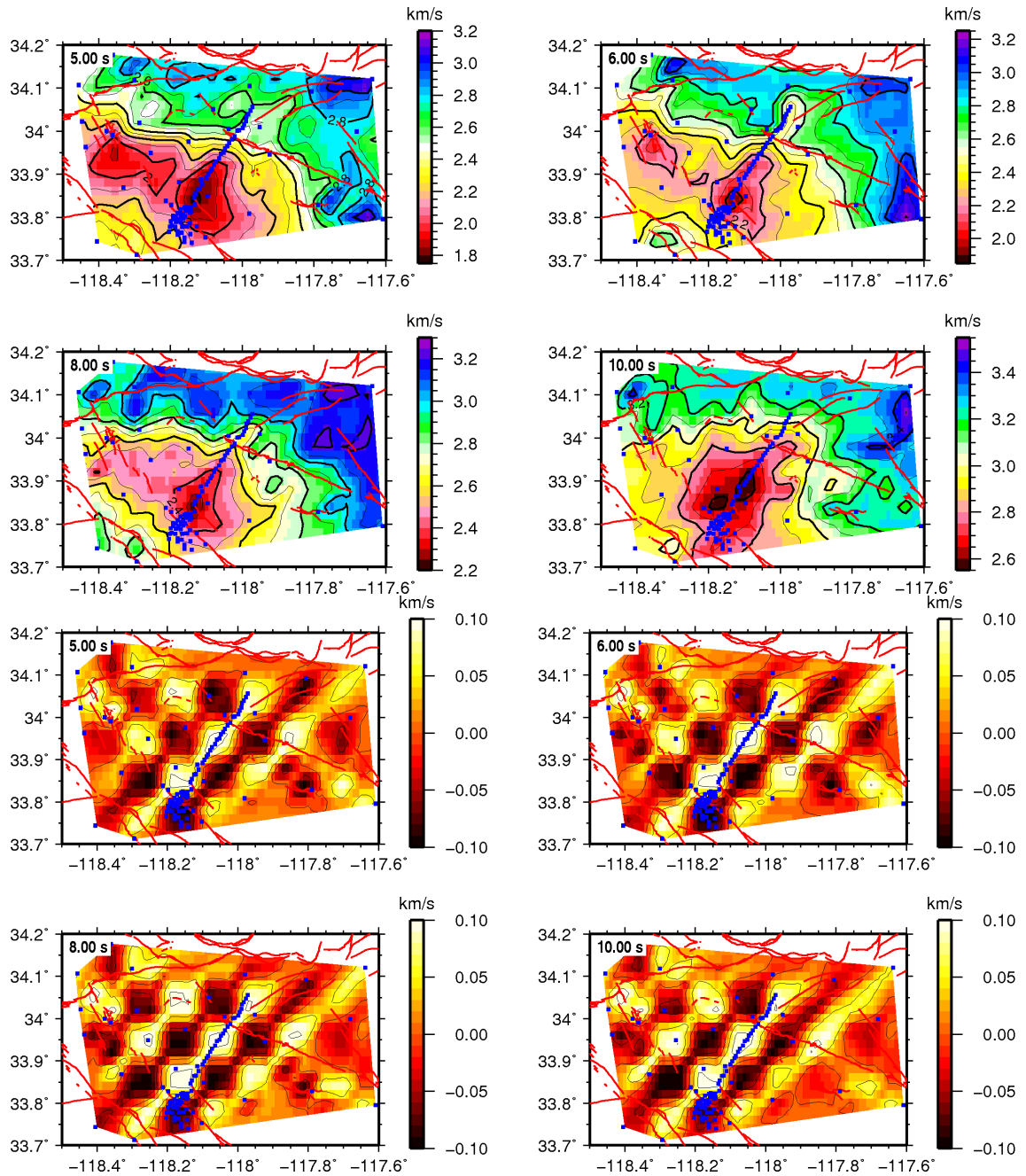
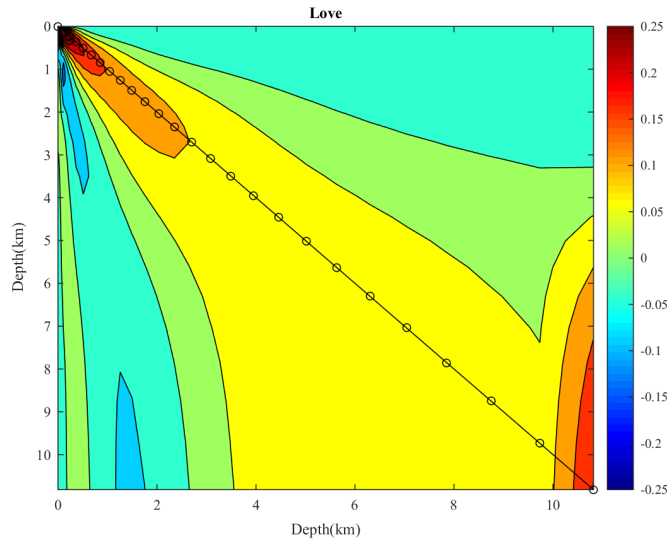
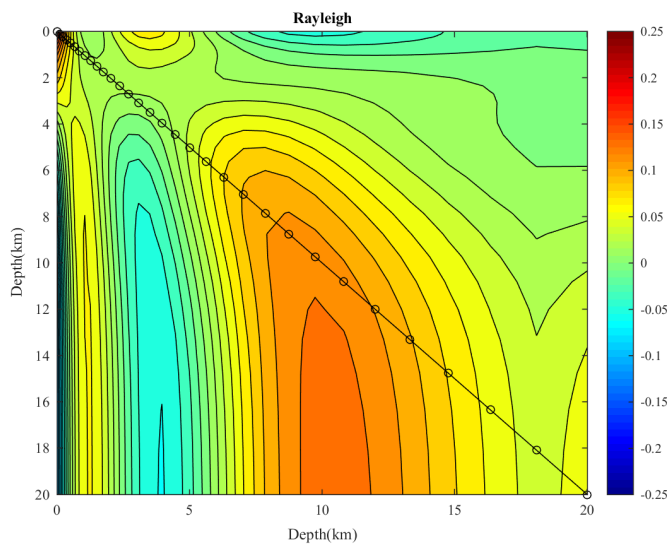


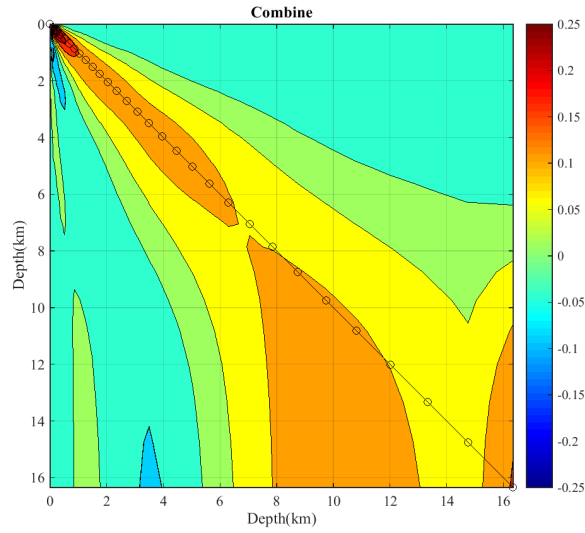
Figure 3.12: Rayleigh wave phase velocity map and resolution test for 5 to 10-s period.



(a)



(b)



(c)

Figure 3.13: The resolution matrix for the 1-D inversion at $x \approx 0$ km. (a) shows that the Love wave inversion has a good resolution until 3 km depth. (b) shows that with the Rayleigh wave data alone, one cannot constrain the structure. (c) shows that with both types of data, the resolution can reach about 8 km depth.

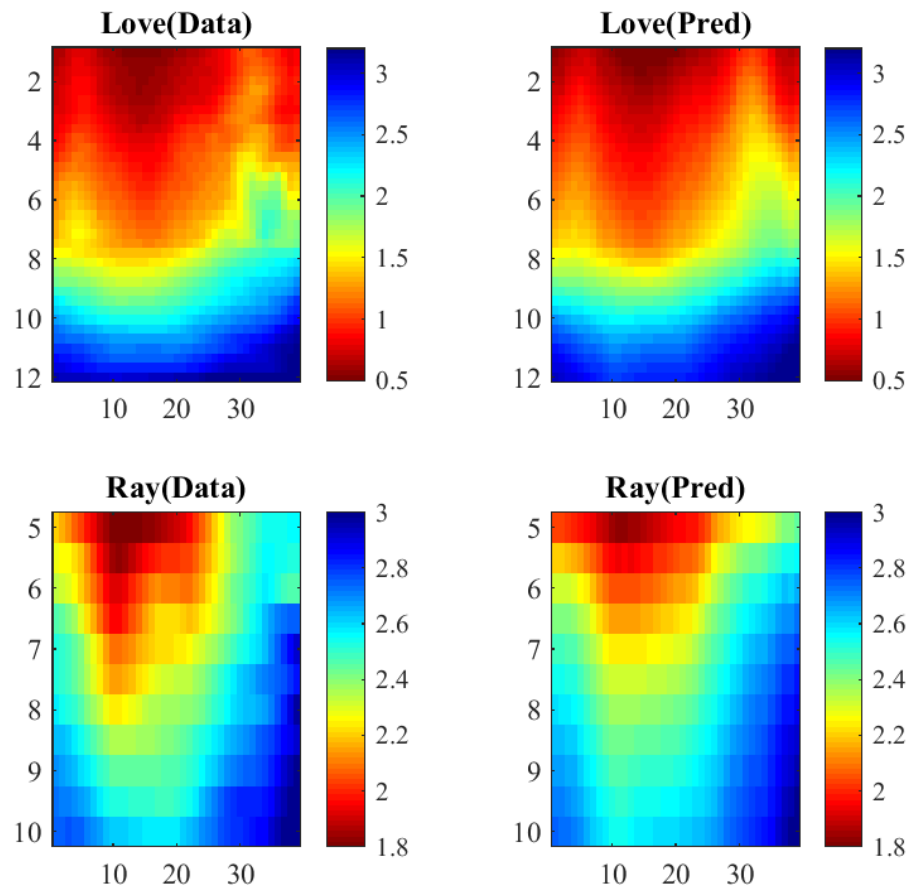


Figure 3.14: Data and predictions from the model (Fig. 3.6, second panel) inverted from the dispersion curves.

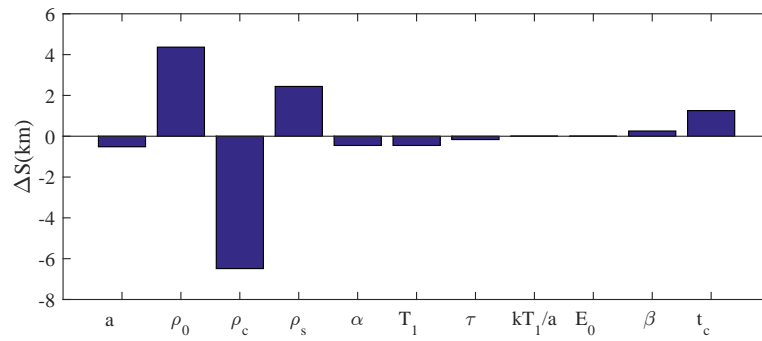


Figure 3.15: The change in the prediction of total subsidence with 10% perturbation in each parameter.

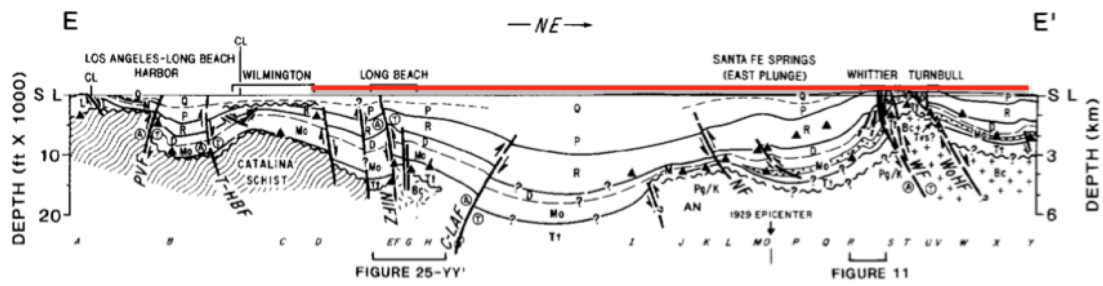


Figure 3.16: A geological profile adapted from Wright (1991). The red line shows the approximate range of A-A'.

Part II

PeruSE: Peru Subduction Experiment

Chapter 4

Locating a scatterer in the active volcanic area of Southern Peru from ambient noise cross-correlations

¹

¹Reprinted from Oxford University Press. Formal publication located at doi: 10.1093/gji/ggs103

Locating a scatterer in the active volcanic area of Southern Peru from ambient noise cross-correlation

Yiran Ma, Robert W. Clayton, Victor C. Tsai and Zhongwen Zhan

Seismological Laboratory, California Institute of Technology, CA 91125, USA. E-mail: yrma@caltech.edu

Accepted 2012 December 5. Received 2012 November 3; in original form 2012 July 17

SUMMARY

We report on a strong scatterer of seismic energy in the 5–10 s period range located in the volcanic arc of Southern Peru. It is superficially like an active noise source in that it produces a continuous signal that arrives earlier than the inter-station surface wave in the noise cross-correlations. However, it is clearly determined to be a scatterer based on the coda arrivals observed in the cross-correlations, and the fact that it scatters waves from earthquake sources. We model the scatterer as a cylinder approximately 5 km in diameter with a shear wave velocity 30 per cent lower than the background velocity. It is likely to exist at the depth of 5–10 km, and is located at 71.6°W/16.1°S with an error of 10 km, which is near the inactive volcano Nevado Chachani and the active volcano El Misti which recently erupted in 1985.

Key words: Interferometry; Wave scattering and diffraction; Volcanic arc processes.

1 INTRODUCTION

Ambient noise cross-correlations have been used extensively in the past decade to estimate the Green's function between pairs of stations (Lobkis & Weaver 2001; Shapiro & Campillo 2004; Wapenaar 2004). The surface wave portion of the Green's function has been used to determine earth structure (Shapiro *et al.* 2005; Yao *et al.* 2006; Brenguier *et al.* 2007; Lin *et al.* 2008) and, by looking at time-lapse changes, the noise cross-correlations have been used to forecast volcanic eruptions (Brenguier *et al.* 2008). The primary noise sources are primary microseisms (Hasselmann 1963) in the 10–20 s period band and secondary microseisms (Longuet-Higgins 1950) in 5–10 s period band, but unidentified sources such as the 26-s microseismic energy originating near Africa (Shapiro *et al.* 2006) have also been reported. When noise sources are non-uniformly distributed, Green's functions can still be approximately recovered (Yang & Ritzwoller 2008), but artificial or truncation phases can be created (e.g. Zhan *et al.* 2010).

Recently, Zeng & Ni (2010) and Zheng *et al.* (2011) reported on precursors which arrive earlier than the inter-station surface wave in ambient noise cross-correlations. They attribute the precursors to a localized noise source and locate it on Kyushu Island, Japan, by a similar procedure to the one described in this paper. Zeng & Ni (2011) suggest that those signals are created by random events associated with Aso volcano. In this case, Aso volcano is thought to be an active noise source because the strength of the precursors is out of phase with the seasonal changes of oceanic noise, and local measurements (Kawakatsu *et al.* 1994) show that Aso volcano produces significant energy in the frequency range of the precursors.

In this paper, we report on a situation that is superficially like that of the Zeng & Ni (2010, 2011) study. Strong precursory arrivals are

seen on noise cross-correlations in southern Peru, and the source of this energy is located in the volcanic arc associated with regional subduction (see Fig. 1). However, as we will show, the source in this case is not an active source, but a passive scatterer of oceanic microseism energy. This conclusion is confirmed by observing that the inferred scatterer also scatters waves from earthquakes. This type of feature may cause unidentified arrivals that appear on noise cross-correlations in other studies.

2 PRECURSOR AND CODA WAVES

Using the method of Bensen *et al.* (2007), we perform vertical-vertical ambient noise cross-correlations between all pairs of broadband stations along the lines shown in Fig. 1. A profile of cross-correlations from station PE13 to all stations on line PE (blue dots, approximately perpendicular to the coast) is shown in Fig. 2(a), and a profile of cross-correlations from station PF25 to all stations on line PF (green dots, approximately 300 km inland and parallel to the coast) is shown in Fig. 2(b). Each trace is filtered to 5–10 s period band and normalized by its maximum amplitude and, on average, 2 yr of recordings are used in each cross-correlation. The direct surface wave arrivals (red lines in Fig. 2) propagating inland are clear in Fig. 2(a), but it is apparent from both of these profiles that the cross-correlations contain significant energy in arrivals besides the direct surface wave. The precursory energy (arriving at correlation times closer to zero than the direct wave) in both profiles is especially clear, but we observe that significant energy also arrives later than the direct wave (e.g. at stations PE03–PE12). We devote the remainder of this paper to quantitatively explaining these observations.

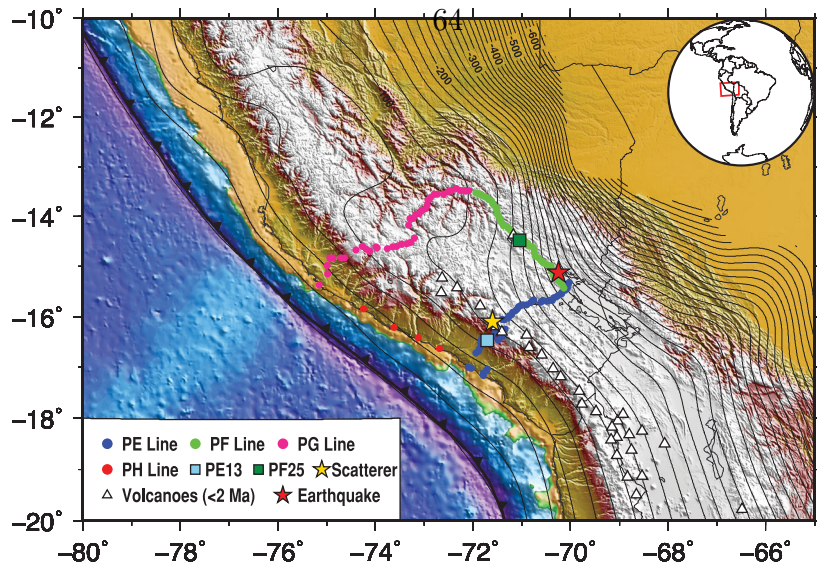


Figure 1. Locations of the seismic stations (dots) used in this study: lines PE (blue), PF (green), PG (pink) and PH (red). Stations PE13 (light blue square) and PF25 (dark green square) are the two virtual source stations used in Section 2. The yellow star is the location of the scatterer located in Section 3. The red star is the hypocenter of the earthquake used in Section 5. All the white triangles are volcanoes (<2 Ma).

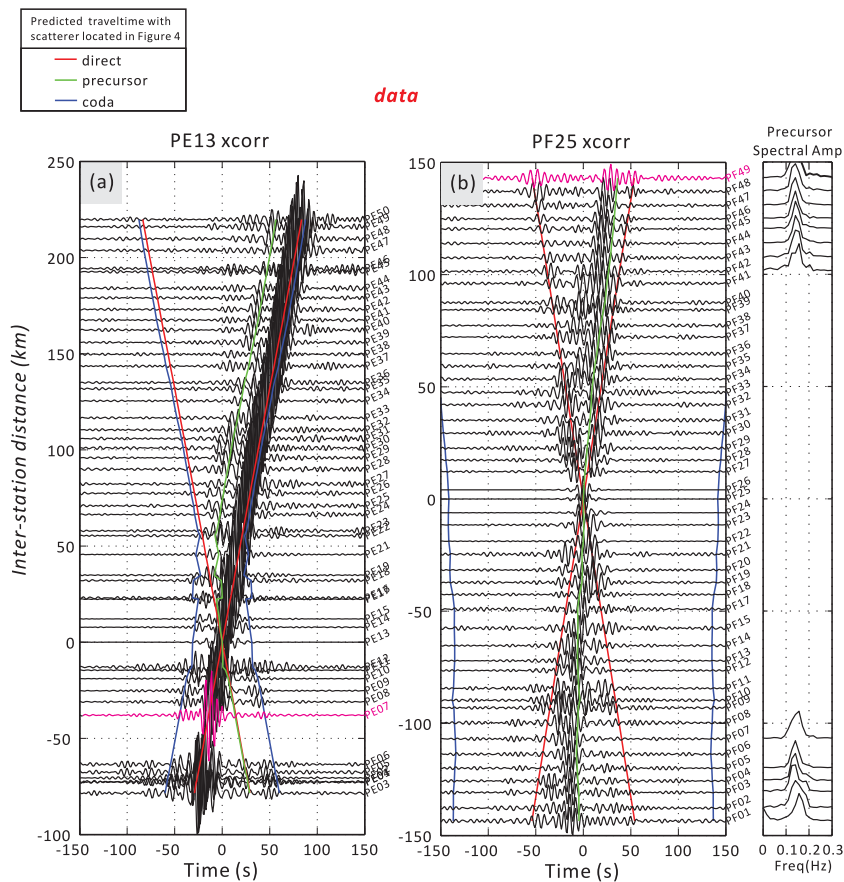


Figure 2. Two profiles of cross-correlations. The direct, coda and precursor arrival times plotted in red, blue and green lines are predicted from the location of the scatterer shown in Fig. 1 and located in Section 3. (a) Cross-correlations between PE13 (the light blue square in Fig. 1) and all PE stations (the blue dots in Fig. 1), aligned in a direction roughly perpendicular to the coast. Positive distances represent the cross-correlations between PE13 and stations further inland. The pink trace is the cross-correlation between PE13 and PE07, which is examined in Section 4. (b) Cross-correlations between PF25 (the dark green square in Fig. 1) and all PF stations (the green dots in Fig. 1), aligned in a direction roughly parallel to the coast. Positive distances represent the cross-correlations between PF25 and stations to the NW. The pink trace is the cross-correlation between PF25 and PF49, which is examined in Section 4. Also shown are some examples of the spectral amplitude of the precursor. The spectral amplitudes of the precursory waves are peaked at about 0.15 Hz.

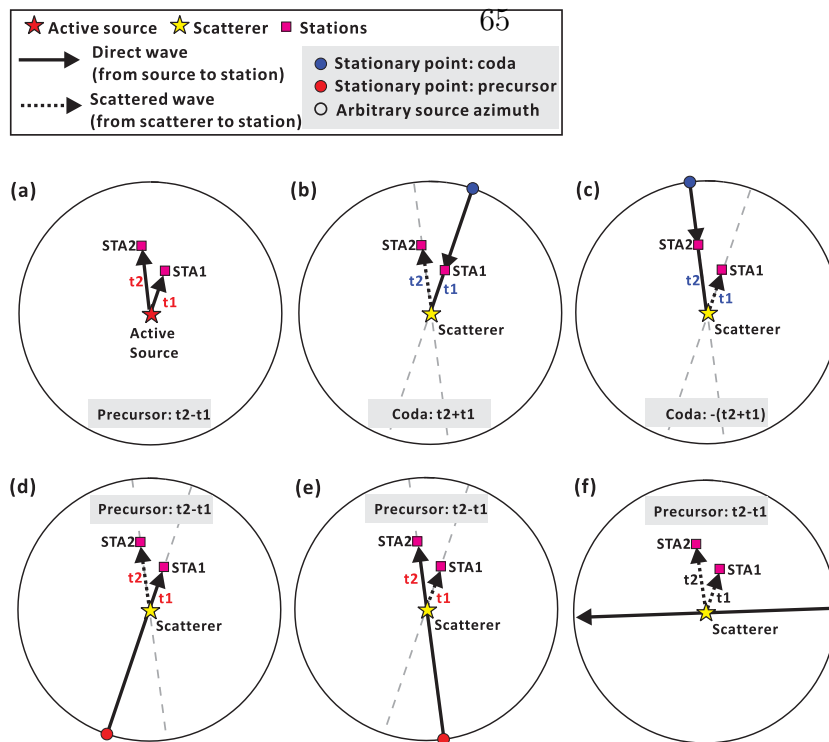


Figure 3. Schematic diagram shows the generation of the precursor and coda in the cross-correlation. (a) In the case of an active source, the precursor is generated from the cross-correlation between two waves travelling from the source to the two stations. (b)–(f) In the case of a scatterer, both coda and precursor are generated. In (b)–(e), the precursor and coda are generated from the ‘direct-scattered’ wave correlations. Among the noise sources from all azimuths, the contributions are mainly from four stationary points denoted with coloured dots. In (f), the precursor is generated from the cross-correlation between two scattered waves, and no stationary point exists.

We first focus on understanding the precursors. There are two clear candidates for explaining the precursory energy. Either the precursors are due to the presence of an active source of microseismic waves or they are due to the presence of a passive scatterer. In either case, if the travel times of the surface wave from the source/scatterer location to a pair of stations STA1 and STA2 are t_1 and t_2 , then the cross-correlation between STA1 and STA2 produces an additional signal that arrives at $t_2 - t_1$. This arrival will always be precursory to the direct arrival between the stations except when the stations and source/scatterer are co-linear. For the active source, this is straightforward to understand and a simple schematic is shown in Fig. 3(a).

For the scatterer, we can understand all of the arrivals based on the stationary phase analysis of Snieder *et al.* (2008), who derived the travel times and stationary points for the expected arrivals in the cross-correlation of ambient noise in the presence of a point scatterer. Wapenaar *et al.* (2010) also derived similar relations using the reciprocity theorem. Their results show that the cross-correlation contains ‘direct-scattered’ wave correlations (Figs 3b–e). These ‘direct-scattered’ correlations represent the cross-correlation between the direct wave that propagates from the source to one station and the scattered wave from the source to the scatterer then to the other station. These contributions, which come from four stationary points, result in four arrivals. If t_1 and t_2 are the travel times of the surface wave from the scatterer to the two stations STA1 and STA2, then two of the four arrivals emerge as coda waves in the positive and negative lags with the arrival times $\pm(t_1 + t_2)$ (Figs 3b and c) and the other two are precursor waves and have the same arrival time $t_2 - t_1$ (Figs 3d and e). The precursor also coincides with the arrival time of the signal from the correlation between two scattered

waves that propagate to the two stations (Fig. 3f). If sources are uniformly distributed, the three components of the precursor wave cancel each other (Snieder *et al.* 2008), but when the noise source distribution is not uniform or the wave speeds vary spatially, the phase exists.

From the preceding discussion, we find that while both the active source and the scatterer generate precursors, coda waves are only generated by the scatterer. Since strong coda waves are observed in Fig. 2(a), we rule out the possibility that an active source is exclusively responsible for the observations. In the following sections, we determine the location (Section 3) and strength (Section 4) of the inferred scatterer, as well as provide a more detailed analysis of the features in Fig. 2 and offer additional evidence against an active source. In Section 5, we confirm that the inferred scatterer also scatters earthquake waves and therefore cannot be a microseismic source.

3 LOCATING THE SCATTERER

We use all the cross-correlations between PE stations and PF stations to locate the scatterer. If the scatterer is equidistant from a given pair of stations, the precursor will arrive at zero lag assuming uniform velocity. Searching for pairs of stations which have the precursor at zero lag allows us to quickly locate the scatterer to the active volcanic area. We then refine the location with a grid search using a $0.05^\circ \times 0.05^\circ$ grid. For each point, we predict the precursor and coda arrival times and stack the envelope amplitude of the cross-correlations (filtered to 5–10 s period band) at these times. The result is shown in Fig. 4. We use an average group velocity of

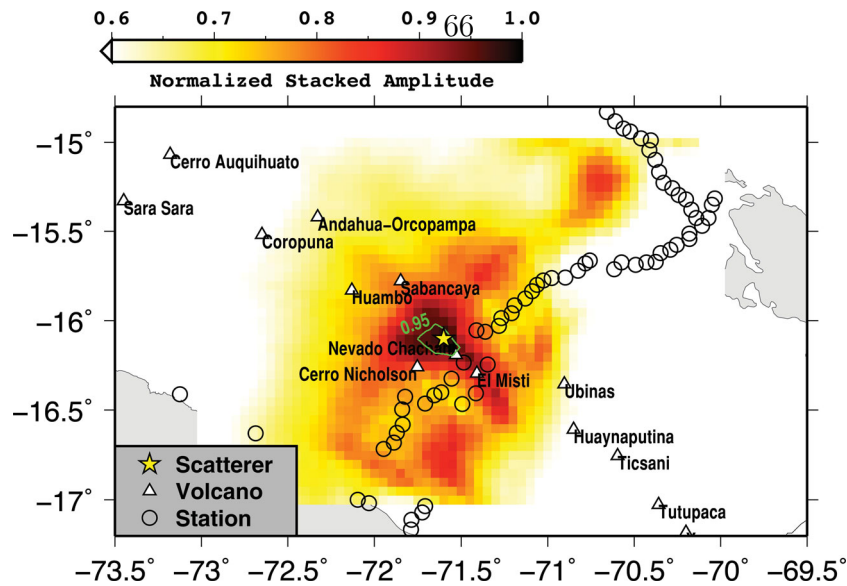


Figure 4. Locating the scatterer using a $0.05^\circ \times 0.05^\circ$ grid. For each point, we calculate the precursor and coda arrival times and stack the envelope amplitudes of the cross-correlations at these times. The colour is the normalized stacked amplitude for the entire data set, with arrival times calculated with a group velocity of 2.7 km s^{-1} . The 95 per cent confidence interval is denoted with a green contour, and is estimated through the bootstrap method. The scatterer's best-fit location is marked with a yellow star ($71.6^\circ\text{W}/16.1^\circ\text{S}$). It is closest to the inactive volcano Nevado Chachani, and is about 30 km from the active volcano El Misti which recently erupted in 1985. The locations of the volcanoes are from Global Volcanism Program (<http://www.volcano.si.edu/world/>).

2.7 km s^{-1} , obtained from 6-s direct surface wave group velocity measurements (as in Bensen *et al.* (2007)) between all stations of the array. The 6-s group velocity of the backarc region, where most of the cross-correlations used in the locating are, ranges from 2.6 to 2.9 km s^{-1} . A constant velocity for location purposes is justified because the velocity range is small and the paths average the velocity. Amplitudes are not used if they lie in the direct wave window defined as 10 s before the arrival time calculated with 3.0 km s^{-1} and 10 s after that calculated with 2.5 km s^{-1} . The maximum stacked amplitude and hence the best-fit location of the scatterer is at $71.6^\circ\text{W}/16.1^\circ\text{S}$ (yellow star in Figs 1 and 4). We note that we did not use the cross-correlations from lines PH and PG because we did not observe clear precursor and coda arrivals in the cross-correlations for these two lines. The reason for this is probably that line PG is far from the scatterer and line PH only has four stations, which makes it hard to observe the phases that are continuously observed in lines PE and PF (which each have 50 stations).

We estimate the 95 per cent confidence interval of the location using the bootstrap method. We vary the average velocity from 2.5 to 2.9 km s^{-1} in 0.1 km s^{-1} steps. For each velocity, we use 2000 data randomly picked from the entire 4600 cross-correlation data set to calculate the best-fit location, and repeat this 20 000 times. All the best-fit locations are combined to produce a contour map of the probability. In Fig. 4, the 95 per cent confidence interval is shown in green.

With the best-fit location of the scatterer, we then predict the travel times of the precursor and coda waves using the 2.7 km s^{-1} group velocity. These are plotted as coloured lines in Fig. 2, and they fit the group arrivals, which are the peak of the envelopes, to within 1.5 wavelengths. For example, the continuously observed precursor wave seen in Fig. 2(a) from PE19-PE50 is well fit by the green synthetic line. The coda waves observed from PE03-PE19 are also well fit by the blue synthetic lines. We note that the predicted arrival times do not just increase linearly with distance (as they would if plotted as a function of scatterer-station distance) because the distances plotted in Fig. 2 are inter-station distances. Some predicted

arrivals do not show up clearly in the data because of the non-uniform source distribution. For example, the cross-correlations in Fig. 2(a) are always one sided because of the dominant noise sources from the Pacific. Since the cross-correlations in Fig. 2(b) are roughly parallel to the coast, the direct waves are not well illuminated by oceanic noise sources, making the precursor wave the strongest arrivals in these cross-correlations. In the next section, these amplitude differences are modelled.

4 MODELLING THE PRECURSOR AND CODA WAVE AMPLITUDES

As discussed previously, because of the observed coda, scattering must contribute to the generation of the precursor. While an active source may also exist, the following two lines of evidence suggest that it should not be an important factor in producing the precursors. Firstly, the frequency content of the precursor is peaked in the secondary microseism band (peak at 0.15 Hz), as is shown in Fig. 2 for station pairs on line PF with especially clear precursor arrivals. This agreement suggests that the energy is related to oceanic sources. A scatterer of oceanic noise would naturally have this feature, whereas the coincidence of peak amplitude for an active source would need additional explanation. Secondly, as with the PE13 profile, we observe a sudden decrease in the precursor amplitude when STA2 changes from inland of PE19 (PE19-PE50) to the coastal side of PE19 (PE03-PE19). This cannot be explained by an active source unless the source has a strong directivity, but it is well predicted by the stationary points of the precursors that will be discussed in Section 4.3.

Based on the evidence presented above, we believe that the scatterer alone can explain our observations, and we proceed to model the precursor and coda amplitudes with a single scatterer. The amplitudes of the precursor and coda waves depend on the azimuthal distribution of noise source strength and the scatterer properties (e.g. velocity, size and depth). To fit the cross-correlation amplitudes, the first step is to determine the azimuthal variations in the

ambient noise source strength by using the direct wave amplitudes in the cross-correlations at different azimuths.

4.1 Noise source strength

The noise source strength at azimuth θ , written as $S(\theta)$, can be determined by the direct wave amplitude since $S(\theta)^2 \propto A\sqrt{R}$, where A is the direct wave amplitude and R is the inter-station distance (Stehly *et al.* 2006; Yang & Ritzwoller 2008; Yao *et al.* 2009). Here, we do not consider attenuation effects since the path lengths inside the array are short. We use 1-yr cross-correlations of all the stations with at least 300 days' recording in the year 2011. The cross-correlations are filtered to 5–10 s period band. We then calculate the signal-to-noise ratio (SNR) which is defined as the ratio of the peak of the envelope in the signal window (corresponding to a velocity between 2 and 3.5 km s⁻¹) to the root mean square (RMS)

of the noise window from 1000 s after the signal window to the end of the cross-correlation (3000 s lag). The SNR is multiplied by the square root of the inter-station distance to account for the geometrical spreading of the Rayleigh wave, and the (normalized) source strength is the square root of the result. To smooth the measurements, we average the source strength over every 10° in azimuth. The above method of using SNR to quantify the source strength works because the same normalization procedures are applied to both the signal and the noise window in the cross-correlation, and the trailing noise level is assumed to be similar for the array (Yang & Ritzwoller 2008; Lin *et al.* 2011).

We expect that the peak of the envelope samples the group arrival of the direct wave, and one problem is to avoid sampling the precursor if its amplitude exceeds that of the direct wave. To address this problem, we first visually inspect all the cross-correlations plotted with the predicted travel times of the precursor and direct waves.

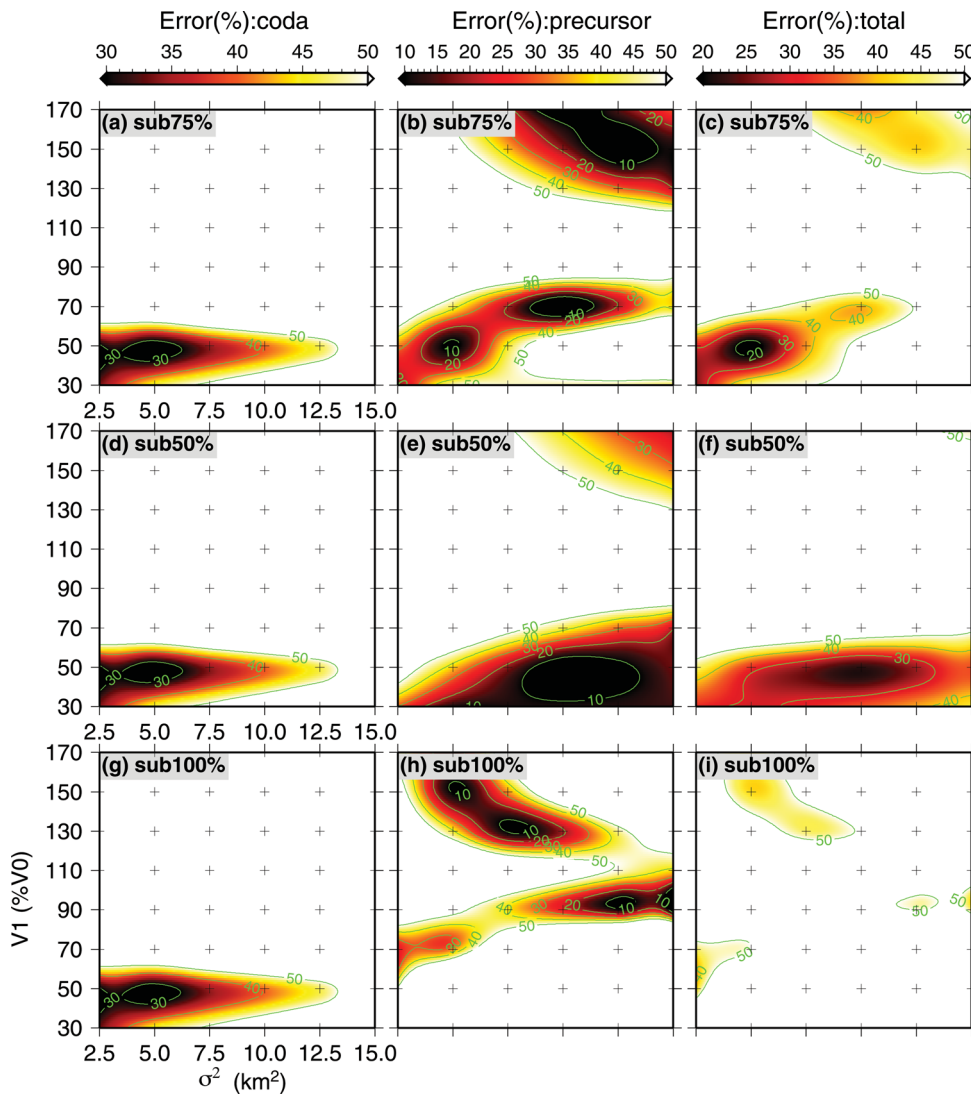


Figure 5. Modelling results for all combinations of parameters σ^2 and v_1 (see eq. 2 for definitions). (a) The error in fitting the coda amplitudes in the cross-correlation between PE13 and PE07 (pink trace in Fig. 2a). (b) The error fitting the precursor amplitude in the cross-correlation between PF25 and PF49 (pink trace in Fig. 2b). (c) The average of (a) and (b). The error is the relative error defined as $|A_{\text{syn}} - A_{\text{obs}}|/A_{\text{obs}}$. The three rows (sub 75 per cent, sub 50 per cent and sub 100 per cent) show the errors under three modified source conditions (see the text for details), which all give the same optimal parameters of $\sigma^2 = 5.0 \text{ km}^2$ and $v_1 = 50$ per cent v_0 from coda fitting. With the optimal scatterer properties, the precursor is best fit under the first (sub 75 per cent) source condition.

For those cross-correlations with a comparatively strong precursor, we calculate the precursor window using the same velocity range as that for the direct wave window. We also empirically determine the maximum SNR for the precursor as 40. If the calculated SNR is above this value, it is assumed to sample the direct wave even if the precursor window and the direct wave window overlap. If the calculated SNR is less than 40 and the windows overlap, the peak of the envelope is likely to sample the precursor and we determine the timing of the direct wave from the reciprocal lag since it is not contaminated by the precursor. We accept the timing of the direct wave determined in the reciprocal lag if the corresponding source strength is larger than 10, and use this timing to sample the envelope amplitude in the original lag and calculate the SNR.

We note that in the azimuthal source strengths estimated from the SNRs, the weak sources are heavily overestimated because they contain a significant component of background waves generated by scattering from throughout the volume, and the correlation of uncorrelated noise at each station site. To model the amplitude of the “weak” direct waves, we correct this bias by removing an estimate of the background wave strength to obtain a new estimate of source strength $S'(\theta)$. As will be discussed in Section 4.3, it is important to note that this correction only affects the modelled amplitudes of the direct waves and does not affect the estimation of scatterer properties.

4.2 Modelling the scatterer

To test the size and velocity contrast of the scatterer, we use a 2-D finite-difference code (Li *et al.* in preparation) to do membrane wave modelling. Tanimoto (1990) showed that for a narrow frequency band, and for smooth lateral variations of elastic constants (Lame parameter λ and shear modulus μ), Rayleigh and Love waves can be approximated by membrane waves which satisfy the 2-D wave equation:

$$\frac{\partial^2 u}{\partial t^2} - c(x, y)^2 \nabla^2 u = 0, \quad (1)$$

where u is the displacement and c is the local Rayleigh or Love wave phase velocity.

The model we use is a uniform phase velocity model of $v_0 = 3 \text{ km s}^{-1}$ with an embedded scatterer. The phase velocity is the average of that measured from the direct surface wave (method by Yao *et al.* (2006)) at 6 s in the cross-correlations between stations of this array. The scatterer is assumed to have a Gaussian distribution of velocity described by:

$$v = v_0 + (v_1 - v_0) \cdot \exp\left(-\frac{r^2}{2\sigma^2}\right), \quad (2)$$

where r is the distance from the centre of the scatterer, v_1 is the velocity at the centre and σ is one standard deviation of the Gaussian

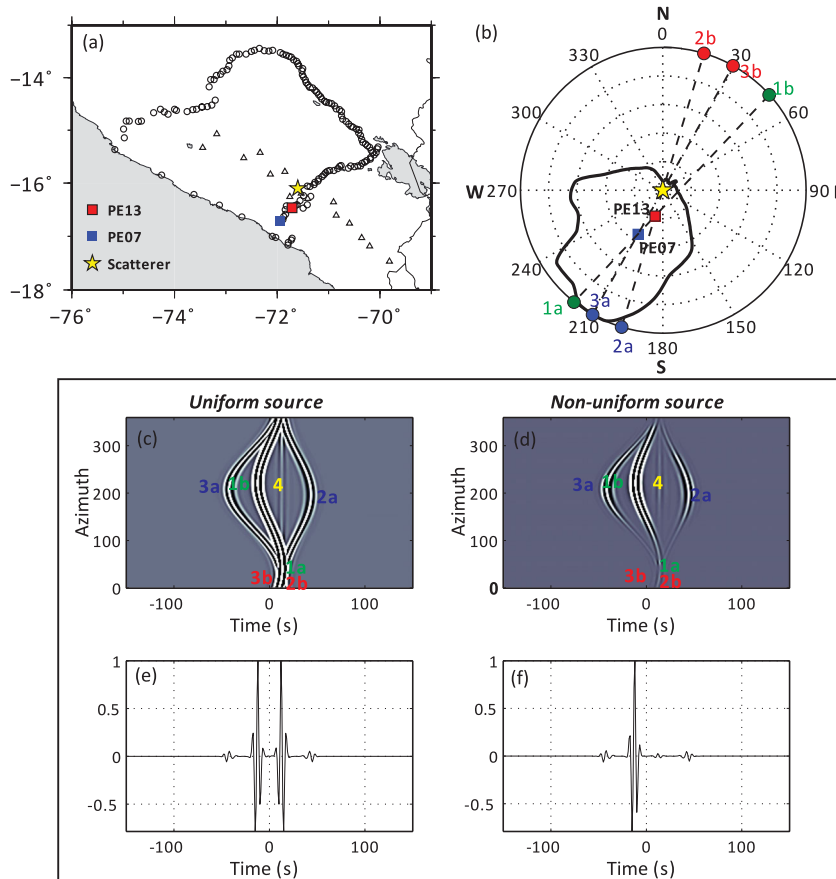


Figure 6. Modelling the cross-correlation between PE13 and PE07. The parameters used are: $\sigma^2 = 5.0 \text{ km}^2$ and $v_1 = 50$ per cent v_0 , where $v_0 = 3 \text{ km s}^{-1}$ is the background velocity. (a) Locations of the two stations and the scatterer. (b) A polar diagram showing the location of the stationary points of the cross-correlation. The black line is the source strength at different azimuths, and is strongest toward the coast and weakest in the opposite direction. (c) The cross-correlogram showing the cross-correlation for each source individually. The y-axis is the azimuth of the source. The colour represents the amplitude of the cross-correlation. The traces with stationary points are described in the text. (d) Same as (c), but for the non-uniform source case using the realistic source strength in (b). (e) The final cross-correlation from stacking all of the individual cross-correlations in (c). (f) The final cross-correlation from stacking all of the individual cross-correlations in (d). The synthetic result shown in (f) is similar to the data shown in pink in Fig. 2(a).

function. We take the cross-correlations between PE13 and PE07 and between PF25 and PF49 as two samples, and fit the precursor and coda amplitudes. We perform synthetics for a range of values including $\sigma^2 = 2.5, 5.0, 7.5, 10.0, 12.5$ and 15.0 km^2 and $v_1 = 30, 50, 70, 90, 110, 130, 150$ and 170 per cent v_0 .

A circular distribution of noise sources centred at the scatterer is assumed. The sources are placed 800 km from the scatterer so that they are in the far field compared with the scatterer–station distance. The source wavelet is a Ricker wavelet with a central period of 6 s. After calculating the waveforms recorded at the two stations from each source, we perform cross-correlations between the recordings for each source individually and stack them to get the final cross-correlation result. For the non-uniform source case, we weight the individual cross-correlations by the square of the source strength ($S'(\theta)$).

4.3 Modelling results

Fig. 5 shows the misfits for the coda amplitudes in the cross-correlation between PE13 and PE07 (pink trace in Fig. 2(a)), and the precursor amplitude in the cross-correlation between PF25 and PF49 (pink trace in Fig. 2(b)). As mentioned previously, our SNR estimate of source strength ($S(\theta)$) is an overestimate due to significant background scattering and uncorrelated noise, and we correct for this by subtracting a given percentage of the

minimum $S(\theta)$ to create our revised estimate $S'(\theta)$. Specifically, we set $S'(\theta) = S(\theta) - \xi \min[S(\theta)]$, where ξ is either 75, 50 or 100 per cent. Synthetics for these three modified source conditions are plotted in the three rows of Fig. 5.

We see that the coda misfits are mostly unaffected by the choice of source modification, with all three conditions giving the same optimal parameters of $\sigma^2 = 5.0 \text{ km}^2$ (i.e. $\sigma = 2.2 \text{ km}$) and $v_1 = 50$ per cent v_0 with about 27 per cent error. We note that this optimal Gaussian scatterer has a velocity perturbation of 30 per cent v_0 at one-sigma (2.2 km) radius. The coda fits are largely unaffected because, as shown in Fig. 6(b), coda amplitudes are primarily determined by sources close to the maximum in $S'(\theta)$ (towards the coast), which is nearly identical to $S(\theta)$ regardless of choice of ξ . The precursor misfits, though, are strongly affected by the modification. The precursor amplitude is related to the difference between the source strengths at the two stationary points since their contributions counteract each other. This difference is not affected if a constant value is subtracted from each. However, here, we try to fit the ratio between the precursor and direct wave amplitude. As shown in Fig. 7(b), for PF25-PF49, the stationary point of the direct wave is no longer in the very strong coastal direction, and thus is easily affected by the subtraction. With the optimal scatterer properties determined above, we find that $\xi = 75$ per cent fits the precursor best. Next, we will show the detailed modelling of the coda and precursor with our best fitting model, $\sigma^2 = 5.0 \text{ km}^2$, $v_1 = 50$ per cent v_0 and $\xi = 75$ per cent.

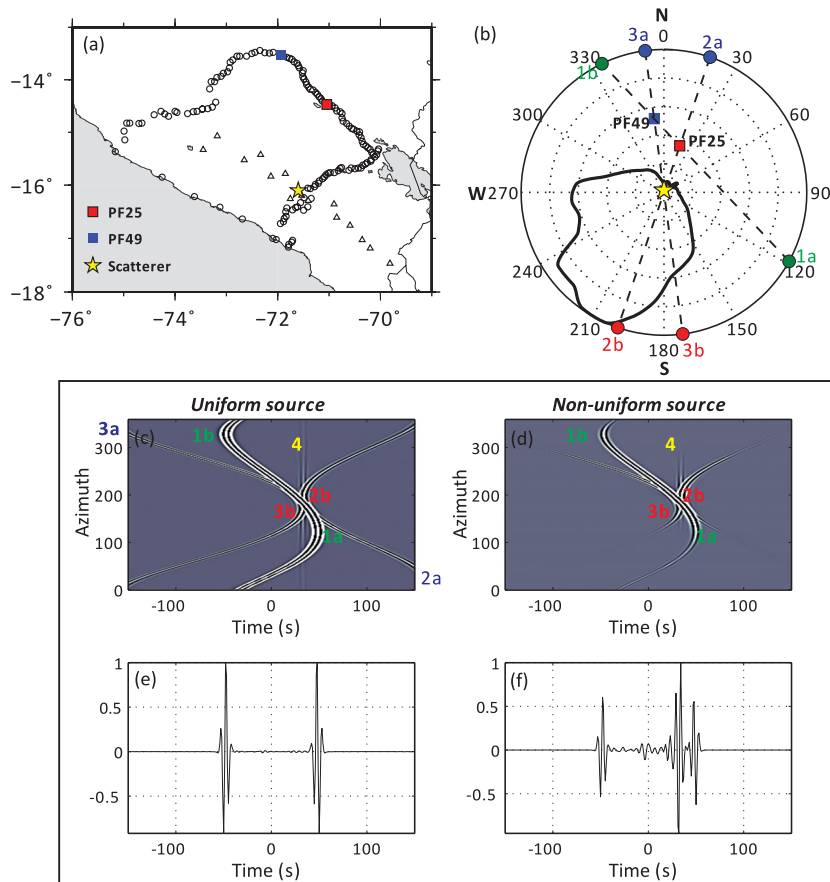


Figure 7. Modelling the cross-correlation between PF25 and PF49. Panels are as in Fig. 6, and use the same model parameters. We see that the precursor wave does not show up in the stacked cross-correlations, which means the contributions from 2b, 3b and 4 in (c) cancel each other. (f) The final cross-correlation from stacking all of the individual cross-correlations in (d). The precursor shows up in this non-uniform source case. This synthetic result in (f) is similar to the data shown in pink in Fig. 2(b).

Fig. 6 shows the simulated cross-correlation between PE13 and PE07. The location of the two stations and the scatterer is shown in Fig. 6(a). The source strength (thick black line) and stationary points (dots) are shown in the polar diagram (Fig. 6(b)). Both the uniform source and non-uniform source cases are shown. Figs 6(c) and (d) show the cross-correlations for each source individually, and Figs 6(e) and (f) are the final cross-correlations that result from stacking the individual cross-correlations in Figs 6(c) and (d), respectively. For both the uniform source and non-uniform source cases, the final cross-correlations are mainly from the four contributions labelled in Figs 6(c) and (d), respectively. Contribution 1 is from waves that directly travel from source to PE13 and PE07, and has two stationary points 1a and 1b corresponding to the two direct waves. Contribution 2 is the cross-correlation between one wave directly from the source to PE13 and one wave from the source to the scatterer then to PE07, and it has two stationary points for which 2a corresponds to the coda in the positive lag and 2b corresponds to the precursory arrival. Contribution 3 is the cross-correlation between one wave from the source to the scatterer and then to PE13 and one wave directly from the source to PE07, and it also has two stationary points for which 3a corresponds to the coda in the negative lag and 3b corresponds to the precursory arrival. Contribution 4 is the cross-correlation between two scattered waves and corresponds to the precursory arrival. We observe that the non-uniform case (Fig. 6f) fits the data well (*cf.*, the pink trace in Fig. 2a).

While the precursor is difficult to distinguish from the direct wave in the positive lag in the first example, they are well separated in the simulated cross-correlation between PF25 and PF49, as shown in Fig. 7. In Figs 7(c) and (d), which are the cross-correlations for each source individually, we see clearly that the stationary points 2b and 3b as well as contribution 4 all correspond to the precursor arrival time. In the uniform source case, the final stacked cross-correlation (Fig. 7e) shows no precursor signal, because the contributions from 2b, 3b and 4 cancel out, as predicted by theory (Snieder *et al.* 2008). However, for the non-uniform source case, the precursor does clearly emerge. The polar diagram (Fig. 7b) shows that the source strength corresponding to 2b and 3b differs significantly, which means the contributions cannot cancel.

We also produce synthetics for the two profiles shown in Fig. 2. The results are shown in Fig. 8, and are plotted with the same scale as the data in Fig. 2. The travel times are predicted with the phase velocity of 3 km s^{-1} used in the synthetics. Both sets of synthetics produce envelope amplitudes that fit the data reasonably well (*cf.*, Fig. 2). The variation in the amplitude of the precursor and coda is the same as that in the data. In general, the coda amplitude is related to the source strength at its stationary point (Fig. 3b for positive lag and Fig. 3c for negative lag). The precursor amplitude is related to the difference between the source strengths at its two stationary points (Figs 3d and e) since their contributions counteract each other as stated in Section 2 and modelled in Section 4 (Fig. 7).

For the PE13 profile (Fig. 8a), the scatterer is near co-linear with the PE line (stations numbered from coastal to inland) and is approximately at PE19 (see Fig. 1). The stationary point of the coda in the positive lag is in the direction pointing from the scatterer to PE13, and is in the coastal direction where the noise source is the strongest. Consequently, the coda in the positive lag should always be observable in PE13 profile, except for the distance range of PE19–PE50, where the positive coda travel time is so close to the direct wave that it is hidden by the direct wave. The stationary point of the coda in the negative lag is in the direction pointing from the scatterer to STA2, which is in the strong-source coastal direction when STA2 is in the range of PE03–PE19, and is in the weak-source inland

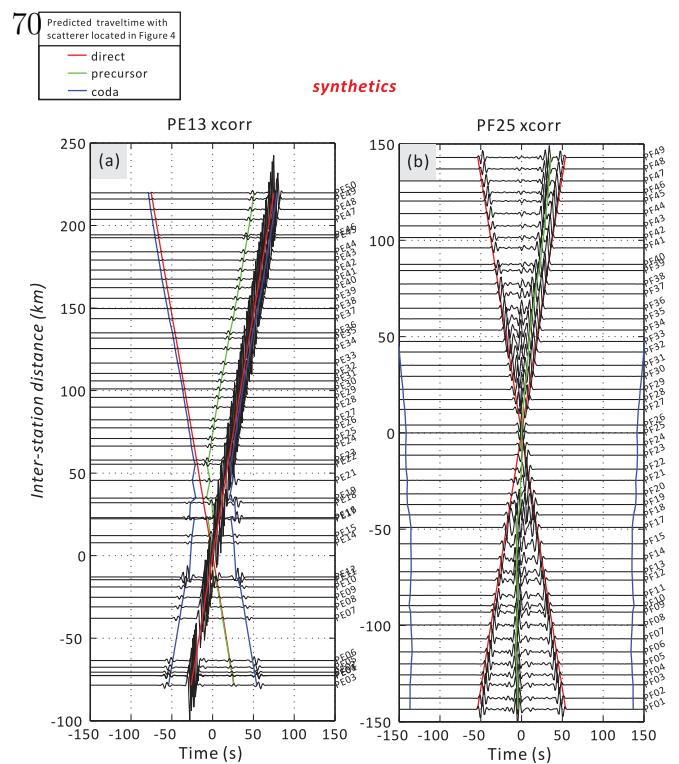


Figure 8. Modelling the cross-correlations between (a) PE13 and all PE stations, and (b) PF25 and all PF stations. The parameters used are: $\sigma^2 = 5.0 \text{ km}^2$ and $v_1 = 50$ per cent v_0 , where $v_0 = 3 \text{ km s}^{-1}$ is the background velocity. The synthetics match the envelope amplitude of the data in Fig. 2 reasonably well. See the text for the discussion of the variations in the precursor and coda amplitudes.

direction when STA2 is in the range of PE19–PE50. Therefore, the coda in the negative lag becomes invisible when STA2 changes from coastal to inland of PE19. For the precursor, when STA2 is in the range of PE03–PE19, the two stationary points are both in the inland direction and are so close that the difference in their source strengths is very small (e.g. Fig. 6b). As a result, the precursor is weak. However, when STA2 is in the range of PE19–PE50, the two stationary points are in the opposite directions (coastal and inland), which results in a strong precursor, as observed in Fig. 2(a).

For the PF25 profile (Fig. 8b), the coda stationary points for each station pair in this profile are always in the inland directions where the noise sources are weak, and therefore are always unrecognizable. However, the precursor stationary points are well separated and the source strengths differ significantly (e.g. Fig. 7b), and therefore the precursors are always strong in this profile, as observed in Fig. 2(b).

Since we use membrane wave modelling, we cannot directly determine the vertical size of the scatterer. Surface wave (group and phase) velocities are determined by an integral over structure with depth, but are most sensitive to shear velocity structure at depths of about one-third of their wavelength (Weeraratne *et al.* 2003; Yang *et al.* 2007). Since we use cross-correlations between 5 and 10 s period and phase velocities are about 3 km s^{-1} at 6 s in this region, we can deduce that the scatterer likely exists at depths of 5–10 km, where the velocity perturbation required is the smallest. If the scatterer were only at much shallower or deeper depths (e.g. $\mp 5 \text{ km}$), it would require a much larger velocity contrast, which we consider to be unlikely. However, we do not exclude the possibility that the scatterer extends much deeper than 10 km. We also note that we have not tested non-Gaussian scatterer models, which may

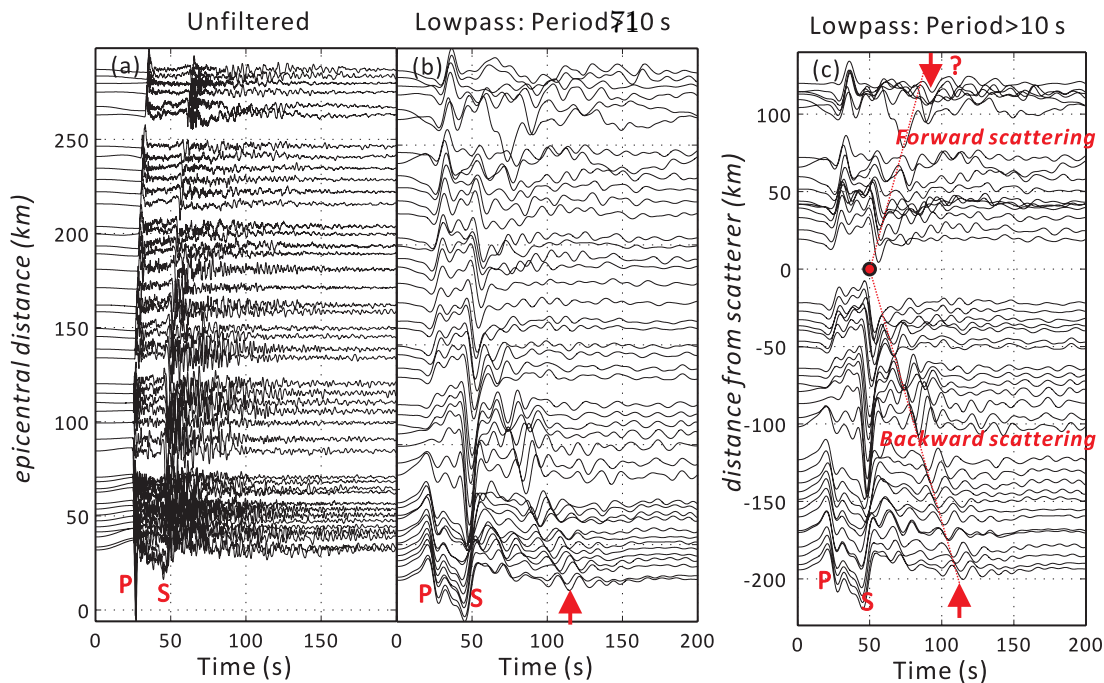


Figure 9. Vertical-component seismograms showing a clear backscattered wave. The hypocenter of the earthquake is the red star in Fig. 1. The epicentral depth is 210.2 km and the magnitude is 5.8. (a) Unfiltered data show clear *P* and *S* waves. (b) Low-pass filtered to period larger than 10 s. Clear backscattered waves appear, marked with the red arrow. (c) Traces sorted by the distance to the scatterer (yellow star in Fig. 1). The positive direction represents stations in the forward scattering region and the negative direction represents those in the backward scattering region. The backscattered wave shows a linear increase of travel time with distance and a velocity of about 3 km s^{-1} , indicating that it is a surface wave. The arrival time of the scattered wave at 0 km distance coincides with the *S* wave, which indicates that the energy is from scattering of the *S* wave. The forward scattered wave can also be observed though not as clearly.

also fit the data reasonably well but would have different model parameters.

5 CONFIRMATION BY AN EARTHQUAKE SOURCE

The scattering results shown above are confirmed by an earthquake recording with a clear backscattered wave (Fig. 9). This earthquake had an epicentral depth of 210 km and a magnitude of 5.8, and its hypocenter is shown as a red star in Fig. 1. The unfiltered (vertical component) seismograms (Fig. 9a) show clear *P* and *S* waves, and when they are low-pass filtered to periods longer than 10 s (Fig. 9b), we see a clear backscattered wave. In Fig. 9(c), we sort the traces according to distance from the scatterer, and distinguish the backward and forward scattering by negative and positive distances. We observe that the travel time of the backscattered wave is now a linear function of distance, and the velocity is about 3 km s^{-1} , which indicates that it is a surface wave. At zero offset, the scattered wave is coincident with the *S*-wave arrival, which indicates that the energy is from scattering of the *S* wave. The generation of a scattered surface wave indicates that the scatterer is shallow, consistent with our preferred scattering model of Section 4.

6 DISCUSSION AND CONCLUSIONS

We have determined that the strong precursor and coda arrivals that appear in the ambient noise cross-correlations within an array in Southern Peru are due to a scatterer located at $71.6^\circ\text{W}/16.1^\circ\text{S}$ with an error of about 10 km. The scatterer can be satisfactorily modelled as a vertical cylinder with a Gaussian distribution of velocity, but it is

only required at depths of 5–10 km. The velocity at the centre of the Gaussian scatterer is 50 per cent of the background velocity, and at one-sigma (2.2 km) radius is 30 per cent lower than the background velocity. The scattering effects are confirmed by examining a local earthquake.

The scatterer is located within the volcanic arc of the subduction zone in Southern Peru and, as such, is likely related to volcanic processes. For example, it could be a low-velocity magma chamber. Nagaoka *et al.* (2012) imaged the magma chamber beneath an active volcano in Japan using ambient noise cross-correlations. Their phase velocity map (Fig. 3d therein) at periods of 5–10 s shows a ~ 20 per cent lower velocity anomaly with radius of about 5 km. The *S*-wave velocity anomaly is about 5–10 km deep, and is ~ 8 km offset from the nearby volcanic edifice. The features of their magma chamber are quite similar to the scatterer discussed here. Our best-fit location of the scatterer is closest to (~ 10 km away from) the volcano Nevado Chachani which is presently inactive, and is about 30 km from the active volcano El Misti. Considering our location errors, the scatterer could be related to either of these volcanoes. The scatterer is close to but approximately 50 km outside of the Hualca Hualca inflation anomaly reported by previous InSAR studies (Pritchard & Simons 2002, 2004). Note that the inflation stopped in 1997 during their study, which is perhaps related to a large eruption of nearby Sabancaya volcano (Pritchard & Simons 2004).

This study points out that scatterers can generate coherent arrivals on ambient noise surveys, particularly when the geometry of the survey is such that the distribution of the ambient noise sources favours the creation of the precursor waves over the direct wave Green's functions. If the array did not have the density of the one used in this study, the identification of the scattering and the location

of the scatterer may not have been possible. Without careful analysis, or with a sparse array, scattered arrivals could be mistaken for direct waves, and hence the inferred velocities would be incorrect. Passive scatterers join a list of effects (gaps in azimuthal sources, active sources, etc.) that cause arrivals in ambient noise surveys that can be misidentified as direct waves.

ACKNOWLEDGMENTS

We thank Fan-Chi Lin at Caltech for providing many useful suggestions and thank Dunzhu Li at Caltech for providing the finite-difference code. We also thank two anonymous reviewers for their helpful comments. Contribution number 212 from the Tectonics Observatory at Caltech. This work is supported by NSF (EAR-1045683) and the Gordon and Betty Moore Foundation.

REFERENCES

- Bensen, G.D., Ritzwoller, M.H., Barmin, M.P., Levshin, A.L., Lin, F., Moschetti, M.P., Shapiro, N.M. & Yang, Y., 2007. Processing seismic ambient noise data to obtain reliable broad-band surface wave dispersion measurements, *Geophys. J. Int.*, **169**, 1239–1260.
- Brenguier, F., Shapiro, N.M., Campillo, M., Ferrazzini, V., Duputel, Z., Coutant, O. & Nercessian, A., 2008. Towards forecasting volcanic eruptions using seismic noise, *Nat. Geosci.*, **1**, 126–130.
- Brenguier, F., Shapiro, N.M., Campillo, M., Nercessian, A. & Ferrazzini, V., 2007. 3-D surface wave tomography of the Piton de la Fournaise volcano using seismic noise correlations, *Geophys. Res. Lett.*, **34**, doi:10.1029/2006GL028586.
- Hasselmann, K., 1963. A statistical analysis of the generation of microseisms, *Rev. Geophys.*, **1**, 177–210.
- Kawakatsu, H., Ohminato, T. & Ito, H., 1994. 10s-period volcanic tremors observed over a wide area in Southwestern Japan, *Geophys. Res. Lett.*, **21**, 1963–1966.
- Lin, F.C., Moschetti, M.P. & Ritzwoller, M.H., 2008. Surface wave tomography of the western United States from ambient seismic noise: Rayleigh and Love wave phase velocity maps, *Geophys. J. Int.*, **173**, 281–298.
- Lin, F.C., Ritzwoller, M.H. & Shen, W.S., 2011. On the reliability of attenuation measurements from ambient noise cross-correlations, *Geophys. Res. Lett.*, **38**, doi:10.1029/2011GL047366.
- Lobkis, O.I. & Weaver, R.L., 2001. On the emergence of the Green's function in the correlations of a diffuse field, *J. Acoust. Soc. Am.*, **110**, 3011–3017.
- Longuet-Higgins, M.S., 1950. A theory of the origin of microseisms, *Philos. Trans. R. Soc. Lond., A*, **243**, 1–35.
- Nagaoka, Y., Nishida, K., Aoki, Y., Takeo, M. & Ohminato, T., 2012. Seismic imaging of magma chamber beneath an active volcano, *Earth planet. Sci. Lett.*, **333**, 1–8.
- Pritchard, M.E. & Simons, M., 2002. A satellite geodetic survey of large-scale deformation of volcanic centres in the central Andes, *Nature*, **418**, 167–171.
- Pritchard, M.E. & Simons, M., 2004. An InSAR-based survey of volcanic deformation in the central Andes, *Geochem. Geophys. Geosyst.*, **5**, doi:10.1029/2003GC000610.
- Shapiro, N.M. & Campillo, M., 2004. Emergence of broadband Rayleigh waves from correlations of the ambient seismic noise, *Geophys. Res. Lett.*, **31**, doi:10.1029/2004GL019491.
- Shapiro, N.M., Campillo, M., Stehly, L. & Ritzwoller, M.H., 2005. High-resolution surface-wave tomography from ambient seismic noise, *Science*, **307**, 1615–1618.
- Shapiro, N.M., Ritzwoller, M.H. & Bensen, G.D., 2006. Source location of the 26 sec microseism from cross-correlations of ambient seismic noise, *Geophys. Res. Lett.*, **33**, L18310, doi:10.1029/2006GL027010.
- Snieder, R., van Wijk, K., Haney, M. & Calvert, R., 2008. Cancellation of spurious arrivals in Green's function extraction and the generalized optical theorem, *Phys. Rev. E*, **78**, 036606, doi:10.1103/PhysRevE.78.036606.
- Stehly, L., Campillo, M. & Shapiro, N.M., 2006. A study of the seismic noise from its long-range correlation properties, *J. geophys. Res. Solid Earth*, **111**, doi:10.1029/2005JB004237.
- Tanimoto, T., 1990. Modeling curved surface-wave paths – membrane-surface wave synthetics, *Geophys. J. Int.*, **102**, 89–100.
- Wapenaar, K., 2004. Retrieving the elastodynamic Green's function of an arbitrary inhomogeneous medium by cross correlation, *Phys. Rev. Lett.*, **93**, doi:10.1103/PhysRevLett.93.254301.
- Wapenaar, K., Slob, E. & Snieder, R., 2010. On seismic interferometry, the generalized optical theorem, and the scattering matrix of a point scatterer, *Geophysics*, **75**, Sa27–Sa35.
- Weeraratne, D.S., Forsyth, D.W., Fischer, K.M. & Nyblade, A.A., 2003. Evidence for an upper mantle plume beneath the Tanzanian craton from Rayleigh wave tomography, *J. geophys. Res.*, **108**, 2427, doi:10.1029/2002JB002273.
- Yang, Y. & Ritzwoller, M.H., 2008. Characteristics of ambient seismic noise as a source for surface wave tomography, *Geochem. Geophys. Geosyst.*, **9**, doi:10.1029/2007GC001814.
- Yang, Y., Ritzwoller, M.H., Levshin, A.L. & Shapiro, N.M., 2007. Ambient noise Rayleigh wave tomography across Europe, *Geophys. J. Int.*, **168**, 259–274.
- Yao, H., Campman, X., de Hoop, M.V. & van der Hilst, R.D., 2009. Estimation of surface wave Green's functions from correlation of direct waves, coda waves, and ambient noise in SE Tibet, *Phys. Earth planet. Inter.*, **177**, 1–11.
- Yao, H., van der Hilst, R.D. & de Hoop, M.V., 2006. Surface-wave array tomography in SE Tibet from ambient seismic noise and two-station analysis – I. Phase velocity maps, *Geophys. J. Int.*, **166**, 732–744.
- Zeng, X.F. & Ni, S.D., 2010. A persistent localized microseismic source near the Kyushu Island, Japan, *Geophys. Res. Lett.*, **37**, doi:10.1029/2010GL045774.
- Zeng, X. & Ni, S., 2011. Correction to “A persistent localized microseismic source near the Kyushu Island, Japan”, *Geophys. Res. Lett.*, **38**, L16320, doi:10.1029/2011GL048822.
- Zhan, Z.W., Ni, S.D., Helmberger, D.V. & Clayton, R.W., 2010. Retrieval of Moho-reflected shear wave arrivals from ambient seismic noise, *Geophys. J. Int.*, **182**, 408–420.
- Zheng, Y., Shen, W.S., Zhou, L.Q., Yang, Y.J., Xie, Z.J. & Ritzwoller, M.H., 2011. Crust and uppermost mantle beneath the North China Craton, north-eastern China, and the Sea of Japan from ambient noise tomography, *J. geophys. Res. Solid Earth*, **116**, doi:10.1029/2011JB008637.

Chapter 5

The crust and uppermost mantle structure of Southern Peru from ambient noise and earthquake surface wave analysis

1



The crust and uppermost mantle structure of Southern Peru from ambient noise and earthquake surface wave analysis



Yiran Ma*, Robert W. Clayton

Seismological Laboratory, California Institute of Technology, CA 91125, USA

ARTICLE INFO

Article history:

Received 17 December 2013
Received in revised form 7 March 2014
Accepted 8 March 2014
Available online 4 April 2014
Editor: P. Shearer

Keywords:

Central Andes
flat subduction
surface wave tomography

ABSTRACT

Southern Peru is located in the northern Central Andes, which is the highest plateau along an active subduction zone. In this region, the Nazca slab changes from normal to flat subduction, with the associated Holocene volcanism ceasing above the flat subduction regime. We use 6 s to 67 s period surface wave signals from ambient noise cross-correlations and earthquake data, to image the shear wave velocity (V_{SV}) structure to a depth of 140 km. A mid-crust low-velocity zone is revealed, and is interpreted as partially molten rocks that are part of the Andean low-velocity zone. It is oblique to the present trench, and possibly indicates the location of the volcanic arcs formed during the steepening of the Oligocene flat slab beneath the Altiplano plateau. The recently subducted slab beneath the forearc shows a decrease in velocity from the normal to flat subduction regime that might be related to hydration during the formation of the Nazca ridge, which in turn may contribute to the buoyancy of the flat slab. The mantle above the flat slab has a comparatively high velocity, which indicates the lack of melting and thus explains the cessation of the volcanism above. A velocity contrast from crust to uppermost mantle is imaged across the Cusco–Vilcanota Fault System, and is interpreted as the boundary between two lithospheric blocks.

© 2014 Elsevier B.V. All rights reserved.

1. Introduction

Southern Peru is an interesting area to study subduction, orogeny and the related volcanism processes along an active continental margin. The dip of the subducted Nazca slab changes from 30° in the southeast to nearly horizontal at a depth of ~100 km in the northwest (Fig. 1). Closely linked with the subduction process, the Quaternary volcanic arc is well developed where the slab is steeper and is absent where the slab is nearly flat (Allmendinger et al., 1997). This area is also characterized by the over 4 km high orogeny of the Central Andes. The high topography is widest above the normal subduction regime, and narrows considerably to the northwest over the flat subduction regime. From the coast to inland, the main tectonic units include the offshore and onshore forearc region, the Western Cordillera, the Altiplano plateau, and an eastern belt of fold and thrust structures comprising the Eastern Cordillera and the Sub-Andean Ranges (Fig. 1) (Oncken et al., 2006). The major crustal thickening is suggested to have initiated around 30–40 Ma (asynchronous for each tectonic unit), and is continuing to present (Mamani et al., 2010; Oncken et al., 2006).

Recent studies in Southern Peru using receiver functions (Phillips and Clayton, 2014; Phillips et al., 2012) suggest that the crustal thickness changes from ~20 km near the coast to ~70 km below the Altiplano plateau. The crustal P-wave structure under the plateau has been investigated by an active seismic survey along a profile from Peru to Bolivia, and is characterized by two low-velocity layers at 9–12 km and 36–46 km depth ranges (Ocola and Meyer, 1972). The deeper layer at the mid-crust depth is also detected in the receiver function (Yuan et al., 2000) and ambient noise surface wave (Ward et al., 2013), as well as other geophysical observations (Schilling et al., 2006) in the Central Andes, and is interpreted as a large volume of molten rocks (Schilling et al., 2006; Yuan et al., 2000). The extensive crustal melting can be attributed to the steepening of an Oligocene flat slab beneath the Altiplano plateau and an early Miocene flat slab beneath the Puna plateau (Kay and Coira, 2009; Ramos and Folguera, 2009). The mantle-wedge convection and arc volcanism resumed when the flat slab began to steepen, and because of the increase in the dip of the slab, the arc migrated trench-ward from inland to the present location (Allmendinger et al., 1997; Mamani et al., 2010) leading to widespread magmatism and heat input into the crust, which caused the crustal melting. While the magmatic addition is not as important as tectonic shortening to the crustal thickening, it had a

* Corresponding author.

E-mail address: yrma@caltech.edu (Y. Ma).

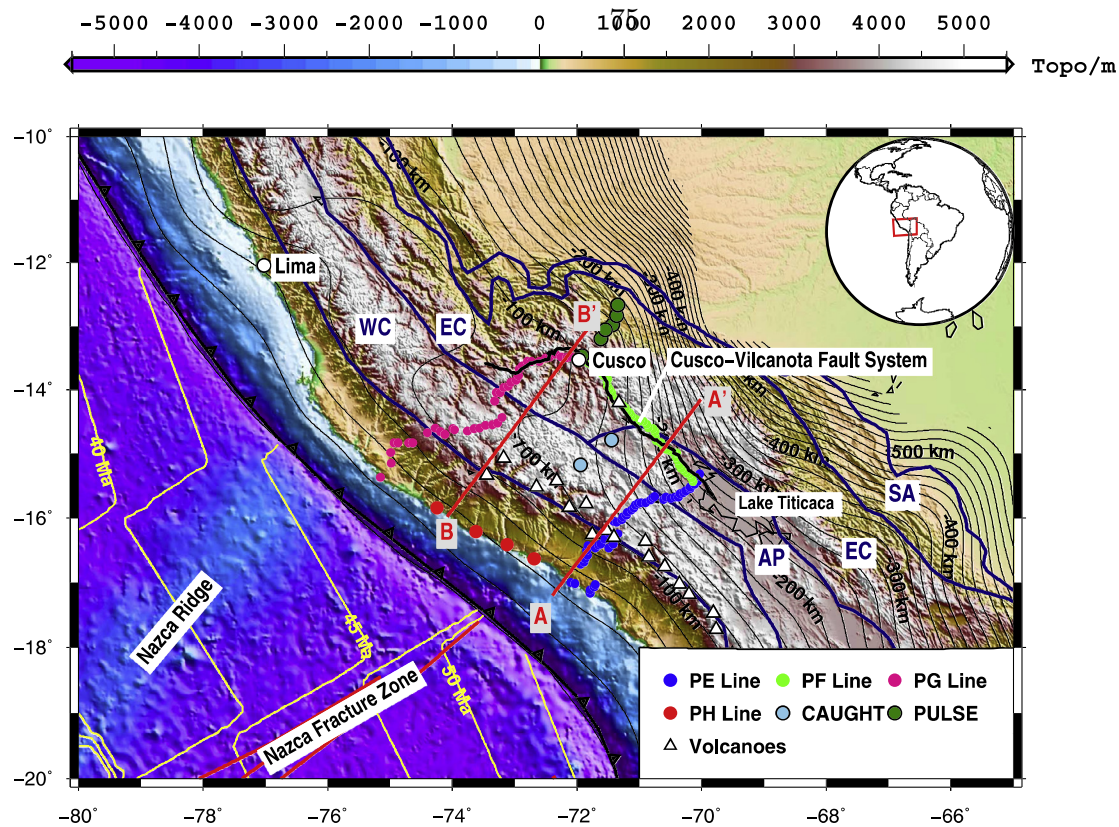


Fig. 1. Location of the seismic stations (dots) used in this study. The main units building the Central Andes are delineated with navy lines (modified from Oncken et al., 2006). WC: Western Cordillera; EC: Eastern Cordillera; AP: Altiplano Plateau; SA: Sub-Andean Ranges. The Holocene volcanoes are denoted with white triangles (data from <http://www.volcano.si.edu/world>). The thick black line is the Cusco-Vilcanota Fault System digitized from Carlier et al. (2005). Slab contours are from <http://earthquake.usgs.gov/research/data/slab>, plotted at 20 km intervals. The Nazca fracture zone data are from <http://www.soest.hawaii.edu/PT/GSFML>. Ocean floor age data are from <http://www.earthbyte.org/Resources/Agegrid/2008/grids>, plotted in 2.5 Ma intervals. Topography data are from <http://glcf.umd.edu/data/srtm>.

major effect on rheology and the mechanical behavior of the crust (Allmendinger et al., 1997).

The Peruvian flat subduction is not unique, as approximately 10 percent of present day subduction zones are considered to have flat slabs (Gutscher et al., 2000; Skinner and Clayton, 2013). Many of the present normal subduction regimes, such as the ones under Altiplano and Puna plateaux (Ramos and Folguera, 2009) mentioned above, are also considered to have experienced flat subduction in the past. The major driving forces of the flat subduction are still unknown, but some possible causes are summarized in Gutscher (2002), among which the subduction of thickened oceanic crust (e.g. the Nazca ridge and the Inca Plateau Gutscher et al., 1999) is suggested to be the dominant one. However, Skinner and Clayton (2013) argue through plate reconstructions that there is no clear correlation between the arrival of the thickened crust and the onset of slab flattening in South America. In addition, geodynamical modeling (Gerya et al., 2009) shows that the buoyancy of the thickened crust itself is not sufficient to raise the slab to the flat orientation, even including a less-dense depleted mantle associated with the formation of a thick crust (Abbott, 1991). The importance of the enhanced mantle wedge suction caused by the thick continental craton near the subduction zone is raised by several other studies (Manea et al., 2012; O'Driscoll et al., 2012). For example, O'Driscoll et al. (2012) suggested that the subduction towards the Amazonian Craton of South America, which is close to the trench, contributed to the flattening of the slab beneath the Altiplano plateau during the late Eocene and Oligocene, while the steepening of this Oligocene flat slab was associated with a change in the subduction direction, which resulted in a weakened wedge suction.

In this paper, we present the velocity structure in the crust and uppermost mantle from surface wave analysis. We show the extent of the mid-crust Andean low-velocity zone in the study region, the two lithosphere blocks across the Cusco-Vilcanota Fault System, and the velocity differences between the flat and normal subduction regimes. This study complements the receiver function studies of Phillips et al. (2012) and Phillips and Clayton (2014) that focuses on the velocity discontinuities (e.g. the Moho and slab depths) of this area.

2. Data and method

The data used in this study are primarily from a box-like array deployed progressively from June 2008 to February 2013 in Southern Peru (Fig. 1). The array is composed of ~150 broadband stations (PE, PF, PG, PH lines), each with ~2 yrs of deployment. We also use data from 8 broadband stations from the CAUGHT and PULSE experiments (Ward et al., 2013). We correct the data for the instrument response, integrate the velocity records to displacement, and use the vertical 1-sample/s channel to obtain the Rayleigh wave signals.

The phase velocity of Rayleigh wave is sensitive to the shear velocities over a range of depths, but is most sensitive to a depth range that is approximately one-third of its wavelength. By combining the phase velocities at various periods, we are able to invert for the shear wave velocity structure as a function of depth. For periods 6 s to 25 s, we use the surface wave signals from the ambient noise cross-correlations, and for 25 s to 67 s, we use the earthquake surface wave signals. We first make a phase velocity map of the area for each period and then perform a 1-D structure

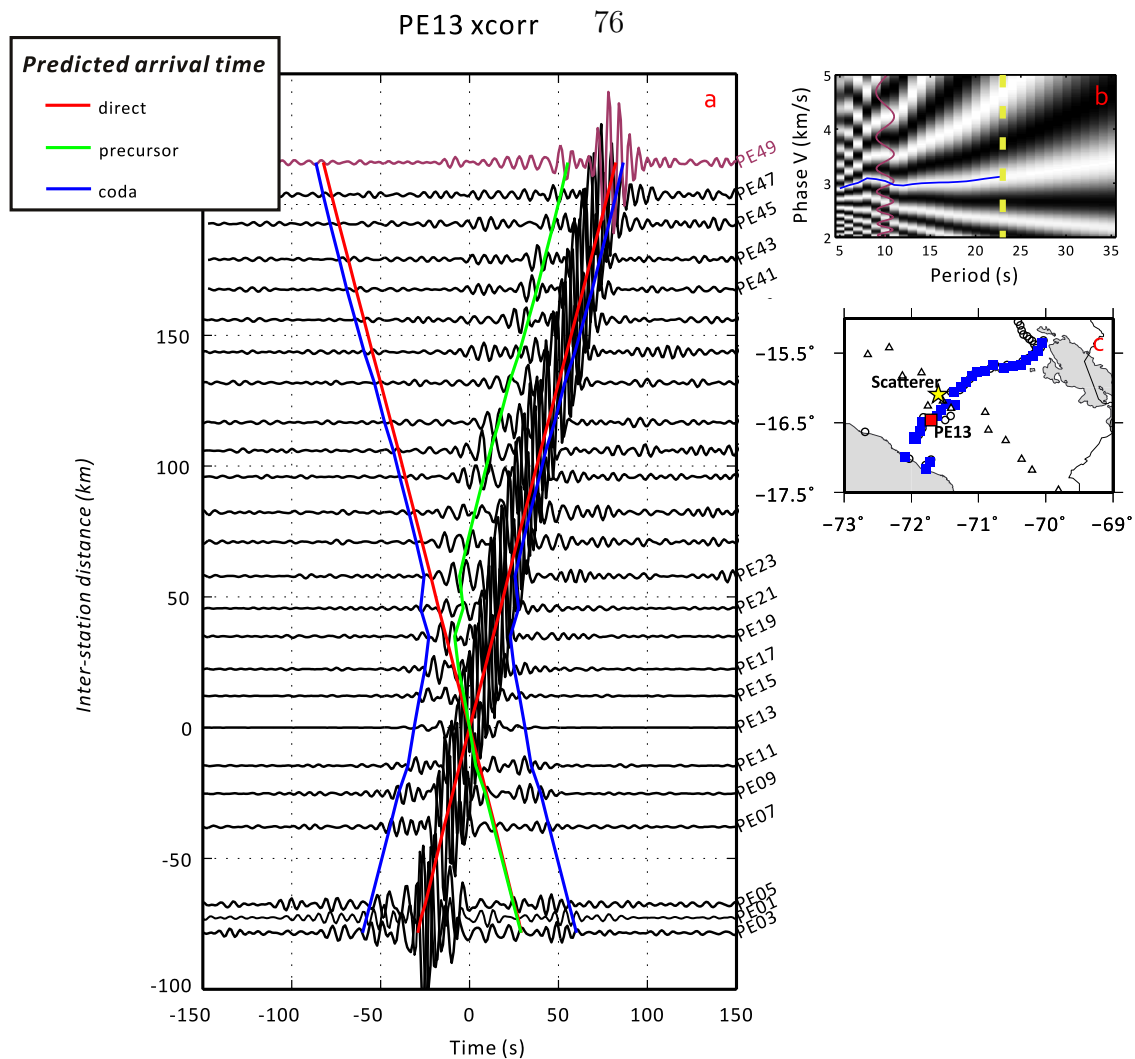


Fig. 2. (a) The cross-correlations between PE13 and all the odd number stations on PE line (see Panel c for the stations). The stations are numbered from the coast to inland. Also shown are the predicted arrival time of the precursor and coda waves due to the scatterer located in Panel c. (b) An example of measuring the dispersion curve of the cross-correlation between PE13 and PE49 (pink trace in Panel a). The yellow dashed line indicates the maximum period can be measured in order to satisfy the far field approximation (see text for more details). (c) The stations used in the cross-correlations in Panel a. Also shown is the location of the strong surface-wave scatterer (Ma et al., 2013). (For interpretation of the references to color in this figure legend, the reader is referred to the web version of this article.)

inversion on the dispersion curve at each location on the map. The 1-D structures are then combined to make a 3-D structure.

2.1. Ambient noise

The surface wave portion of the ambient noise cross-correlations has been used extensively to determine the earth structure (Brenuier et al., 2007; Lin et al., 2008; Shapiro et al., 2005; Yao et al., 2006). Here, we use a similar method to Bensen et al. (2007) to perform vertical-vertical cross-correlations between all station pairs in this array. We then use the method by Yao et al. (2006) to measure the phase velocity dispersion curve for each cross-correlation. Finally, we use a similar method to Barmin et al. (2001) to invert for the phase velocity map at each period.

Fig. 2a shows an example of the cross-correlations between station PE13 and all the odd number stations on line PE. The cross-correlations are dominantly one-sided because the noise sources are not uniformly distributed, with the strongest on the Pacific Ocean side. The synthetics in Ma et al. (2013) shows that this non-uniform distribution of noise source does not cause a bias in the traveltimes of the inter-station surface wave. We can also observe that continuous signals arrive earlier (denoted with green line) or

later (denoted with blue line) than the inter-station surface wave. These are due to a scatterer (yellow star in Fig. 2c), which was reported by Ma et al. (2013), and for the purposes of the structure inversion, we ignore these arrivals. For each station pair, we stack the positive and negative time lags of the cross-correlation, and measure the dispersion curve from the stacked waveform (e.g. Fig. 2b for PE13–PE50), following Yao et al. (2006). Two criteria are used in accepting the measurement at certain period. First, the threshold of signal-to-noise ratio (SNR) is empirically set at 5 to eliminate the irregular (e.g. unsmooth) segments of the dispersion curve in noisy period bands. Note that since the ambient noise energy is peaked around 5 s and 15 s, and also because the scattering effect is strongest at short periods, fewer station pairs satisfy the SNR criterion at longer or shorter periods. Second, the maximum wavelength λ (and hence the maximum period) is limited by the inter-station distance Δ (usually $\Delta \geq 3\lambda$) in order to satisfy the far field approximation in the measurement procedure (Lin et al., 2008; Yao et al., 2006). This reduces the resolution of the tomographic inversion for longer periods, and because of these restrictions, we only use the ambient noise measurements from 6 s to 25 s period.

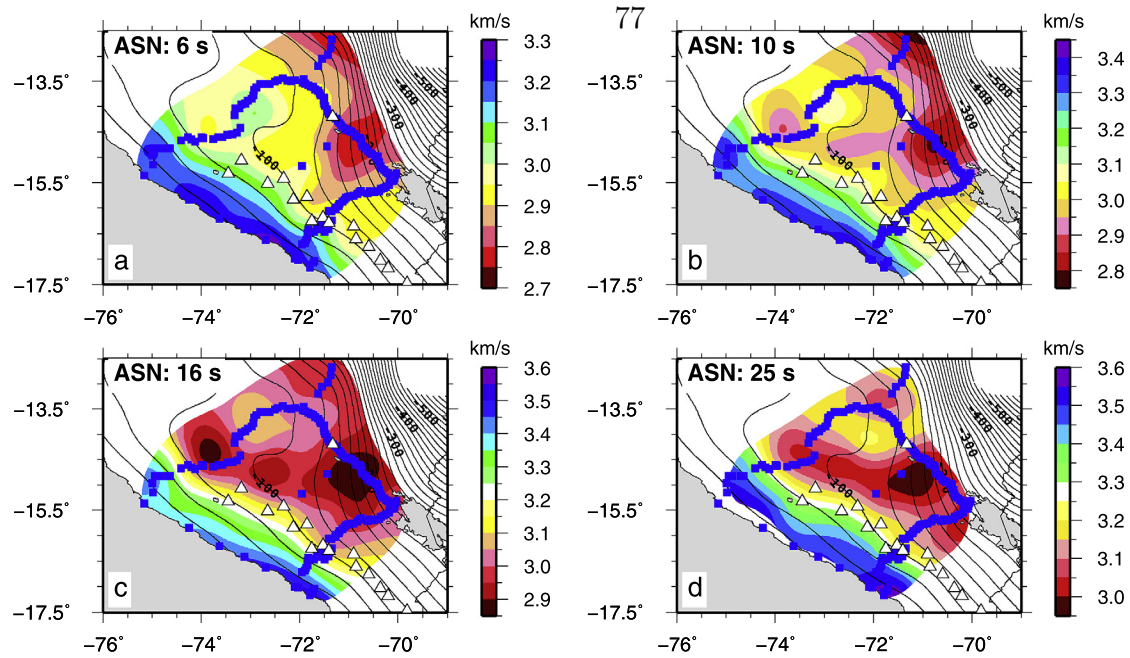


Fig. 3. Ambient noise phase velocity maps at 6, 10, 16 and 25 s periods. The results are clipped with model error less than 10% of the average velocity in each period.

The phase velocity maps at each period are inverted from the inter-station dispersion measurements. The region is discretized into a $0.5^\circ \times 0.5^\circ$ grid, and for each period, a linear inversion for the slowness model is done using the method of Barmin et al. (2001). The penalty function includes the data misfit and model smoothness, as well as constraints on model curvature in order to be consistent with the earthquake method (Forsyth and Li, 2005; Yang and Forsyth, 2006a, 2006b), which is discussed in Section 2.2. For the smoothness term, the correlation length (σ in the Gaussian function) is set at 1° , and we use the trade-off curve between misfit and model smoothness (Aster et al., 2012; Hansen, 1992) to determine the regularization parameter. For the curvature term, the regularization parameter is calculated to minimize (in least squares sense) the off-diagonal terms of model covariance matrix. Two iterations are performed. With the first iteration, all data are equally weighted, and we also apply heavy damping, which results in a highly smoothed model. For the second iteration, the data are weighted inversely proportional to their misfits in the first iteration. The i -th diagonal element of the data covariance matrix is specified as $\max(e_i, w)^2$, where e_i is the misfit of the i -th data after the first iteration, and w is the water level cutoff to ensure stability. The resulting slowness map is then converted to the phase velocity map, which is shown in Fig. 3.

The resolution and model error at two representative periods – 6 s and 25 s – are shown in Supplementary Fig. 1. Due to the small size of the problem, we can directly use the resolution matrix $R = (G^T C^{-1} G + Q)^{-1} G^T C^{-1} G$ (where C is the data covariance matrix, Q is the regularization matrix, and G is the forward operator on the slowness model) from the inversion above to generate standard checkerboard resolution maps. Here, the input model contains ± 10 percent perturbations of the average velocity, and the output model (expressed in percentage) is shown in Supplementary Fig. 1a–b. The error of the model is estimated from the diagonal elements of the model covariance matrix, which is approximately $C_{mm} = (G^T C^{-1} G + Q)^{-1}$ and is typically smaller than 0.05 km/s inside of the array (Supplementary Fig. 1c–d). The model error reflects the variance of the model subject to the variance of the data, and does not reflect the deviation from the true model where the resolution is low.

2.2. Earthquake two-plane wave

The earthquakes we used are selected from the NEIC catalog, using a search window with magnitude larger than 6.0, depth less than 100 km, and epicentral distance in the range of $30\text{--}120^\circ$ (Supplementary Fig. 2). We used the “two-plane-wave method” (Forsyth and Li, 2005; Yang and Forsyth, 2006a, 2006b) to determine the phase velocity structure from 25–67 s period. With this method, the incoming wavefield from one earthquake is represented by the superposition of two plane waves, each with unknown amplitude, initial phase and direction. This approximately accounts for multipathing and the off-great circle path of the surface wave (e.g. Cotte et al., 2002). From the amplitude and phase information recorded by an array of stations, we are able to invert for those wave parameters and the local phase velocity structures as well as other parameters such as site amplification and 1-D attenuation.

In processing the data, we first visually inspect all the data and delete those with obvious recording problems or complex waveforms. The data are then filtered with a series of narrow band-pass (10 mHz), zero-phase, fourth-order Butterworth filters centered at the periods of 25, 29, 33, 40, 45, 50, 59 and 67 s. We then window the surface wave part of each seismogram. The window length is 200 s for periods less than 60 s, and 300 s for 67 s. A 50 s half-cosine taper is added to each end of the window. To find the center of the window, we first measure the group velocity dispersion curve for each station, which gives the arrival time of the surface wave envelope at each period. These estimates are further refined by comparing all the stations for one event. Finally, from the windowed seismograms, the amplitude and phase information is determined. In the inversion procedure, a finite-frequency kernel (Zhou et al., 2004) is used for each period, instead of an empirical Gaussian kernel as was used in the ambient noise tomography.

The nonlinear inversion is linearized to iteratively solve for corrections to the current model. We first discretize the region into a $1^\circ \times 1^\circ$ grid, and do the inversion starting from a uniform model estimated from Crustal2.0 (Laske et al., 2001). The results are then used to calculate an updated uniform starting model for a second inversion, which is on a $0.5^\circ \times 0.5^\circ$ grid (Fig. 4). In addition to a uniform starting model, we also test a starting model with patterns

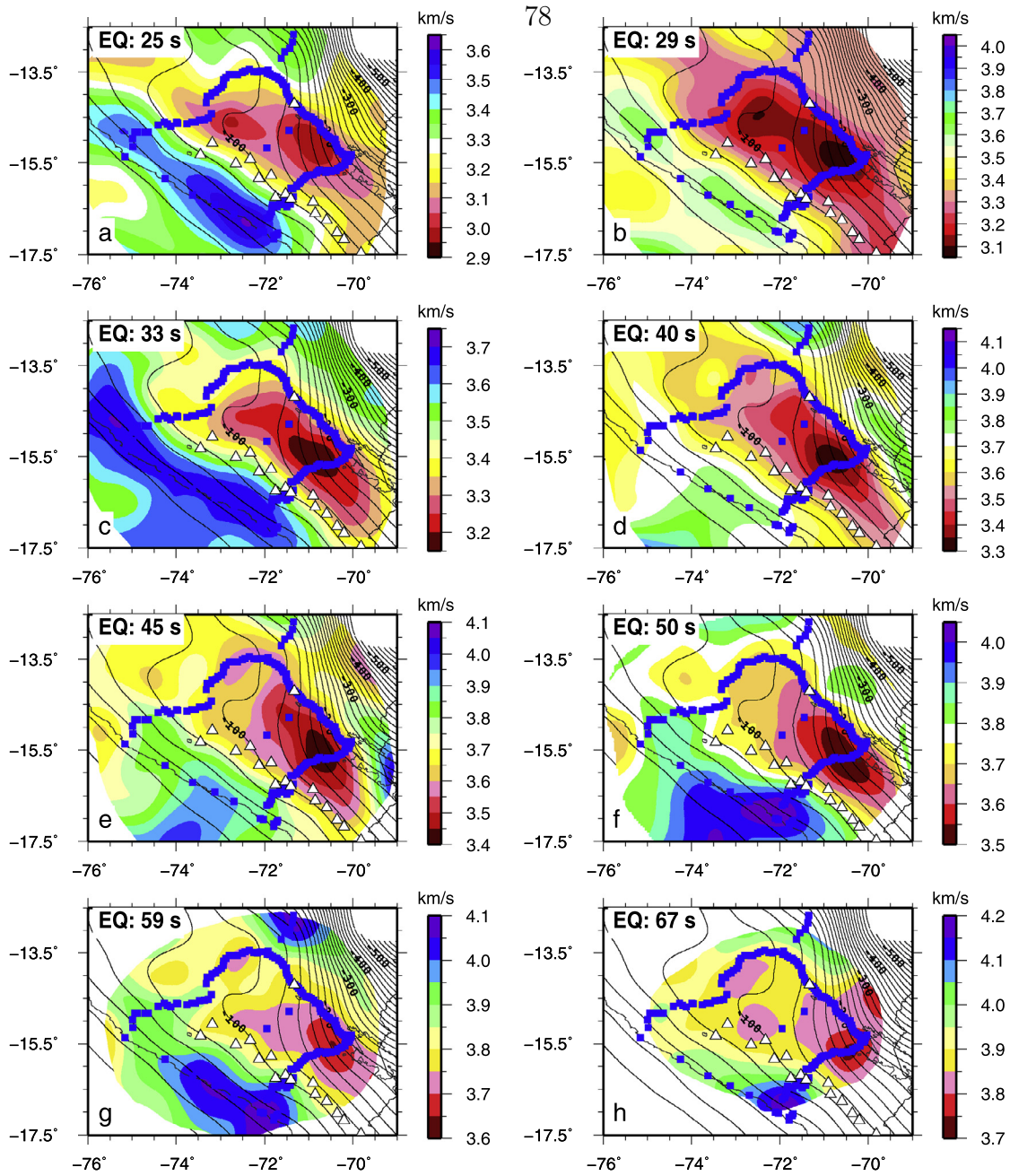


Fig. 4. Two-plane-wave phase velocity maps from 25 s to 67 s period. The results are clipped with model error less than 10% of the average velocity in each period.

from the results of $1^\circ \times 1^\circ$ inversion. The main features are consistent, and hence the initial model does not affect the shear wave inversion results discussed in the following section.

The model resolution and model covariance matrices obtained in the last iteration is used to evaluate the model standard error (Supplementary Fig. 3). Since we solve for the perturbation Δm to the current model in each iteration, the error and resolution is that of Δm . However, if we assume in the $(n-1)$ th iteration, the resulted model m_{n-1} is close enough to the global optimum, which means there is no error associated with the starting model in the n th iteration, then the error and resolution of Δm represents that of m_n . If the iteration converges to a local optimum, then the error can be underestimated, but as addressed above, we tested two starting models to check the consistency. We also check the consistency between the ambient noise and the earthquake surface wave results at the overlap period of 25 s (Supplementary Fig. 3e).

We see that the difference is generally less than 0.05 km/s inside of the box array, but is larger outside of the box where we do not have good resolution for both methods. The earthquake result is possibly more reliable outside of the box since it reflects the rapid change in topography (Fig. 1). Nevertheless, we use the average of the results from the two methods at 25 s.

2.3. Inversion for shear velocity structure

With the phase velocity maps, we are able to extract the phase velocities from 6 to 67 s period at each location. The 1-D shear velocity structure at each location is inverted from the estimated dispersion curve using the linearized inversion algorithm by Herrmann and Ammon (2004). These 1-D profiles are then combined to form a 3-D structure of the whole region.

For each 1-D inversion, we invert for a smooth model without a Moho discontinuity because the surface waves are not very

sensitive to discontinuities, and also we do not have a direct estimate of Moho depth inside of the “box” array. The effects of not imposing a Moho in the inversion will be addressed later. The crustal thicknesses (Fig. 5) and Poisson’s ratio beneath the four lines of the array, which are around the edge of the “box”, were previously determined from receiver function studies (Phillips and Clayton, 2014; Phillips et al., 2012). Although the V_p/V_s ratio measured by the receiver function analysis is only for the crust, we use the average values of 1.76 for the forearc and 1.75 for the backarc (Phillips and Clayton, 2014; Phillips et al., 2012) for the whole depth during the inversions. We found that the surface wave inversion is not very sensitive to the particular choice of V_p/V_s ratio.

We initially invert for the average structures of the forearc and backarc regions separately (Fig. 6). We define the 3.35 km/s con-

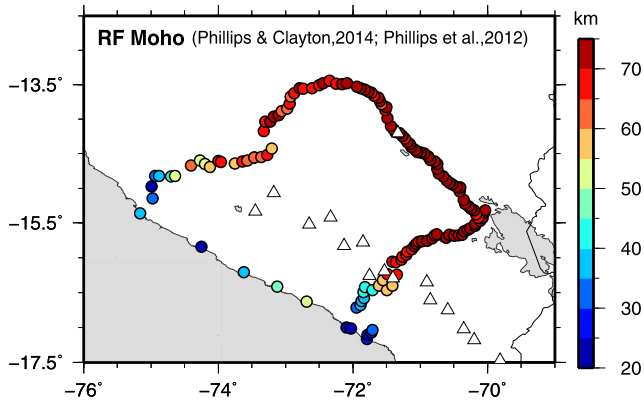


Fig. 5. The Moho depth from receiver functions (Phillips and Clayton, 2014; Phillips et al., 2012).

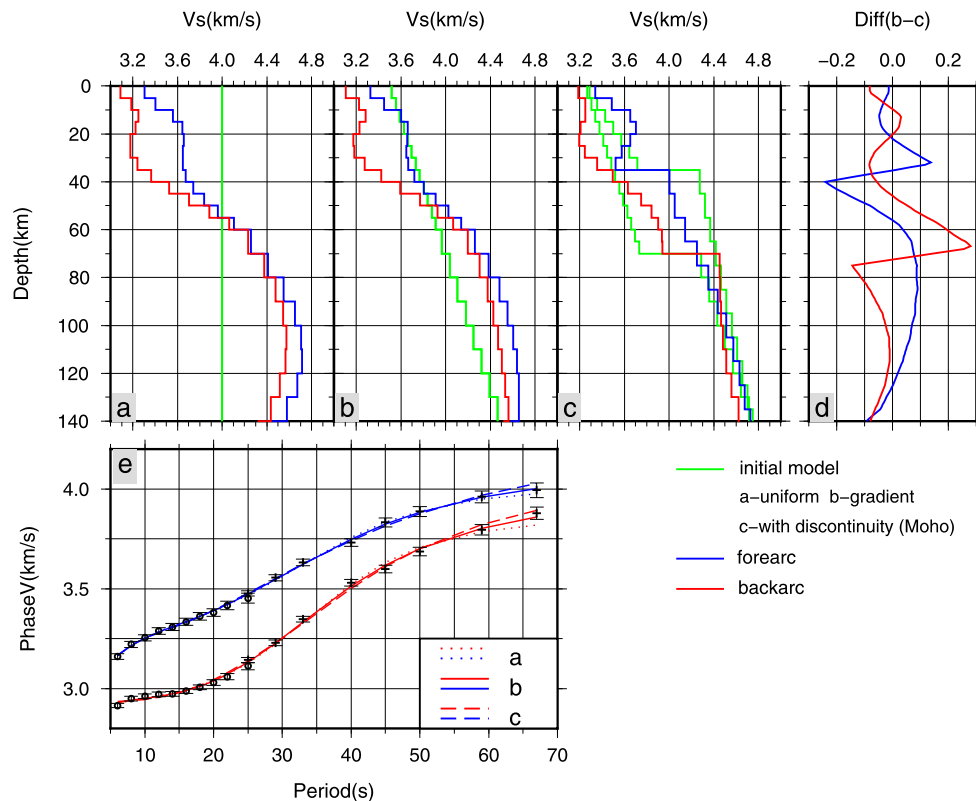


Fig. 6. (a–c) Inversion results from different starting models. The green lines are the starting models. The blue and red lines are inversion results for the forearc and backarc regions respectively. (d) The difference between the results in Panels b and c. (e) Average dispersion curves for the forearc and backarc regions respectively. The data are plotted with error bars, and the predictions are from the inversion results in Panels a–c. (For interpretation of the references to color in this figure legend, the reader is referred to the web version of this article.)

tour⁷⁹ in the 25 s phase velocity map (Fig. 4a) as the boundary between the two regions. The top 60 km is discretized into 5 km layers, and then 10 km layers to 140 km depth. We also tested the case with the combination of 10 km and 20 km layer thicknesses with no significant differences in the results. Two smooth starting models (Fig. 6a–b) were tested. One is a uniform model of 4 km/s, the other is a model linearly increasing from 3.5 km/s at 0 km to 4.5 km/s at 140 km depth. The damping parameter is chosen as 0.5, from the trade-off curve of the misfit and model smoothness (Hansen, 1992), and the density is fixed at 3 kg/m³. The inversion as shown in Fig. 6a–b is stable under the two starting models, except for the velocities from below 120 km depth. From the dispersion curves predicted by the two starting models (Fig. 6e), we see that the linear-gradient initial model (model b) has a better fit at 67 s period. This suggests that the uniform initial model with 4 km/s is too slow at greater depths implying that the inversion is trapped in a local minimum, and hence the linear-gradient initial model is preferred. The average structures for the forearc and backarc regions (Fig. 6b) are then used as starting models for the inversions with finer x–y grids. A damping parameter of 1.0 is used in the results shown here, although other values are also tested. Several depth slices are shown in Fig. 7.

To show the effects of Moho on the inversion results, in Fig. 6c, we also tested a case with a velocity discontinuity in the initial model. The depth of the discontinuity corresponds to the average Moho depth of the forearc and backarc region estimated from the receiver function studies (Fig. 5). We see that with equivalent misfit to the dispersion curves (Fig. 6e), significant differences (>0.05 km/s) exist in the velocities of the lower crust and upper mantle between the two inversion results with or without a Moho (Fig. 6d). Nevertheless, the smoothed model is determined by the true velocities of the lower crust and upper mantle, and therefore

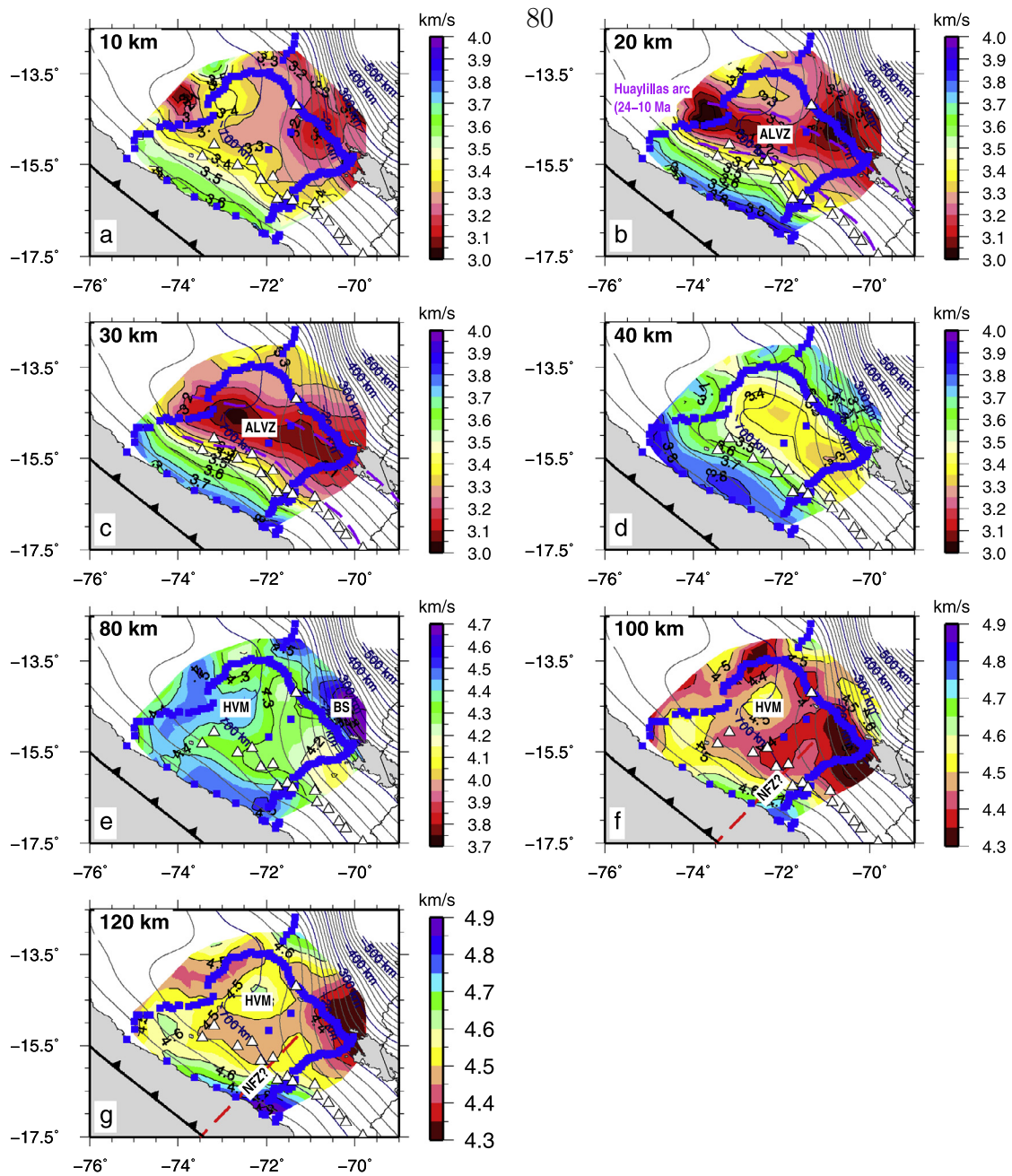


Fig. 7. The depth slices of the shear wave velocity structure from 10 km to 120 km depth. ALVZ: the Andean Low-Velocity Zone; HVM: the High Velocity Mantle above the flat slab; BS: the Brazilian Shield; NFZ: the Nazca Fracture Zone.

the velocity contrasts among the smooth models in each location do reflect the first order features and will be discussed in the next section.

3. Results and discussions

3.1. The mid-crust structure

A mid-crust low-velocity zone is shown clearly in the 20 km and 30 km depth slices (“ALVZ” in Fig. 7b–c). From the cross-sections (Fig. 8), we see that the low-velocity zone extends from 20 km to about 35 km depth. We can also observe this structure directly from 10–25 s phase velocity maps (Figs. 3b–d, 4a).

Interestingly, the low-velocity zone is oblique to the trench, and does not coincide with the present volcanism. Instead, the location and shape of it coincides well with the extent of the Huayllillas

arc (24–10 Ma) in Mamani et al. (2010), as shown in Fig. 7b–c. We identify it as part of the Andean low-velocity zone, which has been imaged by the receiver function study in the latitude range of 20°S–26°S (Yuan et al., 2000). Although the amplitude and thickness of this low-velocity zone varies with location, our results match the structure profile at 24°S, and is explained as the partially molten rocks in the crust. The crustal melting is also characterized by high seismic attenuation, reduced seismic velocity, and high conductivity as shown in several other seismic and magnetotelluric and geomagnetic deep-sounding experiments in the Central Andes (Schilling et al., 2006). The macroscopic properties, such as elasticity and conductivity, depend not only on the volume fraction of the melt (liquid), but also on the microscopic geometry of the liquid phase (Hashin and Shtrikman, 1962; Takei, 1998). On the assumption that the melts form an ideally interconnected network, the observed electrical conductivity pro-

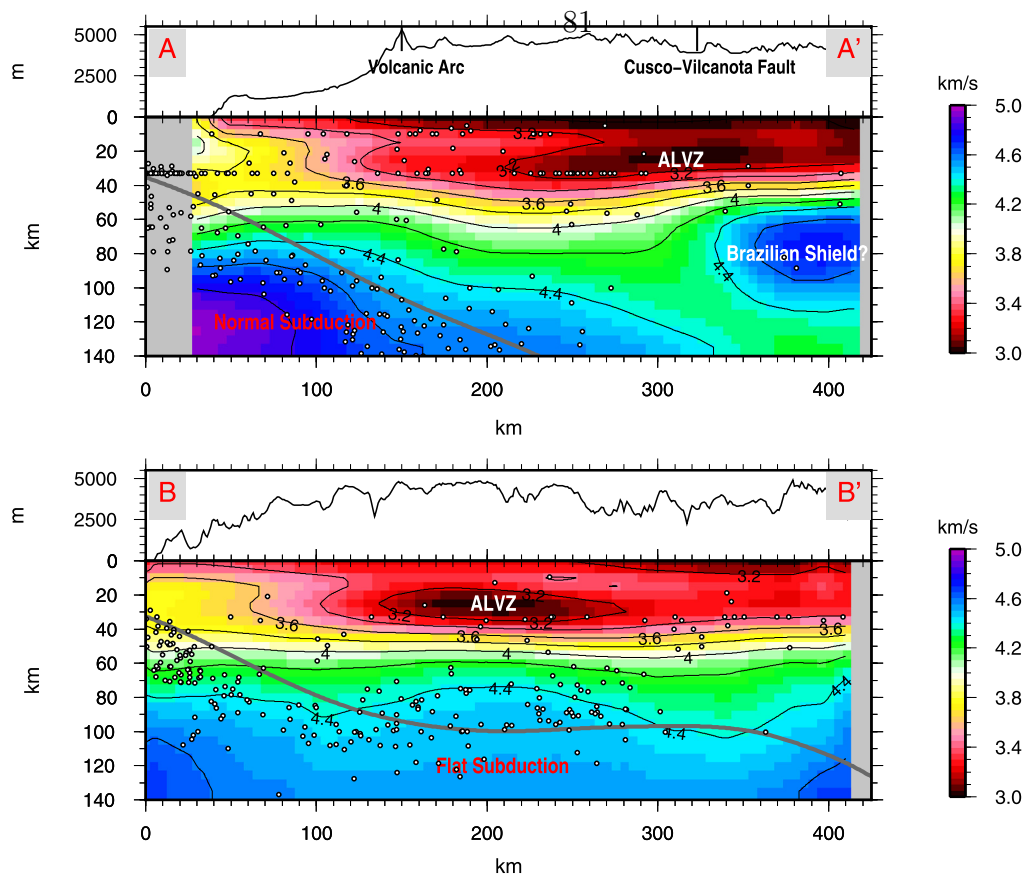


Fig. 8. The shear wave velocity structure along A–A' and B–B' profiles in Fig. 1. The earthquakes are from NEIC catalog (1976/01–2013/09), and those within ± 60 km are projected to the profile. The slab1.0 model (<http://earthquake.usgs.gov/research/data/slab>) is plotted in dark gray lines.

vides a minimum estimation of the proportion of melts to be 14–27 vol.% (Schilling et al., 2006). In order to do the estimation from the shear wave velocity results, we need to understand the dependence of shear wave velocity on the temperature and distribution of the melts.

Because of the correlation between the ALVZ and the surface exposure of the volcanic rocks, Yuan et al. (2000) suggest that this feature is most probably caused by mantle magmatism and heat advection related to subduction, lithospheric mantle delamination and intracrustal diapirism. As suggested in Kay and Coira (2009) and Ramos and Folguera (2009), the steepening of the Oligocene flat slab beneath the Altiplano plateau and the early Miocene flat slab beneath the Puna plateau can lead to the continuous mantle and crustal melting that produced widespread volcanism (including large ignimbrites) in the Central Andes. The magmatic addition from the mantle, although is not significant to the crustal thickening compared with the tectonic shortening (Allmendinger et al., 1997), contributes heat, which induces the crustal melting and lowers the viscosity of the mid-lower crust, and therefore controls the mechanical behavior of the crust. For example, the low velocity zone can be a channel for the crustal flow, which is a proposed mechanism for thickening the Altiplano crust (Husson and Sempere, 2003). The low-velocity zone we observed probably delineates the arcs formed during the steepening of the ancient Altiplano flat slab, and hence maps the geometry of the ancient flat slab at its northern end.

3.2. The slab velocity

The age of the subducted Nazca slab at the trench is about 50 Ma (Müller et al., 2008), and therefore the thickness of it is estimated to be 80 km from the Pacific model in Zhang and

Lay (1999). With the slab contours which delineate the top of the oceanic lithosphere, we can estimate that the bottom of the oceanic lithosphere changes from 80 km depth in the trench to 180 km depth beneath the volcanic arc. From the depth slices of 100 and 120 km in Fig. 7, we observe a decrease in the slab velocity from SE to NW in the forearc region. This feature is also evident in the 100 km depth slice of a larger scale surface wave tomography of South America (Feng et al., 2007). The decrease in the shear wave velocity of the slab towards the flat subduction regime coincides with the thinning of the effective elastic thickness (T_e) (Pérez-Gussinyé et al., 2008). Although the age of the slab decreases northwards along the trench (Fig. 1), and shear velocity of the slab generally increases with the age, the difference in the age is not sufficient to explain the velocity difference according to the age-velocity relations (Stein and Stein, 1992; Zhang and Lay, 1999). There is also a velocity contrast, which is clearest in the 120 km depth slice, seemingly indicates the trace of the Nazca fracture zone (Fig. 7g). Again, the age difference of ~ 5 Myrs across the fracture zone (Fig. 1) is not sufficient to explain this contrast. The general decrease in the slab velocity northward along the coast appears to be related to the serpentinization during the formation of the Nazca Ridge. Fractures formed during the formation of the Nazca ridge as a hotspot trace (Pilger and Handschumacher, 1981) enable the hydration and serpentinization of the upper mantle of the slab, which lowers the slab velocity. This effect is expected to decrease away from the ridge, which agrees with our observations. The hydration of the slab would provide more buoyancy compared with that of a thickened crust in a ridge (Porter et al., 2012). This study does not extend far enough to the north to address the interesting question of why the slab remains flat after the passage of the Nazca Ridge.

3.3. The mantle above the slab

In the 80–120 km depth slices of Fig. 7, the cold oceanic lithosphere is shown as high velocity in the forearc. We also see a high velocity feature in the mantle above the flat slab (“HVM” in Fig. 7e–g), near the sharp-bending of the slab contours. In local studies of the Pampean flat subduction regime, similar phenomenon is also observed by both body wave (Wagner et al., 2005) and surface wave tomography (Porter et al., 2012). In the area at 72.5°W/13.5°S, where the slab inside of the array is flattest, the velocity is similar as the normal subduction regime, which is possibly due to some local structure. The existence of a comparatively high shear wave velocity mantle above the flat slab indicates a cold environment and the lack of melting, which explains the cessation of the volcanism above it.

3.4. The underthrusting Brazilian shield

We observe a velocity contrast across the PF line, which coincides with the Cusco–Vilcanota Fault System (Fig. 1). A higher velocity block is located to the northeast, and is most prominent in the depth range of 40–100 km (Fig. 7). We note that, because the resolution outside of the “box” array is from the earthquake two-plane-wave method which starts from 25 s, we do not have resolution outside of the “box” shallower than around 30 km depth. Therefore, it’s possible that the velocity contrast exists even in the shallow depths. From the cross-section of the normal subduction area (Fig. 8), we see the high velocity is most evident in the uppermost mantle depth. The amplitude of this anomaly in the flat subduction regime is, however, much weaker compared with that in the normal subduction regime (Fig. 7e).

The velocity contrast across the Cusco–Vilcanota Fault System delineates two lithospheric blocks, which is also evident in the geochemical index of mafic rocks (Carlier et al., 2005). The high velocity mantle below the crust of the Eastern Altiplano–Eastern Cordillera is similar as the structure in Bolivia, where it is interpreted as the underthrusting of the Brazilian lithosphere (Beck and Zandt, 2002; Dorbath et al., 1993; Myers et al., 1998). Particularly, the study of Dorbath et al. (1993) to the south of Lake Titicaca, also imaged a velocity contrast, from surface to upper mantle, across a fault near the Lake Titicaca. The underthrusting of the Brazilian shield over time between 19° and 20°S is shown in Fig. 3 in McQuarrie et al. (2005). Our result reveals that the underthrusting Brazilian lithosphere continues northward along the strike. However, since we do not observe a strong velocity anomaly below the Eastern Cordillera in the flat subduction regime, it’s possible that either a collision happened between the oceanic lithosphere and the Brazilian lithosphere, or the Brazilian lithosphere hasn’t reached the northern part of our imaged area.

4. Conclusions

We have imaged the shear wave velocity (V_{SV}) structure of Southern Peru using the surface wave signals from ambient noise cross-correlations and earthquake data. A low-velocity mid-crust structure is imaged, as part of the Andean low-velocity zone. The recently subducted slab below the forearc shows a decrease in velocity from normal to flat subduction regime that appears to be related with the serpentization during the formation of the Nazca ridge. A comparatively high velocity mantle is observed above the flat slab, which indicates the lack of mantle melting and consequently the cessation of volcanism above it. A velocity contrast across the Cusco–Vilcanota Fault System is imaged, which delineates two lithospheric blocks. It indicates the underthrusting of the Brazilian shield beneath the Eastern Cordillera in Southern Peru.

Acknowledgements

We thank Prof. Huajian Yao for providing the ambient noise dispersion measurement code, Prof. Don Forsyth for providing the two-plane-wave tomography code, and Dunzhu Li for useful discussions. We also thank the editor and two anonymous reviewers for their helpful comments. This work is supported by NSF (EAR-1045683) and the Gordon and Betty Moore Foundation through the Tectonics Observatory at Caltech (contribution number 257).

Appendix A. Supplementary material

Supplementary material related to this article can be found online at <http://dx.doi.org/10.1016/j.epsl.2014.03.013>.

References

- Abbott, D., 1991. The case for accretion of the tectosphere by buoyant subduction. *Geophys. Res. Lett.* 18, 585–588.
- Allmendinger, R.W., Jordan, T.E., Kay, S.M., Isacks, B.L., 1997. The evolution of the Altiplano–Puna plateau of the Central Andes. *Annu. Rev. Earth Planet. Sci.* 25, 139–174.
- Aster, R.C., Borchers, B., Thurber, C.H., 2012. *Parameter Estimation and Inverse Problems*. Academic Press.
- Barmin, M.P., Ritzwoller, M.H., Levshin, A.L., 2001. A fast and reliable method for surface wave tomography. *Pure Appl. Geophys.* 158, 1351–1375.
- Beck, S.L., Zandt, G., 2002. The nature of orogenic crust in the central Andes. *J. Geophys. Res.* 107, 2230.
- Bensen, G.D., Ritzwoller, M.H., Barmin, M.P., Levshin, A.L., Lin, F., Moschetti, M.P., Shapiro, N.M., Yang, Y., 2007. Processing seismic ambient noise data to obtain reliable broad-band surface wave dispersion measurements. *Geophys. J. Int.* 169, 1239–1260.
- Brenguier, F., Shapiro, N.M., Campillo, M., Nercessian, A., Ferrazzini, V., 2007. 3-D surface wave tomography of the Piton de la Fournaise volcano using seismic noise correlations. *Geophys. Res. Lett.* 34.
- Carlier, G., Lorand, J., Liégeois, J.-P., Fornari, M., Soler, P., Carlotto, V., Cardenas, J., 2005. Potassic–ultrapotassic mafic rocks delineate two lithospheric mantle blocks beneath the southern Peruvian Altiplano. *Geology* 33, 601–604.
- Cotte, N., Pedersen, H., Campillo, M., Farra, V., Cansi, Y., 2002. Off-great-circle propagation of intermediate-period surface waves observed on a dense array in the French Alps. *Geophys. J. Int.* 142, 825–840.
- Dorbath, C., Granet, M., Poupinet, G., Martinez, C., 1993. A teleseismic study of the Altiplano and the Eastern Cordillera in northern Bolivia: new constraints on a lithospheric model. *J. Geophys. Res., Solid Earth* (1978–2012) 98, 9825–9844.
- Feng, M., Van der Lee, S., Assumpção, M., 2007. Upper mantle structure of South America from joint inversion of waveforms and fundamental mode group velocities of Rayleigh waves. *J. Geophys. Res., Solid Earth* (1978–2012) 112.
- Forsyth, D.W., Li, A., 2005. Array analysis of two-dimensional variations in surface wave phase velocity and azimuthal anisotropy in the presence of multipathing interference. In: *Seismic Earth: Array Analysis of Broadband Seismograms*. AGU, Washington, DC, pp. 81–97.
- Gerya, T.V., Fossati, D., Cantieni, C., Seward, D., 2009. Dynamic effects of aseismic ridge subduction: numerical modelling. *Eur. J. Mineral.* 21, 649–661.
- Gutscher, M.-A., 2002. Andean subduction styles and their effect on thermal structure and interplate coupling. *J. South Am. Earth Sci.* 15, 3–10.
- Gutscher, M.A., Olivet, J.L., Aslanian, D., Eissen, J.P., Maury, R., 1999. The “lost inca plateau”: cause of flat subduction beneath Peru?. *Earth Planet. Sci. Lett.* 171, 335–341.
- Gutscher, M.A., Spakman, W., Bijwaard, H., Engdahl, E.R., 2000. Geodynamics of flat subduction: seismicity and tomographic constraints from the Andean margin. *Tectonics* 19, 814–833.
- Hansen, P.C., 1992. Analysis of discrete ill-posed problems by means of the L-curve. *SIAM Rev.* 34, 561–580.
- Hashin, Z., Shtrikman, S., 1962. A variational approach to the theory of the effective magnetic permeability of multiphase materials. *J. Appl. Phys.* 33, 3125–3131.
- Herrmann, R., Ammon, C., 2004. Surface waves, receiver functions and crustal structure. *Computer Programs in Seismology, Version 3*, 30.
- Husson, L., Sempere, T., 2003. Thickening the Altiplano crust by gravity-driven crustal channel flow. *Geophys. Res. Lett.* 30, 1243.
- Kay, S.M., Coira, B.L., 2009. Shallowing and steepening subduction zones, continental lithospheric loss, magmatism, and crustal flow under the Central Andean Altiplano–Puna Plateau. Backbone of the Americas: shallow subduction, plateau uplift, and ridge and terrane collision 204, 229.

- Laske, G., Masters, G., Reif, C., 2001. CRUST 2.0: a new global crustal model at 2×2 degrees. Institute of Geophysics and Planetary Physics, The University of California, San Diego, website: <http://mahi.ucsd.edu/Gabi/rem.dir/crust/crust2.html>.
- Lin, F.-C., Moschetti, M.P., Ritzwoller, M.H., 2008. Surface wave tomography of the western United States from ambient seismic noise: Rayleigh and Love wave phase velocity maps. *Geophys. J. Int.* 173, 281–298.
- Ma, Y., Clayton, R.W., Tsai, V.C., Zhan, Z., 2013. Locating a scatterer in the active volcanic area of Southern Peru from ambient noise cross-correlation. *Geophys. J. Int.*
- Mamani, M., Wörner, G., Sempere, T., 2010. Geochemical variations in igneous rocks of the Central Andean orocline (^{13}S to ^{18}S): tracing crustal thickening and magma generation through time and space. *Geol. Soc. Am. Bull.* 122, 162–182.
- Manea, V.C., Pérez-Gussinyé, M., Manea, M., 2012. Chilean flat slab subduction controlled by overriding plate thickness and trench rollback. *Geology* 40, 35–38.
- McQuarrie, N., Horton, B.K., Zandt, G., Beck, S., DeCelles, P.G., 2005. Lithospheric evolution of the Andean fold-thrust belt, Bolivia, and the origin of the central Andean plateau. *Tectonophysics* 399, 15–37.
- Müller, R.D., Sdrolias, M., Gaina, C., Roest, W.R., 2008. Age, spreading rates, and spreading asymmetry of the world's ocean crust. *Geochem. Geophys. Geosyst.* 9.
- Myers, S.C., Beck, S., Zandt, G., Wallace, T., 1998. Lithospheric-scale structure across the Bolivian Andes from tomographic images of velocity and attenuation for P and S waves. *J. Geophys. Res., Solid Earth (1978–2012)* 103, 21233–21252.
- Ocola, L.C., Meyer, R.P., 1972. Crustal low-velocity zones under the Peru-Bolivia Altiplano. *Geophys. J. Int.* 30, 199–208.
- O'Driscoll, L.J., Richards, M.A., Humphreys, E.D., 2012. Nazca–South America interactions and the late Eocene–late Oligocene flat-slab episode in the central Andes. *Tectonics* 31.
- Oncken, O., Hindle, D., Kley, J., Elger, K., Victor, P., Schemmann, K., 2006. Deformation of the central Andean upper plate system—facts, fiction, and constraints for plateau models. In: *The Andes*. Springer, pp. 3–27.
- Pérez-Gussinyé, M., Lowry, A., Phipps Morgan, J., Tassara, A., 2008. Effective elastic thickness variations along the Andean margin and their relationship to subduction geometry. *Geochem. Geophys. Geosyst.* 9.
- Phillips, K., Clayton, R.W., 2014. Structure of the subduction transition region from seismic array data in southern Peru. *Geophys. J. Int.* 196, 1889–1905.
- Phillips, K., Clayton, R.W., Davis, P., Tavera, H., Guy, R., Skinner, S., Stubbailo, I., Audin, L., Aguilar, V., 2012. Structure of the subduction system in southern Peru from seismic array data. *J. Geophys. Res., Solid Earth (1978–2012)* 117.
- Pilger, R.H., Handschumacher, D.W., 1981. The fixed-hotspot hypothesis and origin of the Easter–Sala y Gomez–Nazca trace. *Geol. Soc. Am. Bull.* 92, 437–446.
- Porter, R., Gilbert, H., Zandt, G., Beck, S., Warren, L., Calkins, J., Alvarado, P., Anderson, M., 2012. Shear wave velocities in the Pampean flat-slab region from Rayleigh wave tomography: implications for slab and upper mantle hydration. *J. Geophys. Res., Solid Earth (1978–2012)* 117.
- Ramos, V.A., Folguera, A., 2009. Andean flat-slab subduction through time. In: *Special Publications*, vol. 327. Geological Society, London, pp. 31–54.
- Schilling, F.R., Trumbull, R.B., Brasse, H., Haberland, C., Asch, G., Bruhn, D., Mai, K., Haak, V., Giese, P., Muñoz, M., 2006. Partial melting in the Central Andean crust: a review of geophysical, petrophysical, and petrologic evidence. In: *The Andes*. Springer, pp. 459–474.
- Shapiro, N.M., Campillo, M., Stehly, L., Ritzwoller, M.H., 2005. High-resolution surface-wave tomography from ambient seismic noise. *Science* 307, 1615–1618.
- Skinner, S.M., Clayton, R.W., 2013. The lack of correlation between flat slabs and bathymetric impactors in South America. *Earth Planet. Sci. Lett.* 371–372, 1–5.
- Stein, C.A., Stein, S., 1992. A model for the global variation in oceanic depth and heat flow with lithospheric age. *Nature* 359, 123–129.
- Takei, Y., 1998. Constitutive mechanical relations of solid–liquid composites in terms of grain-boundary contiguity. *J. Geophys. Res., Solid Earth (1978–2012)* 103, 18183–18203.
- Wagner, L., Beck, S., Zandt, G., 2005. Upper mantle structure in the south central Chilean subduction zone (30 to 36 S). *J. Geophys. Res.* 110, B01308.
- Ward, K.M., Porter, R.C., Zandt, G., Beck, S.L., Wagner, L.S., Minaya, E., Tavera, H., 2013. Ambient noise tomography across the Central Andes. *Geophys. J. Int.* 194, 1559–1573.
- Yang, Y., Forsyth, D.W., 2006a. Rayleigh wave phase velocities, small-scale convection, and azimuthal anisotropy beneath southern California. *J. Geophys. Res.* 111.
- Yang, Y., Forsyth, D.W., 2006b. Regional tomographic inversion of the amplitude and phase of Rayleigh waves with 2-D sensitivity kernels. *Geophys. J. Int.* 166, 1148–1160.
- Yao, H., van der Hilst, R.D., de Hoop, M.V., 2006. Surface-wave array tomography in SE Tibet from ambient seismic noise and two-station analysis – I. Phase velocity maps. *Geophys. J. Int.* 166, 732–744.
- Yuan, X., Sobolev, S., Kind, R., Oncken, O., Bock, G., Asch, G., Schurr, B., Graeber, F., Rudloff, A., Hanka, W., 2000. Subduction and collision processes in the Central Andes constrained by converted seismic phases. *Nature* 408, 958–961.
- Zhang, Y.-S., Lay, T., 1999. Evolution of oceanic upper mantle structure. *Phys. Earth Planet. Inter.* 114, 71–80.
- Zhou, Y., Dahlen, F., Nolet, G., 2004. Three-dimensional sensitivity kernels for surface wave observables. *Geophys. J. Int.* 158, 142–168.

Supplementary material

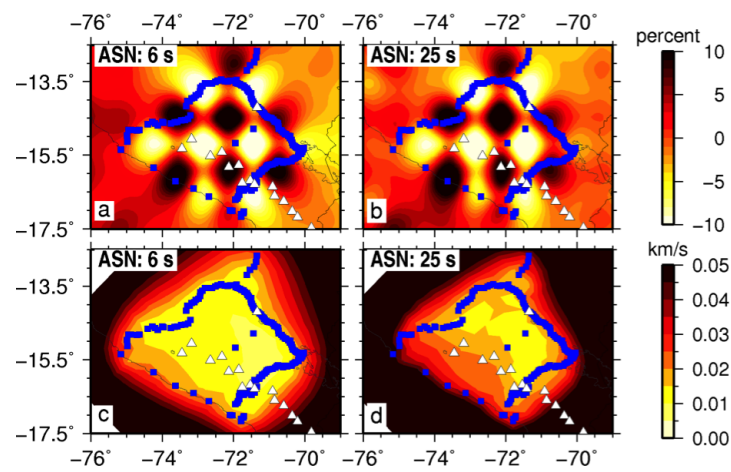


Figure S1: Resolution test and model error of ambient noise tomography estimated from the resolution matrix and model covariance matrix.

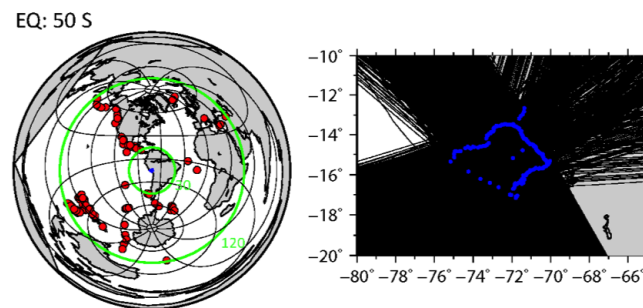


Figure S2: The earthquakes used in the 50 s period two-plane-wave tomography. Also shown is the ray coverage.

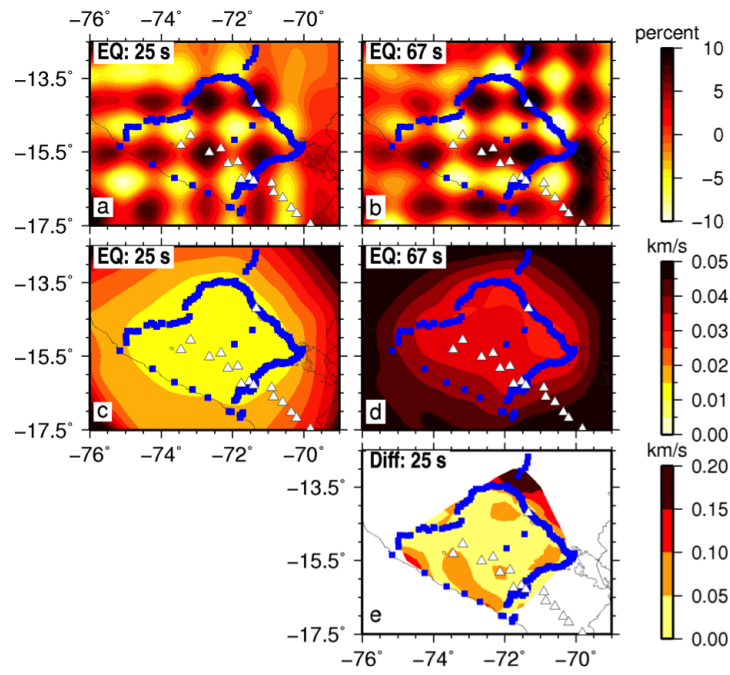
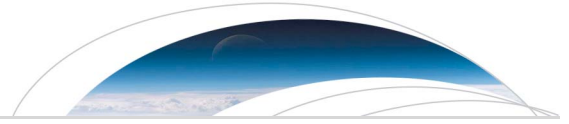


Figure S3: Resolution test and model error of earthquake two-plane-wave tomography estimated from the resolution matrix and model covariance matrix. The difference between the ambient noise and earthquake tomography at 25 s is also plotted.

Chapter 6

Flat slab deformation caused by interplate suction force

1



RESEARCH LETTER

10.1002/2015GL065195

Key Points:

- The flat slab follows the shape of the continental Moho due to the interplate suction force
- The dehydration and eclogitization of the slab is delayed by flat subduction
- Molten rocks and Brazilian Shield are imaged in the crust of Western and Eastern Cordillera

Supporting Information:

- Texts S1 and S2, Figures S1–S6, and Table S1

Correspondence to:

Y. Ma,
yrma@caltech.edu

Citation:

Ma, Y., and R. W. Clayton (2015), Flat slab deformation caused by interplate suction force, *Geophys. Res. Lett.*, *42*, 7064–7072, doi:10.1002/2015GL065195.

Received 1 JUL 2015

Accepted 17 AUG 2015

Accepted article online 20 AUG 2015

Published online 12 SEP 2015

Flat slab deformation caused by interplate suction force

Yiran Ma¹ and Robert W. Clayton¹¹Seismological Laboratory, California Institute of Technology, Pasadena, California, USA

Abstract We image the structure at the southern end of the Peruvian flat subduction zone, using receiver function and surface wave methods. The Nazca slab subducts to ~100 km depth and then remains flat for ~300 km distance before it resumes the dipping subduction. The flat slab closely follows the topography of the continental Moho above, indicating a strong suction force between the slab and the overriding plate. A high-velocity mantle wedge exists above the initial half of the flat slab, and the velocity resumes to normal values before the slab steepens again, indicating the resumption of dehydration and eclogitization. Two prominent midcrust structures are revealed in the 70 km thick crust under the Central Andes: molten rocks beneath the Western Cordillera and the underthrusting Brazilian Shield beneath the Eastern Cordillera.

1. Introduction

The subduction zone along South America includes the longest (along strike) flat slab on Earth (see Figure 1 in *Skinner and Clayton* [2013]). The Peruvian flat slab, which spans over 1500 km long as indicated by a gap in the arc volcanoes [*Ramos and Folguera*, 2009], is especially interesting for investigating the dynamic buoyancy that has flattened the slab. It appears to be tied to the Nazca Ridge, which has migrated southward along the trench from 11°S at the point of initial subduction (at ~11.2 Ma) [*Hampel*, 2002]. Its present location coincides with the southern end of the flat subduction segment. Recent studies indicate that the slab subducts at an 18° angle to about 100 km depth and remains flat for about 300 km before resuming its descent [*Hayes et al.*, 2012; *Phillips and Clayton*, 2014]. Based on the arc volcanoes, various segments of the subduction zone of South America have also experienced flat subduction episodes in the past [*Mamani et al.*, 2010; *Ramos and Folguera*, 2009; *Trumbull et al.*, 2006]. In particular, in Oligocene there was a flat slab beneath the Altiplano plateau that is immediately to the south of the present flat subduction zone considered here [*Mamani et al.*, 2010; *O'Driscoll et al.*, 2012; *Ramos and Folguera*, 2009].

The mechanism that transforms a normal-dipping slab into the flat geometry is not clear. The correlation between flat subduction and the subducting anomalies on the oceanic floor (e.g., Nazca Ridge in Figure 1, and J. Fernandez Ridge for Pampean flat subduction near Chile) suggests that buoyancy provided by the subducted oceanic ridge/plateau causes the flat subduction [*Gutscher*, 2002]. The onset of the Peruvian flat subduction is coincident with the subduction of the Nazca Ridge [*Hampel*, 2002; *Skinner and Clayton*, 2013], but this correlation does not work for all flat slab episodes [*Skinner and Clayton*, 2013]. Moreover, the buoyancy solely provided by thickened oceanic crust is not sufficient [*Gerya et al.*, 2009] and is not as significant compared with the lifting force related to upper plate motion and upper mantle viscosity [*van Hunen et al.*, 2002, 2004]. Therefore, other factors such as the enhanced mantle wedge suction by a thick continental craton near the subduction zone are also suggested to be significant in flattening the slab in South America [*Manea et al.*, 2012; *O'Driscoll et al.*, 2012]. The change in distance to the cratonic root, which controls the interplate suction force, is suggested to have caused the flatten and re steepen of the Oligocene flat slab beneath the Altiplano [*O'Driscoll et al.*, 2012].

Distinguishing between the structure of flat and normal subduction zones is important for understanding the mechanisms as well as consequences of the flat subduction. With the recent deployments of seismic arrays, several studies have emerged on the structure in southern Peru where the slab transitions from normal subduction in the southeast to flat subduction in the northwest [*Dougherty and Clayton*, 2014; *Ma and Clayton*, 2014; *Phillips and Clayton*, 2014; *Phillips et al.*, 2012]. The flat subduction zone structure to the north is being investigated by several studies [*Antonijevic et al.*, 2015; *Bishop et al.*, 2013; *Eakin et al.*, 2015].

In this study, we focus on the southernmost Peruvian flat subduction zone, through detailed images of the structures of the oceanic Moho (slab), the continental Moho, and midcrust structures obtained with receiver function and surface wave tomography methods. In particular, we show that the shape of the flat

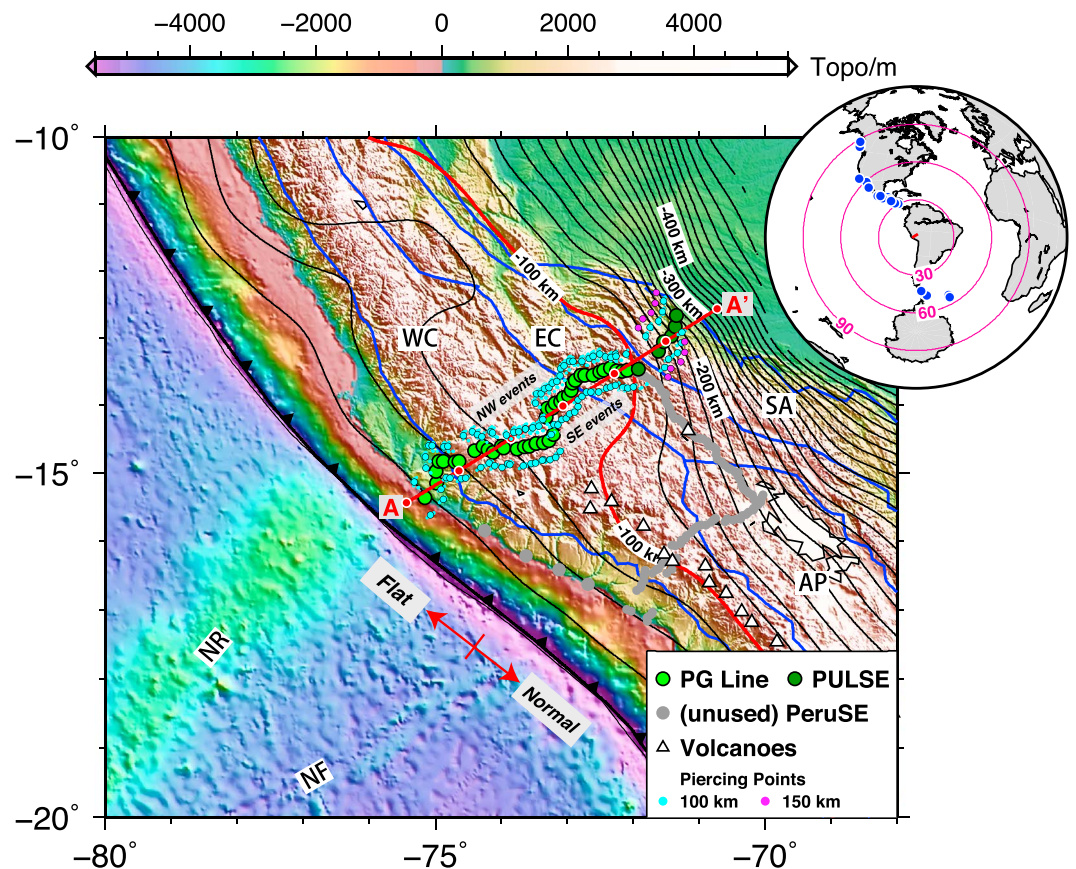


Figure 1. Location of the seismic stations (green dots) used in this study. The grey dots are stations of PeruSE experiment that are not used. A-A' is the projection line of the stations, with 100 km intervals marked with red dots. The main units building the Central Andes are delineated with blue lines (modified from *Oncken et al.* [2006] and *Tassara* [2005]). WC: Western Cordillera; EC: Eastern Cordillera; AP: Altiplano Plateau; and SA: Sub-Andean Ranges. The Holocene volcanoes are denoted with white triangles (data from <http://www.volcano.si.edu/world>). The seafloor features are the Nazca Ridge (NR) and the Nazca Fracture Zone (NF). Slab contours (data from <http://earthquake.usgs.gov/data/slab>) are plotted at 25 km intervals. The 100 km depth slab contour is highlighted with a thick red line, which shows the change of the slab geometry. The top right insert figure shows the teleseismic events used in the receiver function study. The piercing points at 100 km depth are shown in cyan dots in the map, falling into NW and SE events groups. For each station, the centers of the two groups of piercing points are also shown in cyan dots (with black edge). For PULSE stations, we also show piercing points at 150 km depth as pink dots.

slab correlates with the topography of the Moho, which shows the importance of the interplate suction force in the development of flat subduction. Also, a better velocity model is obtained from the surface wave inversion by using velocity discontinuities controlled by the receiver functions. A lateral velocity contrast in the mantle wedge that was first shown in *Ma and Clayton* [2014] is evidence of a delayed dehydration of the flat slab.

2. Data and Results

The data we use are primarily from a dense line of seismic stations (PG line) above the flat subduction regime, which is part of a box-like array (PeruSE) in southern Peru [PeruSE, 2013]. This line includes 40 stations, and was operational from November 2010 to March 2013. We also use six stations (FS stations) from the PULSE experiment [Bishop et al., 2013; Eakin et al., 2014]. The array has an interstation spacing of approximately 10 km and spans from the coast to the sub-Andean region, where the flat slab resumes a normal-dipping geometry (Figure 1).

2.1. Ps Receiver Functions

We use iterative time-domain deconvolution [Kikuchi and Kanamori, 1982; Ligorria and Ammon, 1999] to retrieve P-to-S receiver functions (RFs). A low-pass Gaussian filter is applied with a parameter of 1.5 (the corresponding

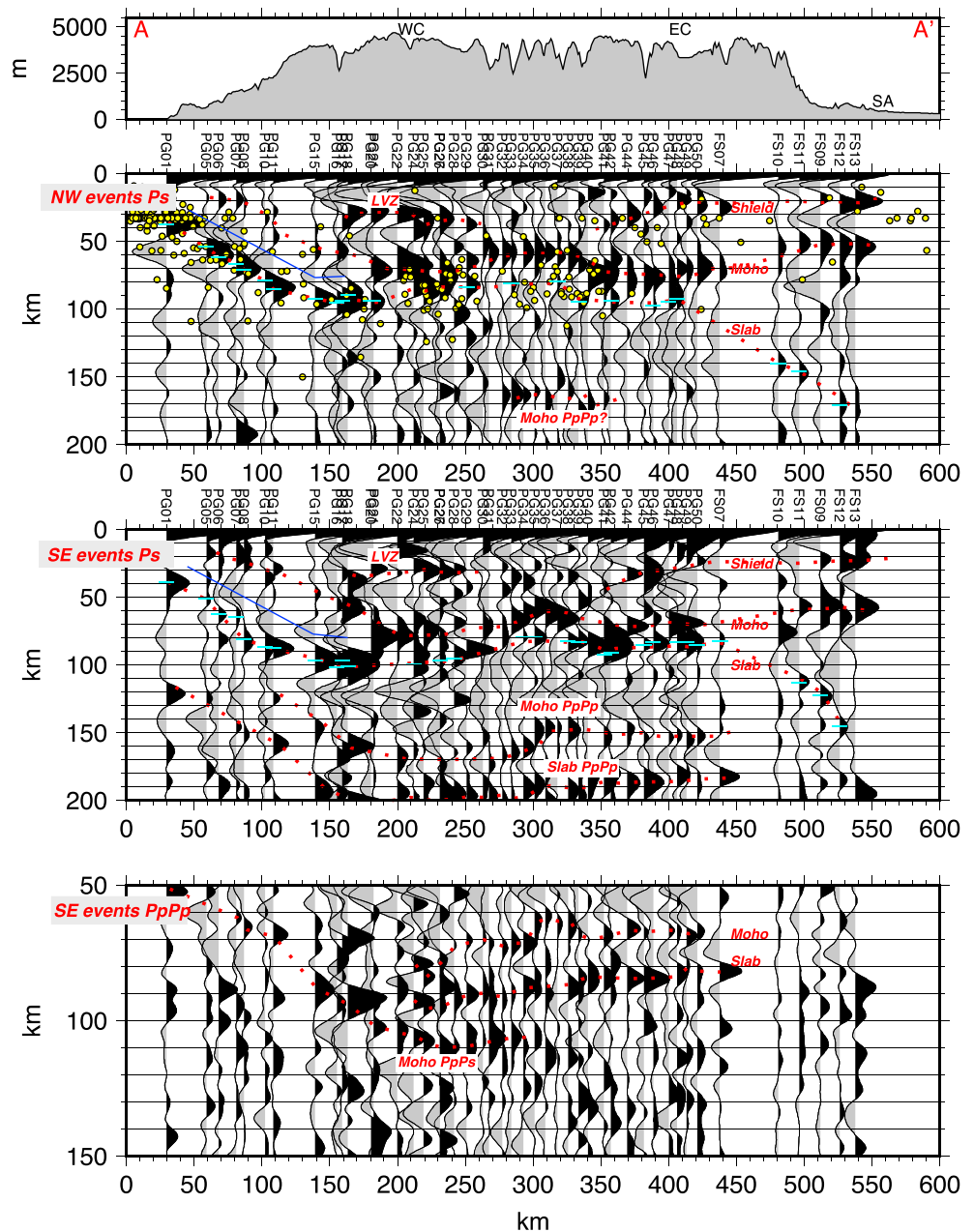


Figure 2. Stacked RFs for each station projected along A-A' profile (Figure 1). Events from NW and SE back azimuths are plotted in separate panels. First and second panels are for P_s RFs. Third panel is for $PpPp$ RFs (see texts for details). The yellow dots are earthquakes from the National Earthquake Information Center catalog (from 1980 to November 2014), with magnitude not less than 4, and within ± 60 km from the profile. The density of the seismicity is better illustrated in Figure S4, which shows two clusters centered at 225 and 325 km distance. The red dotted lines delineate the speculated structures. The negative signals corresponding to the conversion at the top of the slab are marked with blue lines. The cyan dashes are picked slab depths shown in Figure 3b.

cutoff frequency and the pulse width in time domain are approximately 0.7 Hz and 1.36 s, respectively). Figure 1 shows the events used, all of which have a magnitude larger than 5.9 and an epicentral distance in the range of 29–86° (Table S1 in the supporting information). The events are dominantly from NW and SE azimuths, and accordingly their piercing points are separated into two groups as shown in Figure 1. Since there are noticeable along-strike variations in the structure, we show the RFs from the stack of the two groups of events separately in Figure 2. Before the stacking, the IASP91 model [Kennett and Engdahl, 1991] is used as the reference to transform the time axis of the RFs (Figure S1) to depth, using the depth-time relation for the P_s phase. Since the

events are coming from the along-strike direction, we did not apply any correction for the dipping slab. In Figure 2, we show the converted phases associated with the Moho, slab, and the midcrustal structures.

The Moho is ~70 km deep beneath the Western and Eastern Cordillera and rises to ~60 km in the region between the two. The Moho signal is much weaker in the forearc region, indicating a smaller velocity contrast between the uppermost mantle and the crust. In the midcrust beneath the Western Cordillera, there are strong positive and negative signals, which indicate the bottom and the top of a low-velocity zone (LVZ), respectively. Beneath Eastern Cordillera and sub-Andean region, we observe a strong positive signal with an inclined geometry that coincides with increased crustal seismicity. We interpreted it as the top interface of the underthrusting Brazilian Shield, whose existence beneath the Eastern Cordillera is widely recognized [Lamb *et al.*, 1996; McQuarrie *et al.*, 2005; Phillips and Clayton, 2014; Phillips *et al.*, 2012].

In the NW events profile (Figure 2), the slab signals (the P_s conversion at the oceanic Moho) are strong from the coast (PG01) to the initial 50 km of the flattened slab (PG15-PG21) at 95 km depth. The positive signals are then contaminated by strong negative multiples from the midcrust LVZ beneath stations PG22-PG27 (200–230 km distance range in A-A'). Further inland, the flat slab signal does not appear continuously at every station and we pick the slab signal according to its lateral consistency among stations and the seismicity shown by the yellow dots. In the SE events profile, the flat slab signal is more continuous. The flat slab starts at ~100 km depth and shallows to ~80 km depth inland. This trend is magnified with the slab multiples ($PpPp$) which will be discussed in the following section. Further inland, the resteepeened slab imaged by the SE events is ~30 km shallower compared to the NW events profile due to the different geometry of the slab sampled by the two azimuths (see piercing points at 150 km depth in Figure 1).

The depth of the Moho can be controlled to some degree by the V_p/V_s ratio used for the time to depth conversion, with the relationship being approximately $\Delta H = -74.3 \Delta(V_p/V_s)$ (see Text S1 for details), where V_p/V_s is the average for the entire ~60 km thick crust. However, we will see that the observed lateral variations in the Moho geometry cannot be accounted by the V_p/V_s ratio. Since we do not observe any anomalous crustal structure above the up-bulged Moho, we may assume the crustal V_p/V_s there to be 1.75, an average value from previous study [Phillips and Clayton, 2014]. To eliminate the bulge in the Moho would require V_p/V_s to be ~1.88 for the Eastern Cordillera, and ~1.88/2.0 (larger in SE events profile) for the Western Cordillera. These values are extreme and disagree with the observations on the V_p/V_s ratios in the study area [Phillips and Clayton, 2014; Phillips *et al.*, 2012]. A decreasing V_p/V_s inland, in order to remove the shallowing trend in Moho/slab, is also not observed [Phillips and Clayton, 2014].

2.2. $PpPp$ Receiver Functions

In addition to the standard P_s converted phase, we also observe a strong and positive $PpPp$ phase in the SE events profile (Figures S1 and 2). Because the P wave reflection at the free surface changes polarity, the $PpPp$ phase is generally negative in RFs for an interface with positive impedance contrast (downward) such as the Moho. However, with a dipping interface, it can be positive for the events coming from the downdip direction (e.g., Linkimer *et al.* [2010], see Text S2 for more details). This is the case with the SE events because the slab is dipping toward the SE direction near the transition from flat to normal subduction (Figure 1). The dip angle is evident in the cross sections of seismicity parallel to the trench and is estimated to increase from ~10° at ~250 km from the trench to ~20° at ~450 km from the trench (Figure S4 of Dougherty and Clayton [2014]).

The $PpPp$ image (also converted to depth with IASP91 model) clearly shows that the Moho and slab are shallowing inland, which is also evident in the P_s phase but more pronounced with $PpPp$. In addition, an up-bulged Moho is imaged at 310 km distance. An increase in dip angle or P wave velocity inland, for which we have no detailed models, could also cause an apparent shallowing. However, the similarities in depths and lateral changes in the interfaces between P_s and $PpPp$ images give us the confidence that the IASP91 model [Kennett and Engdahl, 1991] we used is appropriate to do the time to depth conversion.

2.3. Shear Wave (V_{SV}) Velocity

We show the shear wave velocity (V_{SV}) structure along the same profile (A-A' in Figure 1) in Figure 3, which is determined from the Rayleigh wave dispersion curves (6–67 s period) retrieved from ambient noise and earthquake data that were previously reported in Ma and Clayton [2014]. In Ma and Clayton [2014], we inverted for smooth 1-D structures at each location inside of the box-like array from the dispersion curves using a reference

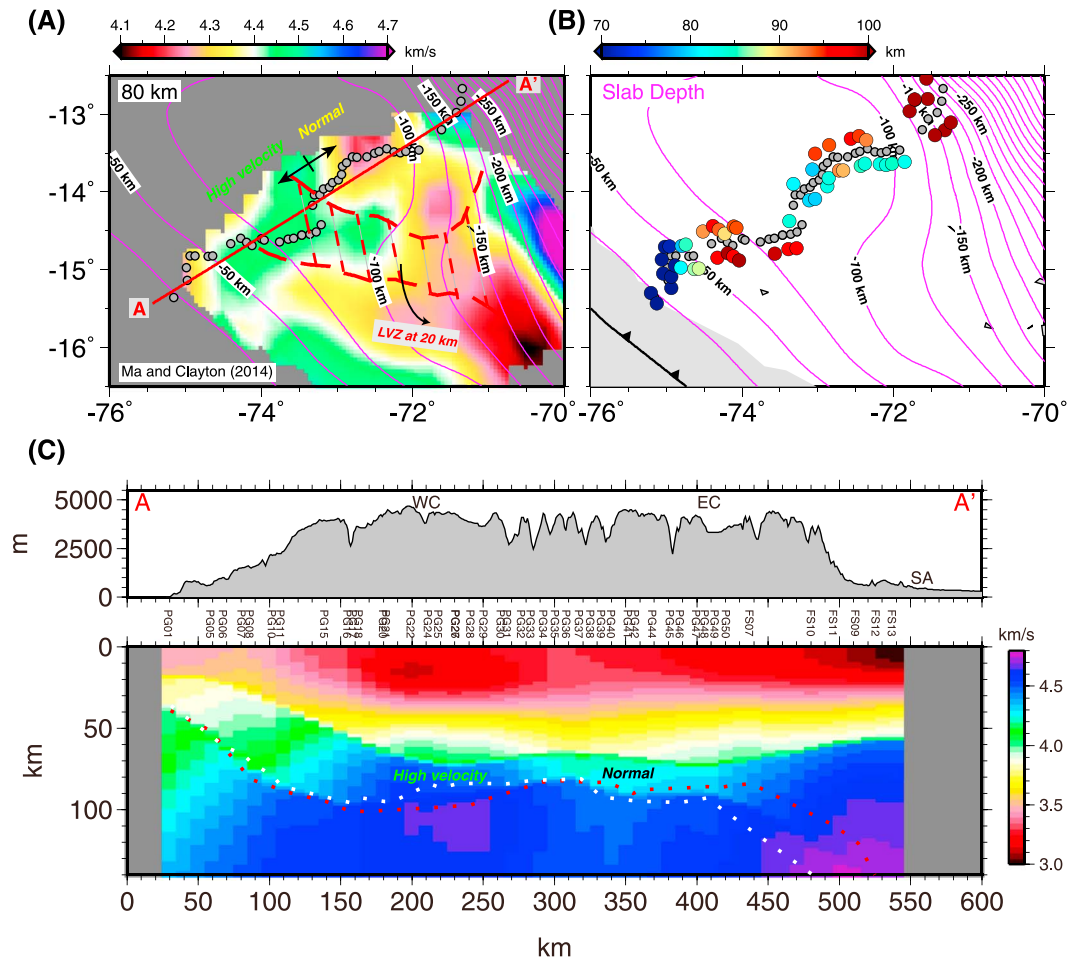


Figure 3. (a) The depth-slice of V_{SV} structure at 80 km depth from *Ma and Clayton* [2014]. Note the contrast between the high and normal velocity mantle. We also plot the extent of the upper-midcrust low-velocity zone (LVZ) on top of it. The boundary of the LVZ is from the 3.2 km/s velocity contour in 20 km depth slice in *Ma and Clayton* [2014]. (b) Depth of the Nazca slab. The data points correspond to the cyan dashes in Figure 2. Pink contours are Slab1.0 model [*Hayes et al.*, 2012]. (c) Shear wave velocity structure inverted from Rayleigh wave dispersion (6–67 s period). The white and red dotted lines are the slab depths from RFs (NW and SE events, respectively) in Figure 2.

model without velocity discontinuities. To improve the velocity estimates along the array of stations used in this study, we use the depths of Moho and slab determined from the RFs (averaged from NW and SE events, and laterally smoothed). We add velocity discontinuities at the depths of the two interfaces in the initial model (Figure S5) and impose less damping across them during the inversion. The initial model is a simple three-layer model with V_s of 3.5 km/s for the crust, 4.3 km/s for the mantle wedge, and 4.5 km/s below the mantle wedge (Figure S5). We discretize the model into 2 km fine layers above 200 km depth for the inversion, and the result is shown in Figure 3c. To confirm the pattern in the mantle, we also discretized the top 50 km of the crust into 2 km layers, while treating the rest of the crust, the mantle wedge, and the slab (assumed to be 80 km thick) as single layers (Figure S5b), and the result (Figure S6) is comparable to Figure 3c.

In the distance range of ~260–420 km (Figure 3), the mantle wedge shows a comparatively lower velocity distinct from the first half (150–260 km) of the flat slab segment, which is characterized by high velocity. The horizontal extent of this high-velocity mantle wedge is shown in Figure 3a, which is a depth slice at 80 km depth from *Ma and Clayton* [2014]. The low velocity may indicate the resumption of the dehydration of the slab before it resumes the normal-dipping subduction. The low velocity extends in depth through the entire oceanic lithosphere, which can be partly due to the smearing effect of the inversion. Alternatively, the oceanic lithosphere may indeed have a low-velocity upper mantle due to the formation of the Nazca ridge, whose subducted portion may cover a larger area than its onshore projection into our study area [*Hampel*, 2002].

3. Discussion

The results of the paper show that beneath the over 4 km high Central Andes, there are two prominent crustal features—the low-velocity zone beneath the Western Cordillera and the Brazilian Shield beneath the Eastern Cordillera. The Nazca slab is not uniformly flat and tends to follow the topography of the Moho.

3.1. The Andean Low-Velocity Zone

The low-velocity zone beneath the Western Cordillera is shown in both RFs and surface wave results (Figures 2 and 3c). The low-velocity zone is shown in 10–25 km depth range from surface wave (Figure 3c) and 15–30 km depth from RFs (Figure 2). The discrepancy may be due to that the V_p/V_s ratio used in migrating the RFs is smaller than reality [Zhu and Kanamori, 2000]. This zone was previously mapped in this region [Ma and Clayton, 2014]. It is oblique to the present trench (Figure 3a) and is suggested to be molten rocks related to the volcanism during the steepening of the Oligocene flat slab beneath the Altiplano plateau [Ma and Clayton, 2014]. This low-velocity zone, as part of the Andean low-velocity zone, widely exists in the crust of the Central Andes [Schilling *et al.*, 2006; Ward *et al.*, 2013; Yuan *et al.*, 2000] and can be the channel for the crustal flow which is important in building the high and flat plateau [Husson and Sempere, 2003; Yang *et al.*, 2003]. However, despite of the apparent large volume of the low-velocity zone, this does not indicate that the mantle-derived melts add significantly to thickening the crust. From the compositions of the ignimbrites, only minor andesitic melts (from the mantle) are thought to contribute to this low-velocity zone, while the melting of the crust itself is the dominant component [Mamani *et al.*, 2010; Schilling *et al.*, 2006].

3.2. The Brazilian Shield

The extent of the underthrusting Brazilian Shield beneath the Eastern Cordillera has previously been determined from the mantle structure [Beck and Zandt, 2002; Dorbath *et al.*, 1993; Myers *et al.*, 1998]. Recently, Phillips *et al.* [2012] and Phillips and Clayton [2014] have imaged the top of it as positive receiver function signals in the midcrust and suggested that the shield has reached further west and exists beneath the Altiplano. Our result better defines the shape of the top of the shield as a thrust fault, as was delineated in Lamb *et al.* [1996] based on unpublished oil company data. It is also delineated by the seismicity (yellow dots in Figure 2). A similar image of the underthrusting Indian shield beneath the Himalayas is shown in Schulte-Pelkum *et al.* [2005] and Nelson *et al.* [1996]. The shield appears to be absent from the upper mantle structure beneath the Eastern Cordillera because the mantle of the Brazilian Shield lithosphere is likely to have been largely removed in this region by the slab [O'Driscoll *et al.*, 2012]. The mantle beneath the sub-Andean shows a high-velocity zone, which we interpret as the shield lithosphere.

3.3. The Slab

The dipping slab in the forearc region shows strong signals, with positive and negative pulses delineating the bottom and the top interfaces of the oceanic crust, respectively. From the amplitude of those signals, Kim and Clayton [2015] determined the seismic and mineralogical properties of the oceanic crust. They found that compared with the normal subduction segment, an additional 20% reduction in V_s exists in the low-velocity layer near the top of the slab, indicating a more fluid-rich layer. Because of the strong hydration of the mantle wedge by the fluids from the slab, the continental Moho signal is weak as the velocity contrast across it is small.

The flat slab signals are not consistently observable in the NW events profile. This is not a problem with the stations, because strong continental Moho signals are observed from this azimuth. The continuous dehydration of the oceanic crust can lead to diminishing slab signals with depth [Kawakatsu and Watada, 2007], but this may not be the reason for here since the SE events profile shows strong and consistent slab signals in both primary and multiple phases. We note that the piercing points of the NW events are close to the trajectory of the Nazca Ridge (Figure 1); hence, scattering by the ridge or the hydration and faulting of the crust and uppermost mantle of the oceanic lithosphere during the formation of the ridge may have weakened the slab signals for these events.

The slab becomes flat at ~100 km depth after subducting approximately 200 km from the trench (at 150 km distance in A-A' profile), which is ~20 km deeper compared with the Slab1.0 model [Hayes *et al.*, 2012] (Figure 3b). Instead of remaining flat or shallowly dipping down, the slab rises afterward and closely follows the shape of the Moho. In the contact region between the Western and Eastern Cordillera, the Moho warps upward and the flat slab follows this trend (Figure 2) along with the seismicity (Figure S1 of Dougherty and Clayton [2014]).

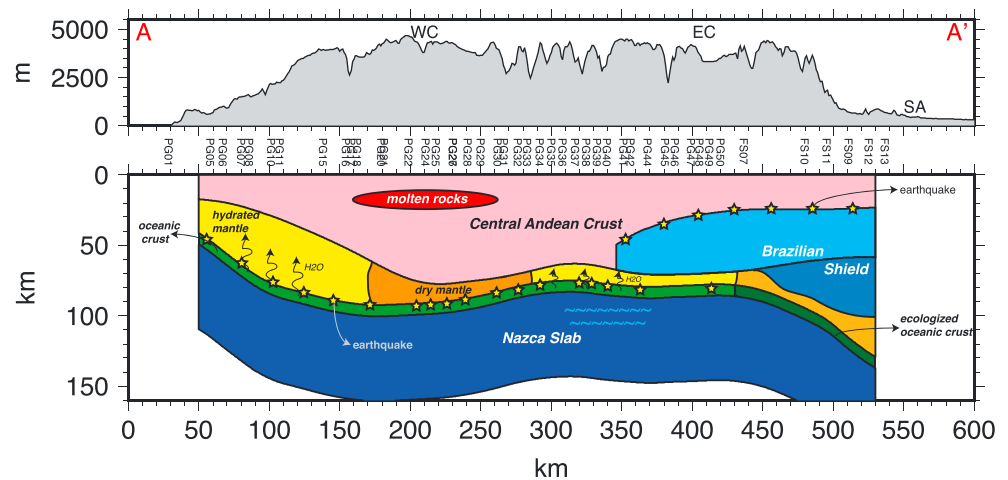


Figure 4. Sketch of the structure imaged in this study. The continental and oceanic Moho depths, as well as the top of the Brazilian Shield are based on the SE events profile in Figure 2. The low-velocity zone and mantle wedge velocity contrast are based on Figure 3. The slab lithosphere is assumed to be 80 km thick with an 8 km thick crust. We illustrate the parallel deformation of the slab and the continental Moho above, which indicates a strong suction force between them. The dehydration process is delayed by the flat subduction, and the complete of the dehydration and eclogitization is reflected in the diminishing seismicity.

The seismicity seems to form two clusters centered at 225 km and 325 km distance (Figure S4), where the largest lateral deformation of the slab occurs.

The shape of the flat slab is probably related to the interplate suction force, which can be very large for the flattened slab [Tovish *et al.*, 1978]. The mantle is pulled out of the wedge by the subducting slab, and with a small dip angle of the slab, insufficient mantle flows into the wedge, leading to a large negative pressure that further decreases the dip angle of the slab. However, we note that there needs to be some mechanism to raise the slab over some critical angle as in Tovish *et al.* [1978], before the negative pressure can flatten the slab by itself. At angles steeper than the critical angle, the inflow is efficient in decreasing the negative pressure and restoring the slab back to a normal geometry, so that the system is in equilibrium. The subduction of the Nazca Ridge may be the factor that pushes the system beyond the critical angle. This process is much easier with a thick crust and nearby lithospheric root, which obstructs the inflow, and hence enhances the suction force as suggested in O'Driscoll *et al.* [2012].

The initial half (close to the trench) of the flat slab is associated with a high-velocity mantle, which gradually disappears along the slab. The extent of the high velocity is shown in Figure 3a, which is a similar pattern shown to the V_s body wave tomography (Figures 13 and 14 in Young [2014]). The high V_s mantle above the flat slab is also observed in the body wave tomography in the Pampean flat subduction zone in Chile, and is associated with relatively low V_p/V_s ratio which indicates a cold and dry environment [Marot *et al.*, 2014; Wagner *et al.*, 2005]. The disappearance of the high-velocity mantle wedge above the flat slab indicates that the slab resumes the dehydration and eclogitization before it steepens again. The eclogitization of the oceanic crust, as is characterized by the vanishing intermediate-depth earthquakes that are due to the dehydration embrittlement [Jung *et al.*, 2004], may cause the resteeptening of the slab beneath sub-Andean.

4. Conclusions

We use a dense linear array to image the structure in the southernmost Peruvian flat subduction zone with receiver functions and surface wave methods. The results are synthesized in Figure 4. The over 4 km high topography of the Central Andes is supported by ~70 km thick crust. An approximately 15 km thick low-velocity zone interpreted as molten rocks is imaged in the upper crust beneath the Western Cordillera. The top of the Brazilian Shield is imaged as a thrust fault beneath the whole Eastern Cordillera. A 10 km shallower Moho is imaged beneath the contact region of the Western and Eastern Cordillera.

The Nazca slab subducts to ~100 km depth and then remains flat for ~300 km distance before it resumes normal subduction. The flat part of the slab closely follows the topography of the continental Moho above,

indicating a strong interplate suction force. The velocity of the upper mantle above the flat slab is comparatively high, indicating a dry and cold environment. The dehydration and eclogitization resumes at 350 km from the trench above the flat slab and lasts for about 100 km until the slab steepens again.

Acknowledgments

The PeruSE experiment was supported by the Gordon and Betty Moore Foundation and NSF (EAR-1045683), and the data used are available through IRIS. We thank Lara Wagner and other members of the PULSE experiment for providing data from six stations. We also thank the Editor and reviewers for constructive comments. The script files necessary to reproduce the results are available from the authors upon request.

The Editor thanks Leland O'Driscoll and an anonymous reviewer for their assistance in evaluating this paper.

References

- Antonijevic, S. K., L. S. Wagner, A. Kumar, S. L. Beck, M. D. Long, G. Zandt, H. Tavera, and C. Condori (2015), The role of ridges in the formation and longevity of flat slabs, *Nature*, *524*(7564), 212–215.
- Beck, S. L., and G. Zandt (2002), The nature of orogenic crust in the central Andes, *J. Geophys. Res.*, *107*(B10), 2230, doi:10.1029/2000JB000124.
- Bishop, B., S. Beck, G. Zandt, A. Kumar, L. Wagner, M. Long, and H. Tavera (2013), Receiver function study of the Peruvian flat-slab region: Initial results from PULSE, paper presented at AGU Fall Meeting Abstracts.
- Dorbath, C., M. Granet, G. Poupinet, and C. Martinez (1993), A teleseismic study of the Altiplano and the Eastern Cordillera in northern Bolivia: New constraints on a lithospheric model, *J. Geophys. Res.*, *98*(B6), 9825–9844, doi:10.1029/92JB02406.
- Dougherty, S. L., and R. W. Clayton (2014), Seismic structure in southern Peru: Evidence for a smooth contortion between flat and normal subduction of the Nazca Plate, *Geophys. J. Int.*, *200*(1), 534–555.
- Eakin, C. M., M. D. Long, S. L. Beck, L. S. Wagner, H. Tavera, and C. Condori (2014), Response of the mantle to flat slab evolution: Insights from local S splitting beneath Peru, *Geophys. Res. Lett.*, *41*, 3438–3446, doi:10.1002/2014GL059943.
- Eakin, C. M., M. D. Long, L. S. Wagner, S. L. Beck, and H. Tavera (2015), Upper mantle anisotropy beneath Peru from SKS splitting: Constraints on flat slab dynamics and interaction with the Nazca Ridge, *Earth Planet. Sci. Lett.*, *412*, 152–162.
- Gerya, T. V., D. Fossati, C. Cantieni, and D. Seward (2009), Dynamic effects of aseismic ridge subduction: Numerical modelling, *Eur. J. Mineral.*, *21*(3), 649–661.
- Gutscher, M.-A. (2002), Andean subduction styles and their effect on thermal structure and interplate coupling, *J. South Am. Earth Sci.*, *15*(1), 3–10.
- Hampel, A. (2002), The migration history of the Nazca Ridge along the Peruvian active margin: A re-evaluation, *Earth Planet. Sci. Lett.*, *203*(2), 665–679.
- Hayes, G. P., D. J. Wald, and R. L. Johnson (2012), Slab1.0: A three dimensional model of global subduction zone geometries, *J. Geophys. Res.*, *117*, B01302, doi:10.1029/2011JB008524.
- Husson, L., and T. Sempere (2003), Thickening the Altiplano crust by gravity-driven crustal channel flow, *Geophys. Res. Lett.*, *30*(5), 1243, doi:10.1029/2002GL016877.
- Jung, H., H. W. Green II, and L. F. Dobrzhinetskaya (2004), Intermediate-depth earthquake faulting by dehydration embrittlement with negative volume change, *Nature*, *428*(6982), 545–549.
- Kawakatsu, H., and S. Watada (2007), Seismic evidence for deep-water transportation in the mantle, *Science*, *316*(5830), 1468–1471.
- Kennett, B. N., and E. Engdahl (1991), Traveltimes for global earthquake location and phase identification, *Geophys. J. Int.*, *105*(2), 429–465.
- Kikuchi, M., and H. Kanamori (1982), Inversion of complex body waves, *Bull. Seismol. Soc. Am.*, *72*(2), 491–506.
- Kim, Y., and R. W. Clayton (2015), Seismic properties of the Nazca oceanic crust in southern Peruvian subduction system, *Earth Planet. Sci. Lett.*, doi:10.1016/j.epsl.2015.07.055.
- Lamb, S., L. Hoke, L. Kennan, and J. Dewey (1996), Cenozoic evolution of the Central Andes in Bolivia and northern Chile, *Geol. Soc. London Spec. Publ.*, *121*, 237–264.
- Ligorria, J. P., and C. J. Ammon (1999), Iterative deconvolution and receiver-function estimation, *Bull. Seismol. Soc. Am.*, *89*(5), 1395–1400.
- Linkimer, L., S. L. Beck, S. Y. Schwartz, G. Zandt, and V. Levin (2010), Nature of crustal terranes and the Moho in northern Costa Rica from receiver function analysis, *Geochem. Geophys. Geosyst.*, *11*, Q01S19, doi:10.1029/2009GC002795.
- Ma, Y., and R. W. Clayton (2014), The crust and uppermost mantle structure of Southern Peru from ambient noise and earthquake surface wave analysis, *Earth Planet. Sci. Lett.*, *395*, 61–70.
- Mamani, M., G. Wörner, and T. Sempere (2010), Geochemical variations in igneous rocks of the Central Andean orocline (13 S to 18 S): Tracing crustal thickening and magma generation through time and space, *Geol. Soc. Am. Bull.*, *122*(1–2), 162–182.
- Manea, V. C., M. Pérez-Gussinyé, and M. Manea (2012), Chilean flat slab subduction controlled by overriding plate thickness and trench rollback, *Geology*, *40*(1), 35–38.
- Marot, M., T. Monfret, M. Gerbault, G. Nolet, G. Ranalli, and M. Pardo (2014), Flat versus normal subduction zones: A comparison based on 3-D regional traveltime tomography and petrological modelling of central Chile and western Argentina (29°–35°S), *Geophys. J. Int.*, *199*(3), 1633–1654.
- McQuarrie, N., B. K. Horton, G. Zandt, S. Beck, and P. G. DeCelles (2005), Lithospheric evolution of the Andean fold-thrust belt, Bolivia, and the origin of the central Andean plateau, *Tectonophysics*, *399*(1), 15–37.
- Myers, S. C., S. Beck, G. Zandt, and T. Wallace (1998), Lithospheric-scale structure across the Bolivian Andes from tomographic images of velocity and attenuation for P and S waves, *J. Geophys. Res.*, *103*(B9), 21,233–21,252, doi:10.1029/98JB00956.
- Nelson, K. D., W. Zhao, L. Brown, J. Kuo, J. Che, X. Liu, S. Klemperer, Y. Makovsky, R. Meissner, and J. Mechie (1996), Partially molten middle crust beneath southern Tibet: Synthesis of project INDEPTH results, *Science*, *274*(5293), 1684–1688.
- O'Driscoll, L. J., M. A. Richards, and E. D. Humphreys (2012), Nazca-South America interactions and the late Eocene-late Oligocene flat slab episode in the central Andes, *Tectonics*, *31*, TC2013, doi:10.1029/2011TC003036.
- Oncken, O., D. Hindle, J. Kley, K. Elger, P. Victor, and K. Schemmann (2006), Deformation of the central Andean upper plate system—Facts, fiction, and constraints for plateau models, in *The Andes*, edited by O. Oncken et al., pp. 3–27, Springer, Berlin.
- PeruSE (2013), Peru subduction experiment, *Caltech. Dataset*, doi:10.7909/C3H41PBZ.
- Phillips, K., and R. W. Clayton (2014), Structure of the subduction transition region from seismic array data in southern Peru, *Geophys. J. Int.*, *196*, 1889–1905.
- Phillips, K., R. W. Clayton, P. Davis, H. Tavera, R. Guy, S. Skinner, I. Stubbailo, L. Audin, and V. Aguilar (2012), Structure of the subduction system in southern Peru from seismic array data, *J. Geophys. Res.*, *117*, B11306, doi:10.1029/2012JB009540.
- Ramos, V. A., and A. Folguera (2009), Andean flat-slab subduction through time, *Geol. Soc. London Spec. Publ.*, *327*(1), 31–54.
- Schilling, F. R., R. B. Trumbull, H. Brasse, C. Haberland, G. Asch, D. Bruhn, K. Mai, V. Haak, P. Giese, and M. Muñoz (2006), Partial melting in the Central Andean crust: A review of geophysical, petrophysical, and petrologic evidence, in *The Andes*, edited by O. Oncken et al., pp. 459–474, Springer, Berlin.
- Schulte-Pelkum, V., G. Monsalve, A. Sheehan, M. Pandey, S. Sapkota, R. Bilham, and F. Wu (2005), Imaging the Indian subcontinent beneath the Himalaya, *Nature*, *435*(7046), 1222–1225.

- Skinner, S. M., and R. W. Clayton (2013), The lack of correlation between flat slabs and bathymetric impactors in South America, *Earth Planet. Sci. Lett.*, 371–372, 1–5.
- Tassara, A. (2005), Interaction between the Nazca and South American plates and formation of the Altiplano-Puna plateau: Review of a flexural analysis along the Andean margin (15–34 S), *Tectonophysics*, 399(1), 39–57.
- Tovish, A., G. Schubert, and B. P. Luyendyk (1978), Mantle flow pressure and the angle of subduction: Non Newtonian corner flows, *J. Geophys. Res.*, 83(B12), 5892–5898, doi:10.1029/JB083iB12p05892.
- Trumbull, R. B., U. Riller, O. Oncken, E. Scheuber, K. Munier, and F. Hongn (2006), The time-space distribution of Cenozoic volcanism in the South-Central Andes: A new data compilation and some tectonic implications, in *The Andes*, edited by O. Oncken, pp. 29–43, Springer, Berlin.
- van Hunen, J., A. P. van den Berg, and N. J. Vlaar (2002), The impact of the South American plate motion and the Nazca Ridge subduction on the flat subduction below South Peru, *Geophys. Res. Lett.*, 29(14), 35–31–35–34, doi:10.1029/2001GL014004.
- van Hunen, J., A. P. van den Berg, and N. J. Vlaar (2004), Various mechanisms to induce present-day shallow flat subduction and implications for the younger Earth: A numerical parameter study, *Phys. Earth Planet. Inter.*, 146(1), 179–194.
- Wagner, L., S. Beck, and G. Zandt (2005), Upper mantle structure in the south central Chilean subduction zone (30 to 36 S), *J. Geophys. Res.*, 110, B01308, doi:10.1029/2004JB003238.
- Ward, K. M., R. C. Porter, G. Zandt, S. L. Beck, L. S. Wagner, E. Minaya, and H. Tavera (2013), Ambient noise tomography across the Central Andes, *Geophys. J. Int.*, 194(3), 1559–1573.
- Yang, Y., M. Liu, and S. Stein (2003), A 3-D geodynamic model of lateral crustal flow during Andean mountain building, *Geophys. Res. Lett.*, 30(21), 2093, doi:10.1029/2003GL018308.
- Young, B. E. (2014), Regional body-wave tomography of the Peruvian flat slab, Univ. of North Carolina at Chapel Hill.
- Yuan, X., S. Sobolev, R. Kind, O. Oncken, G. Bock, G. Asch, B. Schurr, F. Graeber, A. Rudloff, and W. Hanka (2000), Subduction and collision processes in the Central Andes constrained by converted seismic phases, *Nature*, 408(6815), 958–961.
- Zhu, L., and H. Kanamori (2000), Moho depth variation in southern California from teleseismic receiver functions, *J. Geophys. Res.*, 105(B2), 2969–2980, doi:10.1029/1999JB900322.



Geophysical Research Letters

Supporting Information for

Flat Slab Deformation Caused by Interplate Suction Force

Yiran Ma and Robert W. Clayton

Seismological Laboratory, California Institute of Technology, Pasadena, CA 91125

Contents of this file

Text S1 to S2
Figures S1 to S6
Tables S1

Introduction

In Table S1, we provide information on the events we used for the receiver functions (RFs). The time-axis RFs are shown in Figure S1. With Figure S2 and Text S1, we derive the relationship between the change in estimated Moho depth and the change in the V_p/V_s ratio used in the reference model to convert P_s arrival time to depth. With Figure S3 and Text S2, we rationalize our observation of positive $PpPp$ phase in the RFs. In Figure S4, we show the density of the seismicity along A-A' profile, in which two clusters are shown, possibly related with the bending of the slab.

Figure S5 shows the initial model we used for the inversion of V_s , as well as the sensitivity kernel of the surface wave phase velocity for this model. In Figure S6, we show the inversion result with much thicker layers in the mantle, to confirm the large-scale features we see with fine-layered model.

Text S1.

P_s arrival time is mostly related with the relative traveltimes of S and P waves above the interface, therefore is more sensitive to V_p/V_s ratio rather than V_p or V_s individually [Zhu and Kanamori, 2000]. Assume a crustal thickness $H = 60$ km, average P wave velocity of the crust $V_p = 6.3$ km/s, ray parameter $p = 0.06$, $V_p/V_s = 1.8$. From formula (2) in Zhu and Kanamori [2000], the P_s arrival time in the receiver function is 7.9 s.

Then, using the same formula as above, we can convert the time to depth with V_p/V_s ratio from 1.7 to 1.9 (Fig. S2), which gives a relationship: $\Delta H = -74.3 \Delta(V_p/V_s)$.

It suggests that if the V_p/V_s ratio in the reference model (for converting time to depth) is 0.067 smaller than reality, the interface will be mapped 5 km deeper. For IASP91 model used in this study, the average V_p/V_s above 60 km depth is 1.76, which will cause 5 km deeper crust, if the actual V_p/V_s ratio in the crust is 1.827, which is possible for the crust with melts [Yuan et al., 2002]. However, we will see it in the text that the lateral variations in the Moho/slab geometry cannot be explained by the V_p/V_s ratio.

Text S2.

Because of the changing of polarity in free surface reflection, $PpPp$ is usually negative in the RFs. For dipping interface, however, if the ray is coming from the down-dip direction, the horizontal propagation direction of the P wave at the receiver can be opposite to that of the incident P wave (Fig. S3). Therefore, with the changing of polarity, we will observe a positive $PpPp$ phase in the R-component RF.

We will see that the conditions to produce a positive $PpPp$ phase in the RFs are easily to satisfy.

Let the dipping angle of the interface θ , the incidence angles with respect to the vertical direction i_1, i_2, i_3 (Fig. S3). Then,

$$i_2 \leq 90^\circ - \theta \quad (1)$$

$$\frac{\sin(i_1 + \theta)}{V_{p1}} = \frac{\sin(i_2 + \theta)}{V_{p2}} \quad (2)$$

From (2), we have

$$i_1 = \sin^{-1} \left(\frac{V_{p1}}{V_{p2}} \sin(i_2 + \theta) \right) - \theta \quad (3)$$

We see that, to make the horizontal propagation direction of the last leg (L_3) of the P wave different from the incidence wave (L_0), we need to make L_3 at least vertical or deviate to the east. Therefore,

$$i_1 \leq 2\theta \quad (4)$$

$$\sin^{-1} \left(\frac{V_{p1}}{V_{p2}} \sin(i_2 + \theta) \right) \leq 3\theta \quad (5)$$

Then, from (1) and (5), the conditions for a positive $PpPp$ phase in RF is:

$$i_2 \leq \begin{cases} 90^\circ - \theta & \theta \geq 30^\circ \\ \sin^{-1} \left(\min \left(\frac{V_{p_2}}{V_{p_1}} \sin 3\theta, 1 \right) \right) - \theta & \theta < 30^\circ \end{cases} \quad (6)$$

Let $V_{p_1} = 6.8$ km/s, $V_{p_2} = 7.7$ km/s, and $i_2 = 27^\circ$, which are reasonable estimates of the velocities across the Moho and the incidence angle of the teleseismic event used in the RFs, a dipping angle larger than 11° can produce positive $PpPp$ phase in the RFs. An increase in the velocity contrast or a decrease in the incidence angle will require less dipping angle to produce a positive phase.

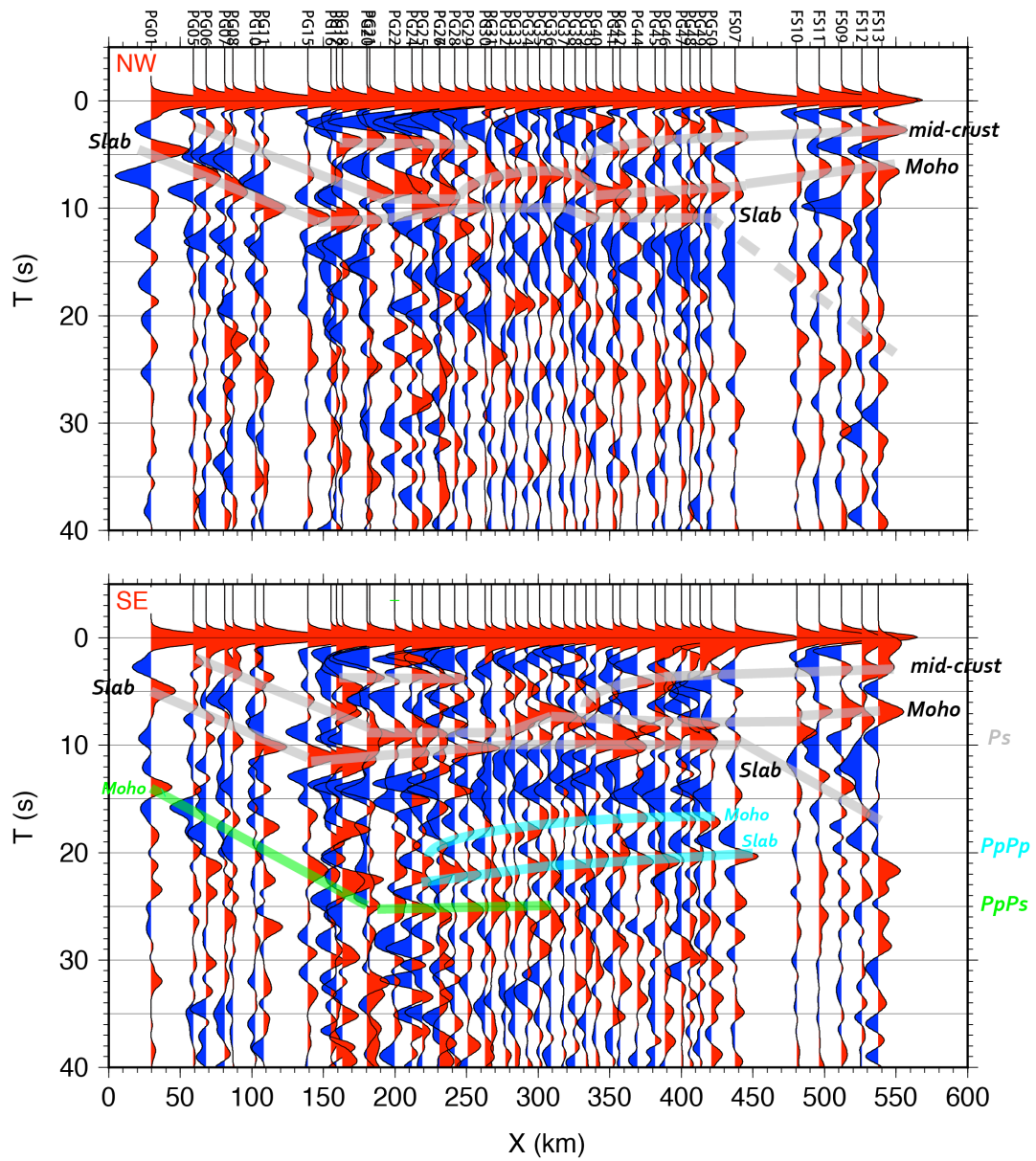


Figure S1. The time-axis RFs stacked for events from NW and SE azimuths separately. The gray lines delineate the P_s phase related with the mid-crust structures, the continental Moho, and the slab (oceanic Moho); the cyan lines in SE profile delineate the $PpPp$ phase related with the Moho and the slab; the green line delineates the $PpPs$ phase related with the Moho.

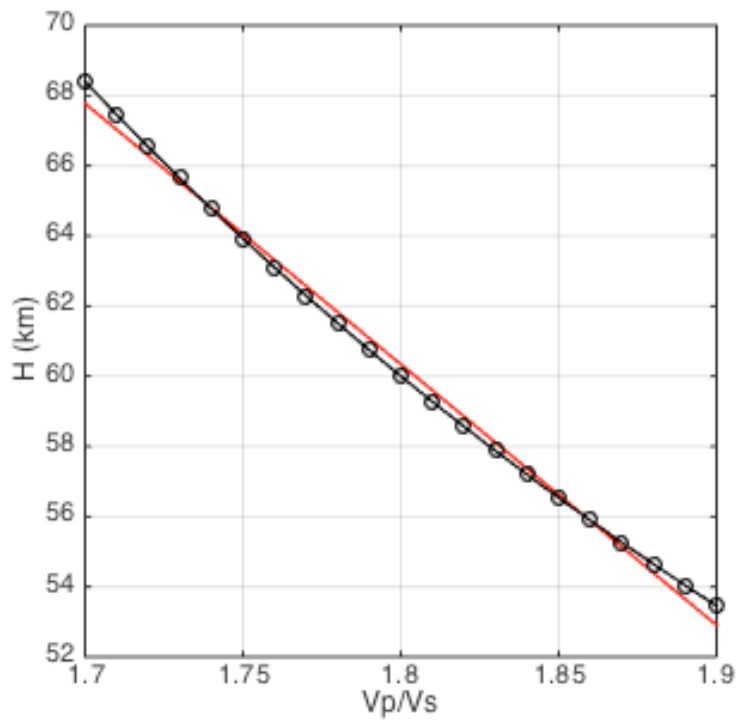


Figure S2. Assume a crustal thickness $H = 60$ km, average P wave velocity of the crust $V_p = 6.3$ km/s, ray parameter $p = 0.06$, $V_p/V_s = 1.8$. We show the resolved depths of the Moho with different V_p/V_s ratios for the time-depth conversion (black line). The red line is a linear-fit to the black line, which gives $\Delta H = -74.3 \Delta(V_p/V_s)$.

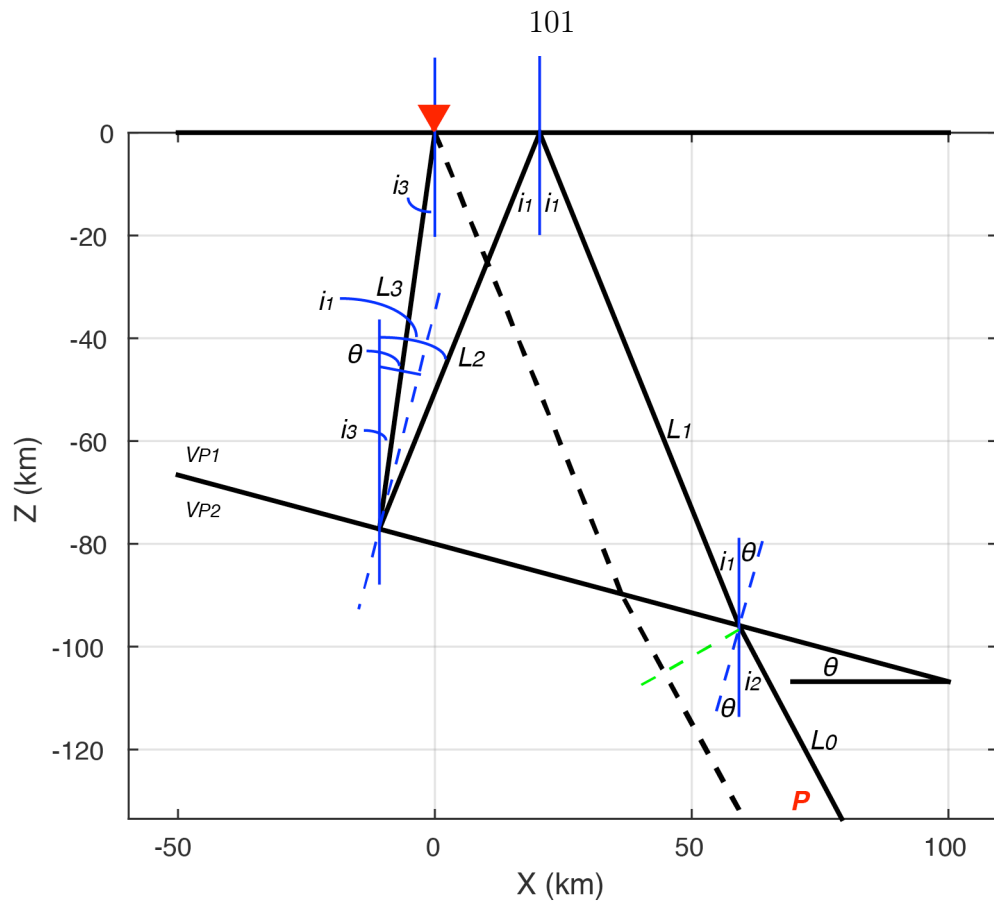


Figure S3. The ray paths of $PpPp$ and direct P (dashed line) for a dipping layered structure. For this model, the depth of the interface beneath the station (red inverted triangle) is 80 km, and the dipping angle θ is 15° . The incident angle of the event (i_2) beneath the interface is 28° . The P wave velocity above and below the interfaces are: $v_{p1} = 6.8$ km/s and $v_{p2} = 7.7$ km/s. The green line marks the wavefront of the P wave before impinging the dipping interface.

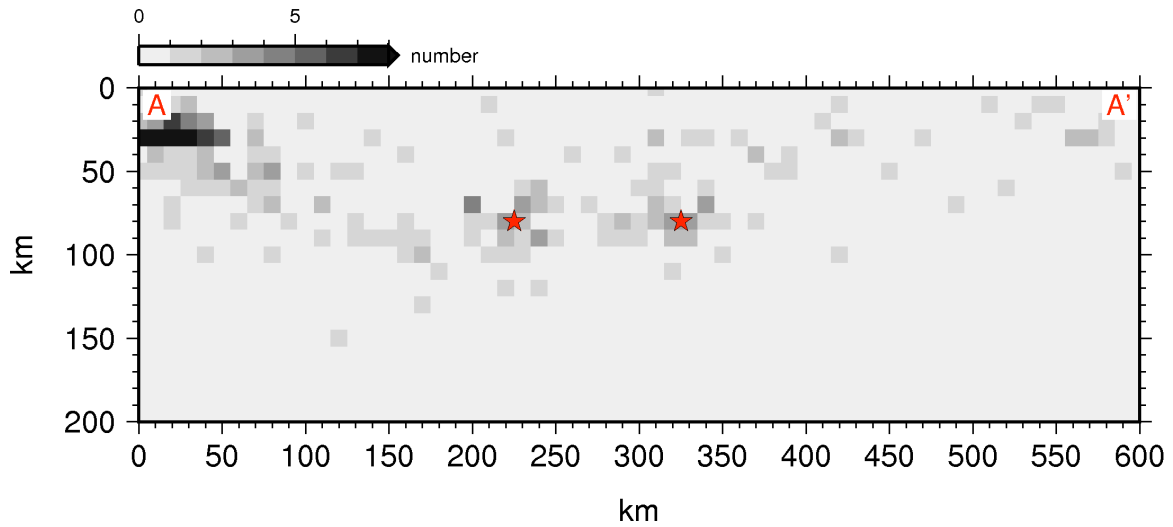


Figure S4. The number of earthquakes in each $10 \times 10 \text{ km}^2$ bins. The earthquake data is the same as the yellow dots in Fig. 2, which is from the NEIC catalog (from 1980 to 2014/11), with magnitude not less than 4, and within $\pm 60 \text{ km}$ from the A-A' projection profile (Fig. 1). The red stars mark the centers of the two clusters at 225 km and 325 km distance.

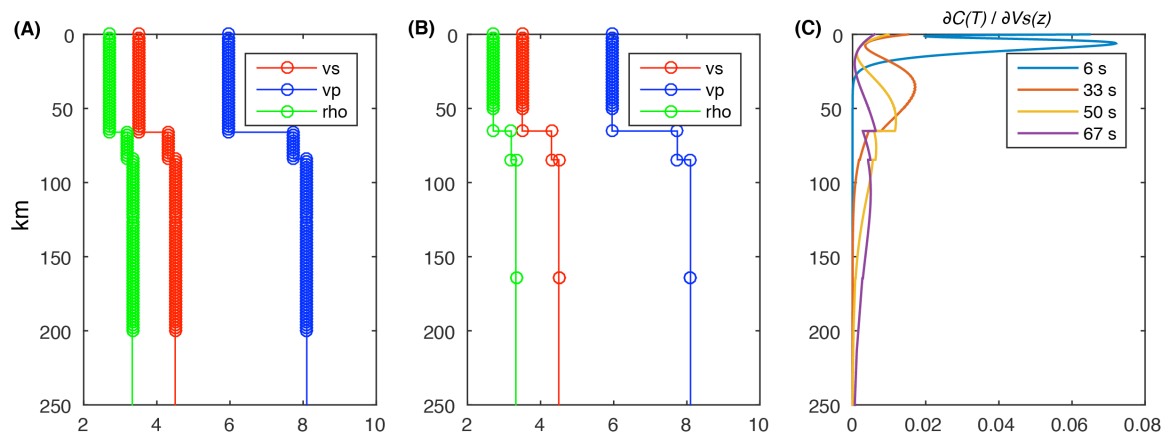


Figure S5. The initial model for the inversion of the 1-D structure at 325 km distance in A-A' profile. In (A), the model is discretized into 2-km layers above 200 km depth, with a half space underneath; in (B), the top 50 km of the crust is discretized into 2-km layers, while the rest of the crust, the mantle wedge and the slab (assumed to be 80 km thick) are treated as single layers. The inversion result with the initial models of (A) type is shown in Fig. 3c, and of (B) type is shown in Fig. S6. In (C), we show the sensitivity of the phase velocity in different period to the shear velocity in different depth.

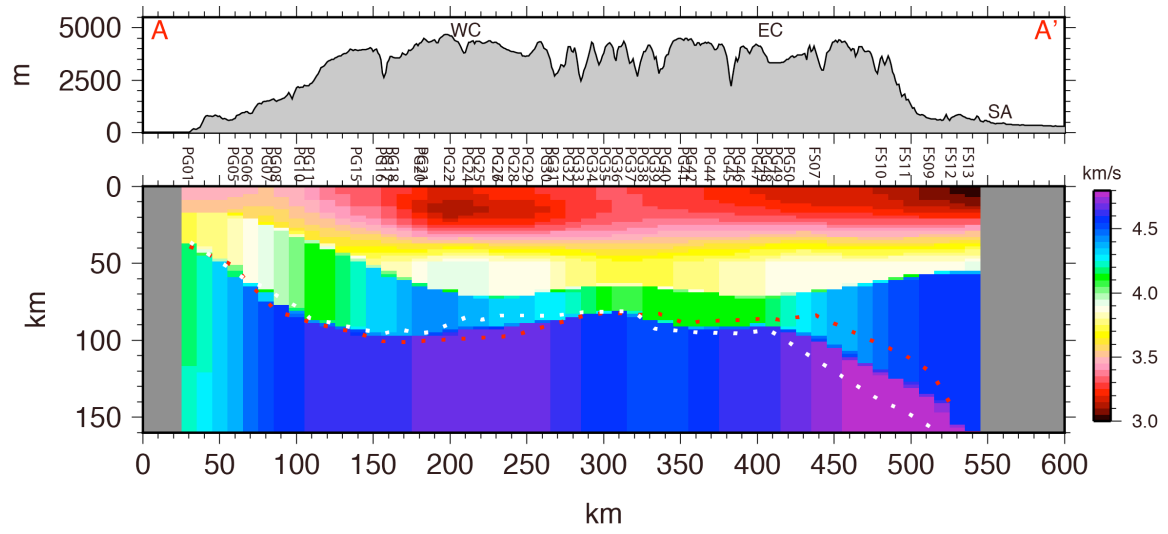


Figure S6. Inversion result with thick upper mantle layer (Fig. S5b), which is comparable to the inversion result on a fine-layered model (Fig. S5a) shown in Fig. 3c.

Time*	Latitude (°)	Longitude (°)	Depth (km)	Magnitude	Back azimuth (°)	Distance (°)
NW events						
20110407131122	17.208	-94.338	166.2	6.6	328.9	37.5
20111107223525	11.56	-85.861	177	6	337.8	28.8
20111211014725	17.844	-99.963	54.2	6.5	322.5	41.1
20120121184711	14.873	-93.005	45	6.2	328.8	34.8
20120320180247	16.493	-98.231	20	7.4	323.3	39.0
20120402173642	16.395	-98.316	9	6	323.1	39.0
20120411225510	18.229	-102.689	20	6.5	319.9	43.0
20120412071548	28.696	-113.104	13	7	320.0	57.1
20120827043719	12.139	-88.59	28	7.3	333.3	30.4
20120925234524	24.666	-110.173	10	6.3	318.2	52.3
20121028030408	52.788	-132.101	14	7.8	329.2	83.7
20121030024902	52.365	-131.902	9	6.2	328.4	83.3
20121107163546	13.963	-91.854	24	7.4	329.6	33.5
20121115092021	18.346	-100.382	53	6.1	321.9	41.4
20121214103601	31.095	-119.66	13	6.3	317.5	62.9
20130105085819	55.394	-134.65	10	7.5	330.5	86.4
SE events						
20101208052435	-56.412	-25.741	29.4	6.3	149.3	55.5
20110306143236	-56.422	-27.063	87.7	6.5	149.7	54.9
20110903044857	-56.451	-26.847	84	6.4	149.8	55.2
20111211095455	-56.009	-28.184	116	6.2	149.5	54.0
20120115134016	-60.975	-56.072	10	5.9	167.5	47.6
20120115134019	-60.948	-56.113	8	6.6	167.5	47.6
20120122055342	-56.759	-25.147	13	6	149.3	55.9
20120414105619	-57.679	-65.308	15	6.2	172.2	42.9
* Time is in the format of YYYYMMDDHHMMSS						

Table S1. Information of the events used in the RFs.

References

- Yuan, X., S. Sobolev, and R. Kind (2002), Moho topography in the central Andes and its geodynamic implications, *Earth and Planetary Science Letters*, 199(3), 389-402.
- Zhu, L., and H. Kanamori (2000), Moho depth variation in southern California from teleseismic receiver functions, *Journal of Geophysical Research*, 105(B2), 2969-2980.

Chapter 7

Conclusions

In Part I, we used data from a dense (~ 1 km spacing) but short duration (~ 1.5 month) array that was deployed across the LA Basin (LASSIE experiment) to image the structure of the basin. With two seismic events, the basement and Moho depths are clearly delineated by the PpPs phase in the receiver functions. The shear velocities are revealed by the Love and Rayleigh waves that emerge in the multi-component cross-correlations.

An elevated Moho is imaged beneath the basin. From the edge to the center of the basin, the basement depth increases from about 3-4 km to about 8 km, and the Moho depth decreases from about 23 km to about 17 km. It indicates a stretch factor increasing from about 1.3 to 2.6, with an estimated initial crustal thickness of 26 km from isostasy. The shear velocity of the sediments increases from about 0.5 km/s to 2 km/s at ~ 2.5 km depth. The gradient rapidly decreases at ~ 4 km depth, indicating that the sediments are fully compacted by this depth. The Newport-Inglewood, Compton-Los Alamitos, and Whittier Faults are all evident from the shear velocity profile.

We show that higher modes are an important component of high-frequency Rayleigh waves in the cross-correlations over sedimentary basins. The particle motion provide a good test for distinguishing the fundamental mode from the higher mode, with the fundamental mode having retrograde motion and the higher mode having prograde motion in the 1-10 s period of interest. The basement depth controls the cut-off period, above which the higher mode is evanescent that coincides with a rapid increase

in the ellipticity or H/V ratio of the fundamental mode. The relative amplitude of the higher and fundamental mode in the cross-correlation is not only determined by the Green's function, but also the noise source distribution, especially in the partitioning between source force components.

In Part II, we used data from a dense box-like array that was deployed progressively in Southern Peru (PeruSE experiment) to image the crust and uppermost mantle structure of the subduction zone. Ambient-noise and earthquake Rayleigh waves are used to construct the V_{SV} model, and receiver functions are used to image the interfaces (e.g., oceanic and continental Moho, the mid-crust structures) with a focus on the flat subduction regime.

The over 4-km high topography of the Central Andes is supported by ~ 70 km thick crust. A mid-crust low-velocity zone is revealed, and is interpreted as partially molten rocks that are part of the Andean low-velocity zone. It is oblique to the present trench, and possibly indicates the location of the volcanic arcs formed during the steepening of the Oligocene flat slab beneath the Altiplano Plateau. The top of the Brazilian Shield is imaged as a thrust fault beneath the whole Eastern Cordillera. A velocity contrast from crust to uppermost mantle is imaged across the Cusco-Vilcanota Fault System, and is interpreted as the boundary between two lithospheric blocks.

In the flat subduction regime, the Nazca slab subducts to ~ 100 km depth and then remains flat for ~ 300 km distance before it resumes normal dipping subduction. The flat part of the slab closely follows the topography of the continental Moho above indicating a strong interplate suction force. The velocity of the upper mantle above the flat slab is comparatively high, indicating a dry and cold environment. The velocity turns to normal values before the slab steepens again, indicating possible resumption of dehydration and eclogitization.

In addition, we report on a strong scatterer of seismic energy in the 5-10 s period range located in the volcanic arc of Southern Peru. It produces strong precursor and coda waves relative to the interstation Rayleigh wave in the cross-correlations. We model the scatterer as a cylinder approximately 5 km in diameter with a shear wave

velocity 30% lower than the background velocity. It is likely to exist at the depth of 5-10 km, and is located at 71.6°W/16.1°S, which is near the inactive volcano Nevada Chachani and the active volcano El Misti which recently erupted in 1985.

Bibliography

- Aki, K. and Richards, P. G. (2002). *Quantitative seismology*, volume 1.
- Aster, R. C., Borchers, B., and Thurber, C. H. (2011). *Parameter estimation and inverse problems*. Academic Press.
- Barmin, M., Ritzwoller, M., and Levshin, A. (2001). A fast and reliable method for surface wave tomography. In *Monitoring the Comprehensive Nuclear-Test-Ban Treaty: Surface Waves*, pages 1351–1375. Springer.
- Bensen, G., Ritzwoller, M., Barmin, M., Levshin, A., Lin, F., Moschetti, M., Shapiro, N., and Yang, Y. (2007). Processing seismic ambient noise data to obtain reliable broad-band surface wave dispersion measurements. *Geophysical Journal International*, 169(3):1239–1260.
- Boaga, J., Cassiani, G., Strobbia, C. L., and Vignoli, G. (2013). Mode misidentification in Rayleigh waves: Ellipticity as a cause and a cure. *Geophysics*, 78(4):EN17–EN28.
- Brocher, T. M. (2005). Empirical relations between elastic wavespeeds and density in the Earth’s crust. *Bulletin of the Seismological Society of America*, 95(6):2081–2092.
- Crouch, J. K. and Suppe, J. (1993). Late Cenozoic tectonic evolution of the Los Angeles basin and inner California borderland: A model for core complex-like crustal extension. *Geological Society of America Bulletin*, 105(11):1415–1434.

- Denolle, M., Dunham, E., Prieto, G., and Beroza, G. (2013). Ground motion prediction of realistic earthquake sources using the ambient seismic field. *Journal of Geophysical Research: Solid Earth*, 118(5):2102–2118.
- Denolle, M., Dunham, E., Prieto, G., and Beroza, G. (2014). Strong ground motion prediction using virtual earthquakes. *Science*, 343(6169):399–403.
- Fäh, D., Kind, F., and Giardini, D. (2001). A theoretical investigation of average H/V ratios. *Geophysical Journal International*, 145(2):535–549.
- Fang, H., Yao, H., Zhang, H., Huang, Y.-C., and van der Hilst, R. D. (2015). Direct inversion of surface wave dispersion for three-dimensional shallow crustal structure based on ray tracing: methodology and application. *Geophysical Journal International*, 201(3):1251–1263.
- Field, E. and Jacob, K. (1993). The theoretical response of sedimentary layers to ambient seismic noise. *Geophysical research letters*, 20(24):2925–2928.
- Fuis, G., Ryberg, T., Godfrey, N., Okaya, D., and Murphy, J. (2001). Crustal structure and tectonics from the Los Angeles basin to the Mojave Desert, southern California. *Geology*, 29(1):15–18.
- Gutscher, M.-A. (2002). Andean subduction styles and their effect on thermal structure and interplate coupling. *Journal of South American Earth Sciences*, 15(1):3–10.
- Gutscher, M.-A., Spakman, W., Bijwaard, H., and Engdahl, E. R. (2000). Geodynamics of flat subduction: Seismicity and tomographic constraints from the Andean margin. *Tectonics*, 19(5):814–833.
- Haney, M. M. and Tsai, V. C. (2015). Nonperturbational surface-wave inversion: A Dix-type relation for surface waves. *Geophysics*, 80(6):EN167–EN177.
- Hauksson, E. (2000). Crustal structure and seismicity distribution adjacent to the

- Pacific and North America plate boundary in southern California. *Journal of Geophysical Research: Solid Earth (1978–2012)*, 105(B6):13875–13903.
- Hauksson, E. and Haase, J. S. (1997). Three-dimensional VP and VP/VS velocity models of the Los Angeles basin and central Transverse Ranges, California. *Journal of Geophysical Research: Solid Earth (1978–2012)*, 102(B3):5423–5453.
- Herrmann, R. and Ammon, C. (2002). Computer programs in seismology: Surface waves, receiver functions and crustal structure. *St. Louis University, St. Louis, MO*.
- Husson, L. and Sempere, T. (2003). Thickening the Altiplano crust by gravity-driven crustal channel flow. *Geophysical Research Letters*, 30(5).
- Ingersoll, R. V. and Rumelhart, P. E. (1999). Three-stage evolution of the Los Angeles basin, southern California. *Geology*, 27(7):593–596.
- Jennings, C. and Bryant, W. (2010). Fault Activity Map of California: California Geological Survey. *Geologic Data Map*, 6.
- Kohler, M., Magistrale, H., and Clayton, R. (2003). Mantle heterogeneities and the SCEC reference three-dimensional seismic velocity model version 3. *Bulletin of the Seismological Society of America*, 93(2):757–774.
- Kohler, M. D. and Davis, P. M. (1997). Crustal thickness variations in southern California from Los Angeles Region Seismic Experiment passive phase teleseismic travel times. *Bulletin of the Seismological Society of America*, 87(5):1330–1344.
- Komatitsch, D., Liu, Q., Tromp, J., Süß, P., Stidham, C., and Shaw, J. H. (2004). Simulations of ground motion in the Los Angeles basin based upon the spectral-element method. *Bulletin of the Seismological Society of America*, 94(1):187–206.
- Lamb, S., Hoke, L., Kennan, L., and Dewey, J. (1996). Cenozoic evolution of the Central Andes in Bolivia and northern Chile. *SPECIAL PUBLICATION-GEOLOGICAL SOCIETY OF LONDON*, 121:237–264.

- Lee, E.-J., Chen, P., Jordan, T. H., Maechling, P. B., Denolle, M. A., and Beroza, G. C. (2014). Full-3-D tomography for crustal structure in Southern California based on the scattering-integral and the adjoint-wavefield methods. *Journal of Geophysical Research: Solid Earth*, 119(8):6421–6451.
- Li, D., Helmberger, D., Clayton, R. W., and Sun, D. (2014). Global synthetic seismograms using a 2-D finite-difference method. *Geophysical Journal International*, 197(2):1166–1183.
- Ligorria, J. P. and Ammon, C. J. (1999). Iterative deconvolution and receiver-function estimation. *Bulletin of the seismological Society of America*, 89(5):1395–1400.
- Lin, F.-C., Li, D., Clayton, R. W., and Hollis, D. (2013). High-resolution 3D shallow crustal structure in Long Beach, California: Application of ambient noise tomography on a dense seismic array. *Geophysics*, 78(4):Q45–Q56.
- Lin, F.-C., Moschetti, M. P., and Ritzwoller, M. H. (2008). Surface wave tomography of the western United States from ambient seismic noise: Rayleigh and Love wave phase velocity maps. *Geophysical Journal International*, 173(1):281–298.
- Lin, F.-C., Tsai, V. C., and Schmandt, B. (2014). 3-D crustal structure of the western United States: application of Rayleigh-wave ellipticity extracted from noise cross-correlations. *Geophysical Journal International*, page ggu160.
- Luo, Y., Yang, Y., Xu, Y., Xu, H., Zhao, K., and Wang, K. (2015). On the limitations of interstation distances in ambient noise tomography. *Geophysical Journal International*, 201(2):652–661.
- Ma, Y., Clayton, R. W., Tsai, V. C., and Zhan, Z. (2013). Locating a scatterer in the active volcanic area of Southern Peru from ambient noise cross-correlation. *Geophysical Journal International*, 192(3):1332–1341.
- Magistrale, H., Day, S., Clayton, R. W., and Graves, R. (2000). The SCEC Southern California reference three-dimensional seismic velocity model version 2. *Bulletin of the Seismological Society of America*, 90(6B):S65–S76.

- Mamani, M., Wörner, G., and Sempere, T. (2010). Geochemical variations in igneous rocks of the Central Andean orocline (13 S to 18 S): tracing crustal thickening and magma generation through time and space. *Geological Society of America Bulletin*, 122(1-2):162–182.
- Manea, V. C., Pérez-Gussinyé, M., and Manea, M. (2012). Chilean flat slab subduction controlled by overriding plate thickness and trench rollback. *Geology*, 40(1):35–38.
- McCulloch, T. H. (1960). Gravity variations and the geology of the Los Angeles basin of California. *US Geol. Surv. Profess. Pap. 400-B*, pages 320–325.
- McKenzie, D. (1978). Some remarks on the development of sedimentary basins. *Earth and Planetary science letters*, 40(1):25–32.
- Nakamura, Y. (1989). A method for dynamic characteristics estimation of subsurface using microtremor on the ground surface. *Railway Technical Research Institute, Quarterly Reports*, 30(1).
- Nakata, N., Chang, J. P., Lawrence, J. F., and Boué, P. (2015). Body wave extraction and tomography at Long Beach, California, with ambient-noise interferometry. *Journal of Geophysical Research: Solid Earth*, 120(2):1159–1173.
- Nicholson, C., Sorlien, C. C., Atwater, T., Crowell, J. C., and Luyendyk, B. P. (1994). Microplate capture, rotation of the western Transverse Ranges, and initiation of the San Andreas transform as a low-angle fault system. *Geology*, 22(6):491–495.
- O’Driscoll, L. J., Richards, M. A., and Humphreys, E. D. (2012). Nazca–South America interactions and the late Eocene–late Oligocene flat-slab episode in the central Andes. *Tectonics*, 31(2).
- Olsen, K. (2000). Site amplification in the Los Angeles basin from three-dimensional modeling of ground motion. *Bulletin of the Seismological Society of America*, 90(6B):S77–S94.

- Oncken, O., Hindle, D., Kley, J., Elger, K., Victor, P., and Schemmann, K. (2006). Deformation of the central Andean upper plate system—Facts, fiction, and constraints for plateau models. In *The Andes*, pages 3–27. Springer.
- PeruSE (2013). Peru Subduction Experiment. Caltech. Dataset. doi:10.7909/C3H41PBZ.
- Phillips, K. and Clayton, R. W. (2014). Structure of the subduction transition region from seismic array data in southern Peru. *Geophysical Journal International*, 196(3):1889–1905.
- Phillips, K., Clayton, R. W., Davis, P., Tavera, H., Guy, R., Skinner, S., Stubailo, I., Audin, L., and Aguilar, V. (2012). Structure of the subduction system in southern Peru from seismic array data. *Journal of Geophysical Research: Solid Earth (1978–2012)*, 117(B11).
- Plesch, A., Tape, C., Graves, R., Small, P., Ely, G., and Shaw, J. (2011). Updates for the CVM-H including new representations of the offshore Santa Maria and San Bernardino basin and a new Moho surface. In *2011 Southern California Earthquake Center Annual Meeting, Proceedings and Abstracts*, volume 21, page 214.
- Ramos, V. A. and Folguera, A. (2009). Andean flat-slab subduction through time. *Geological Society, London, Special Publications*, 327(1):31–54.
- Rivet, D., Campillo, M., Sanchez-Sesma, F., Shapiro, N. M., and Singh, S. K. (2015). Identification of surface wave higher modes using a methodology based on seismic noise and coda waves. *Geophysical Journal International*, 203(2):856–868.
- Savage, M. K., Lin, F.-C., and Townend, J. (2013). Ambient noise cross-correlation observations of fundamental and higher-mode Rayleigh wave propagation governed by basement resonance. *Geophysical Research Letters*, 40(14):3556–3561.
- Sawyer, D. S., Hsui, A. T., and Toksöz, M. N. (1987). Extension, subsidence and thermal evolution of the Los Angeles Basin—a two-dimensional model. *Tectonophysics*, 133(1):15–32.

- Schilling, F. R., Trumbull, R. B., Brasse, H., Haberland, C., Asch, G., Bruhn, D., Mai, K., Haak, V., Giese, P., Muñoz, M., et al. (2006). Partial melting in the Central Andean crust: a review of geophysical, petrophysical, and petrologic evidence. In *The Andes*, pages 459–474. Springer.
- Shapiro, N. M., Campillo, M., Stehly, L., and Ritzwoller, M. H. (2005). High-resolution surface-wave tomography from ambient seismic noise. *Science*, 307(5715):1615–1618.
- Shaw, J. H., Plesch, A., Tape, C., Suess, M. P., Jordan, T. H., Ely, G., Hauksson, E., Tromp, J., Tanimoto, T., Graves, R., et al. (2015). Unified Structural Representation of the southern California crust and upper mantle. *Earth and Planetary Science Letters*, 415:1–15.
- Shirzad, T. and Shomali, Z. H. (2014). Shallow crustal radial anisotropy beneath the Tehran basin of Iran from seismic ambient noise tomography. *Physics of the Earth and Planetary Interiors*, 231:16–29.
- Skinner, S. M. and Clayton, R. W. (2013). The lack of correlation between flat slabs and bathymetric impactors in South America. *Earth and Planetary Science Letters*, 371:1–5.
- Süss, M. P. and Shaw, J. H. (2003). P wave seismic velocity structure derived from sonic logs and industry reflection data in the Los Angeles basin, California. *Journal of Geophysical Research: Solid Earth (1978–2012)*, 108(B3).
- Tanimoto, T. and Rivera, L. (2008). The ZH ratio method for long-period seismic data: sensitivity kernels and observational techniques. *Geophysical Journal International*, 172(1):187–198.
- Tape, C., Liu, Q., Maggi, A., and Tromp, J. (2009). Adjoint tomography of the southern California crust. *Science*, 325(5943):988–992.

- Turcotte, D. and McAdoo, D. (1979). Thermal subsidence and petroleum generation in the southwestern block of the Los Angeles Basin, California. *Journal of Geophysical Research: Solid Earth (1978–2012)*, 84(B7):3460–3464.
- Ward, K. M., Porter, R. C., Zandt, G., Beck, S. L., Wagner, L. S., Minaya, E., and Tavera, H. (2013). Ambient noise tomography across the Central Andes. *Geophysical Journal International*, page ggt166.
- Wright, T. L. (1991). Structural geology and tectonic evolution of the Los Angeles Basin, California. *Active Margin Basins*, 52:35–134.
- Yano, T., Tanimoto, T., and Rivera, L. (2009). The ZH ratio method for long-period seismic data: inversion for S-wave velocity structure. *Geophysical Journal International*, 179(1):413–424.
- Yao, H., van Der Hilst, R. D., and Maarten, V. (2006). Surface-wave array tomography in SE Tibet from ambient seismic noise and two-station analysis-I. Phase velocity maps. *Geophysical Journal International*, 166(2):732–744.
- Yerkes, R. F., McCulloh, T. H., Schoellhamer, J., and Vedder, J. G. (1965). Geology of the Los Angeles basin, California: an introduction. *US, Geol. Surv., Prof. Pap.:(United States)*, 420.
- Yuan, X., Sobolev, S., Kind, R., Oncken, O., Bock, G., Asch, G., Schurr, B., Graeber, F., Rudloff, A., Hanka, W., et al. (2000). Subduction and collision processes in the Central Andes constrained by converted seismic phases. *Nature*, 408(6815):958–961.
- Zhu, L. and Kanamori, H. (2000). Moho depth variation in southern California from teleseismic receiver functions. *Journal of Geophysical Research B*, 105(B2):2969–2980.
- Zhu, L. and Rivera, L. A. (2002). A note on the dynamic and static displacements from a point source in multilayered media. *Geophysical Journal International*, 148(3):619–627.